

Study of Electron Showers in a Prototype Hadron Calorimeter for a Future Linear Collider

von

Anna Rosmanitz¹

Masterarbeit in Physik
vorgelegt dem Fachbereich Physik, Mathematik und Informatik (FB 08)
der Johannes Gutenberg-Universität Mainz
am 24. November 2017

1. Gutachter: Prof. Dr. Lucia Masetti
2. Gutachter: Prof. Dr. Volker Büscher

¹arosmani@students.uni-mainz.de

Ich versichere, dass ich die Arbeit selbstständig verfasst und keine anderen als die angegebenen Quellen und Hilfsmittel benutzt sowie Zitate kenntlich gemacht habe.

Mainz, den 24.11.2017

Anna Rosmanitz
ETAP
Institut für Physik
Staudingerweg 7
Johannes Gutenberg-Universität D-55099 Mainz
arosmani@students.uni-mainz.de

Abstract

The CALICE collaboration is developing highly granular calorimeters for the ILC, a planned electron-positron linear collider. In this thesis, data taken at an electron test beam in July and August at DESY with energies of 1 to 5 GeV from an engineering prototype are analysed. In this test beam setup, power pulsing, for which the electronics are switched off except for when a particle bunch arrives to reduce energy consumption and heating, is used for the first time. The goal of the analysis is to examine if there are differences between data with and without power pulsing.

Contents

1	Introduction	1
2	Theoretical concepts	3
2.1	Standard model	3
2.1.1	Elementary particles	3
2.1.2	Fundamental forces	4
2.2	Interaction of particles with matter	5
2.2.1	Electromagnetic interaction	5
2.2.2	Hadronic interaction	8
2.2.3	Electromagnetic showers	10
2.2.4	Hadronic showers	11
2.3	Calorimetry	12
2.3.1	Energy resolution	13
2.3.2	Typical structures of multi-purpose detectors	14
2.4	Particle Flow Algorithm	15
3	ILC and ILD	17
3.1	ILC	17
3.2	ILD	18
3.3	SiD	20
4	CALICE AHCAL	22
4.1	HCAL Basic Unit	22
4.1.1	SPIROC2b ASIC	23
4.1.2	Scintillator tiles	24
4.1.3	Silicon photomultipliers	24
4.1.3.1	Properties	25
4.2	Test beam setup	27
4.2.1	Test beam facility	27
4.2.2	Detector setup	28
4.2.3	Data taking	29
5	Software	30
5.1	Gain calibration	30
5.2	MIP calibration	33
5.3	Reconstruction	34
5.4	Simulation	34
5.5	Temperature correction	35

6	Analysis of test beam data	36
6.1	Calibration of SiPM gain	36
6.2	Determination of MIP energy	42
6.2.1	TDC cut	42
6.2.2	MIP values	42
6.3	Temperature difference	44
6.4	Analysis of electron data	44
6.4.1	Beam profiles	44
6.4.2	Longitudinal shower profile	46
6.5	Detailed comparison of the data with and without power pulsing . . .	51
6.5.1	Linearity of energy measurement	57
7	Conclusion and Outlook	59
8	Appendix	64
8.1	Cellwise energy distribution	64
8.2	2D distributions for each layer	70
9	Acknowledgements	73

1 Introduction

Particle physics aims to examine the properties of the particles that build our world, of which the smallest known are called elementary particles, with the help of collider experiments. By producing collisions between particles like electrons and positrons and observing the decay products, the kinetic energy is transformed into mass allowing to produce and observe heavier, short lived particles.

Currently, the collider with the highest energies is the Large Hadron Collider (LHC), where protons with centre of mass energies of 13 TeV (since spring 2015) collide. Here, the Higgs particle was discovered in 2012 at energies of 8 TeV. Proton-proton-colliders are useful to discover new particles, but their resolution is worse than that of a comparable e^+e^- -collider.

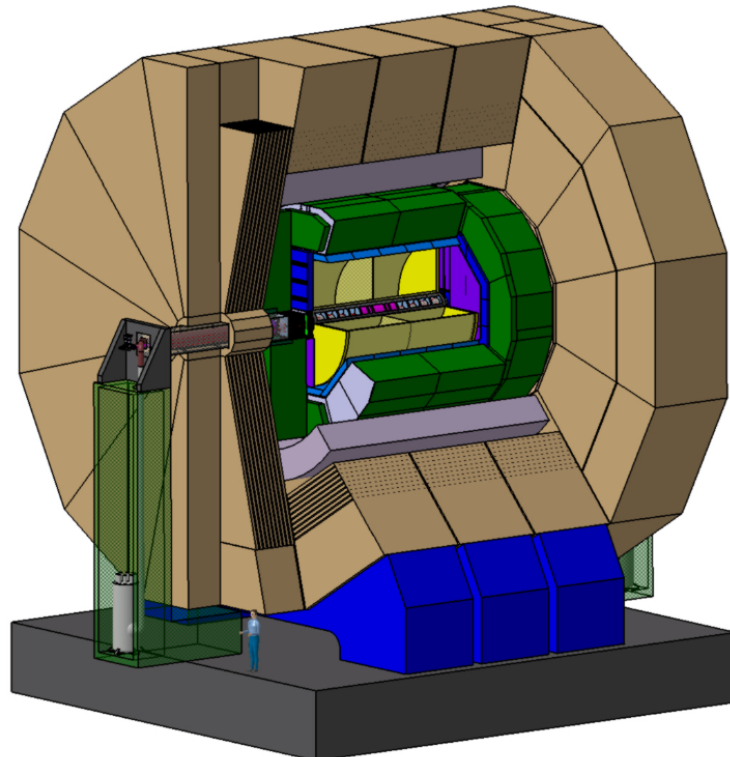


Figure 1.1: Concept for the ILC; [1]

1 Introduction

The International Linear Collider (ILC) is a proposal for a new linear collider to investigate the properties of the Higgs boson as well as the top quark and to search for new elementary particles. It will be an e^+e^- -collider running at energies of 500 GeV. The accelerator is linear in order to avoid energy loss by bremsstrahlung caused by the curvature of a ring accelerator, and thus allows reaching higher energies. [2]

To observe the collisions the International Linear Detector (ILD) and the Silicon Detector (SiD) are proposed. This thesis will concentrate on the ILC, whose concept is shown in figure 1.1. One of the goals is to achieve a hadronic jet resolution of $30\%/\sqrt{E[\text{GeV}]}$. Therefore, the requirement for the detectors is to have high precision measurements which are achieved by the use of Particle Flow Algorithms (PFA) that track the exact path of each particle. To be able to use those, the detector needs to have a high granularity. In addition, an angular coverage of nearly 100% is necessary. [1]

The CALICE (CALorimeter for LInear Collider Experiment) collaboration is developing different calorimeter concepts to be used for the ILD, which need to be able to operate in high magnetic fields. Currently, sampling calorimeters consisting of absorbing material made out of steel alternating with layers of sensitive material out of scintillator tiles read out by silicon photomultipliers are investigated on. [1] There have been several physics prototypes to identify the optimal configurations for those layers and other components. The final detector will have around 8 million channels. This large magnitude makes it important to build a technical prototype as well to test technical challenges like assembly, power supply, readout electronics and cooling systems.

This thesis analyses data from an engineering prototype which was tested in summer 2016 at DESY. In this test power pulsing was applied for the first time. Power pulsing means that the detector is alternately switched on and off in time with the particle bunches arriving from the accelerator. This helps to reduce energy consumption and heating which avoids cooling systems for the electronics.

This thesis will first explain the theoretical background and the components of the detector. Next, the setup for the test beam is explained. Then, the calibration for the silicon photomultipliers is done and finally, test beam data is analysed. Further, data with and without power pulsing is compared with simulations.

Standard Model of Elementary Particles

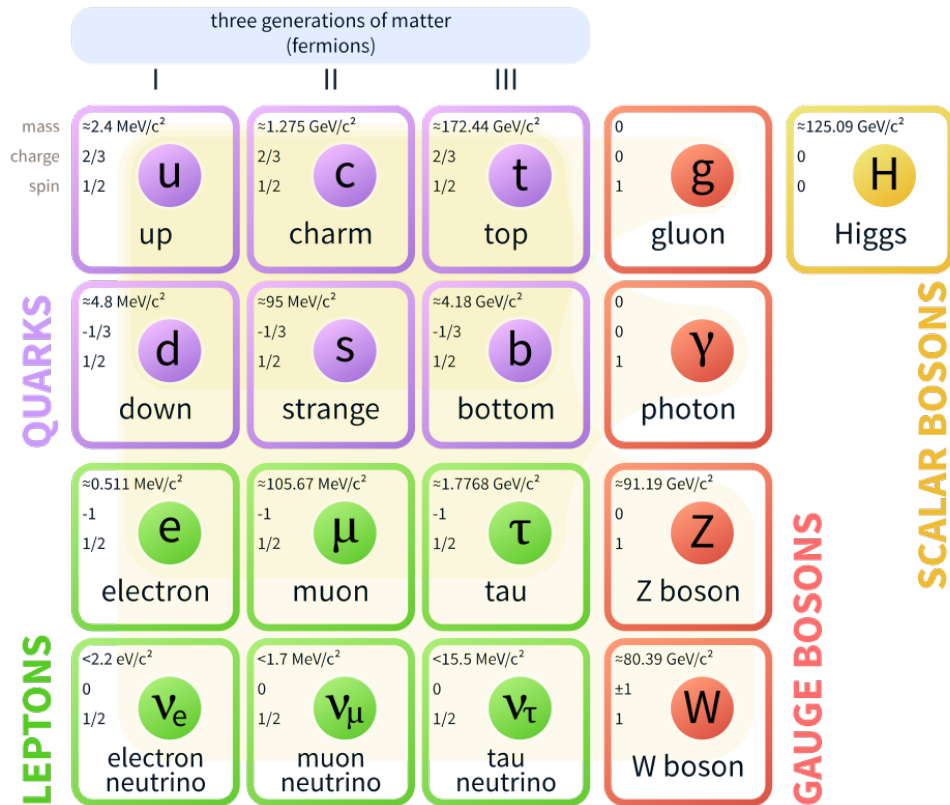


Figure 2.1: Standard model of particle physics [3]

2 Theoretical concepts

2.1 Standard model

2.1.1 Elementary particles

Elementary particles are the smallest known particles of which all other matter is built of. Currently, there are 25 known elementary particles as described in figure 2.1, but this number might change with future discoveries. In general, particles belong into two different groups: **fermions** have a half-integral spin and **bosons** have a whole-number

2 Theoretical concepts

spin [4]. Those 25 particles can be divided further in several sub-groups:

- **Quarks:** Quarks are fermions. They have a spin of $\frac{1}{2}$ and an electrical charge of $+\frac{2}{3}e$ for the up, charm, and top quark and $-\frac{1}{3}e$ for the down, strange, and bottom quark and a colour charge. There are three generations of quarks divided by weight. The lightest quarks are the up and the down quark, followed by the charm and strange and the heaviest quarks are the top and bottom quark. Quarks are effected by the weak, strong and electromagnetic forces. Particles, that consist of quarks are called hadrons. Each quark has an associated anti-quark which has the opposite charge. [5]
- **Leptons:** Like quarks, leptons have a spin of $\frac{1}{2}$ and thus are fermions. Each also has an anti-particle. There are three leptons with an electrical charge of $-1e$, those are the electron e , the muon μ and the tau τ , and three uncharged leptons, which are the electron-neutrino ν_e , the muon-neutrino ν_μ and the tau-neutrino ν_τ . The only stable leptons are the electron and its anti-particle, the positron. Like the quarks, the leptons can be divided by weight of the non-neutrino leptons into three generations where upon the neutrinos are nearly massless. From light to heavy, those are the electron and electron-neutrino, muon and muon-neutrino, and tau and tau-neutrino. [6]
- **Gauge Bosons:** The gauge bosons have a spin of 1. They are responsible for the transfer of the fundamental forces. The twelve known gauge bosons are: the photon γ , the Z^0 , the W^+ and W^- boson and eight gluons g with different colours. [6]
- **Higgs Boson:** The Higgs boson is an uncharged particle with spin 0. It is needed because the gauge invariance contains that the spin-1 gauge bosons have to be massless. But since the W^\pm and the Z^0 bosons are rather heavy, the scalar Higgs field is introduced to overcome the problem with gauge invariance. When interacting with this Higgs field, the elementary particles gain their mass, whereat the interaction with gauge bosons remains gauge invariant. In contrast to other fields like the electromagnetic field, the vacuum state η_0 , which contains no particles, has a nonzero value, that value is not invariant under gauge transformation. Like that, the whole theory is not gauge invariant and thus, the gauge bosons are allowed to have a mass. The Higgs boson results from the elementary excitation of the Higgs field. [6] The Higgs boson was first measured in 2012 at CERN. Its manners of coupling to other particles will hopefully be determined in the next years. [7]

2.1.2 Fundamental forces

- **Strong Force:** The strong force is responsible for the binding between quarks with the help of gluons, and as well between protons and neutrons in a very

2 Theoretical concepts

short range ($\sim 10^{-15}\text{m}$). Thus, it provides the stability of hadrons and also atomic nuclei. The gluons can transmit three different colour charges between the quarks which results in eight different gluons, one for each colour-anti-colour combination. In the end, the hadron itself is of colourless. Because of this, hadrons must consist of two (quark plus anti-quark) or three (three quarks or three anti-quarks) quarks. When trying to separate two quarks the gluons would act like a spring. Therefore, the further they are separated the more force has to be applied. When the braking point is reached, which means enough energy was put into the bond, a new quark- anti-quark-pair is created. This behaviour is called confinement. [8]

- **Electromagnetic Force:** The electromagnetic force is mediated by photons. It is responsible for most of the daily observed phenomena like electricity, light, magnetism and chemical reactions. Its range of influence is theoretically limitless but since it affects electrical charges, it can be shielded with a source of the opposite charge. The electromagnetic force is much stronger than the gravitation or the weak force but still weaker than the strong force. [9]
- **Weak Force:** The force carriers of the weak force are the W^\pm and the Z^0 bosons. It is very shortly ranged ($\sim 10^{-18}\text{m}$) and has a much lower energy than the electromagnetic and the strong force. It affects leptons as well as quarks and can convert one kind of particle into another one (but not leptons into quarks or vice versa). With this property, it is responsible for the radioactive beta decay. [6]
- **Gravitation:** The gravitational force causes attraction between mass-carrying particles. In contrast to electrical or magnetical forces it cannot be shielded and its influence is limitless, even though the strength is reduced with increasing distance. A suspected mediator is the graviton but it was not observed yet. On a sub-atomical scale, gravitation is much smaller than the other forces and thus its influence can be neglected. [9]

2.2 Interaction of particles with matter

When particles cross matter, they interact and loose part of their energy. There are different types of interaction. In this thesis, only hadrons, electrons and muons are covered. For those, it is useful to divide the interactions in hadronic and electromagnetic interactions. If the energy of the interacting particle is high enough multiple interactions can take place and an electromagnetic respectively hadronic particle shower is generated. The working principles of both types of interactions are discussed below.

2.2.1 Electromagnetic interaction

Electromagnetic interactions are initiated by electrons and photons, these processes are well described by the quantum electro dynamics. Their different possibilities of

2 Theoretical concepts

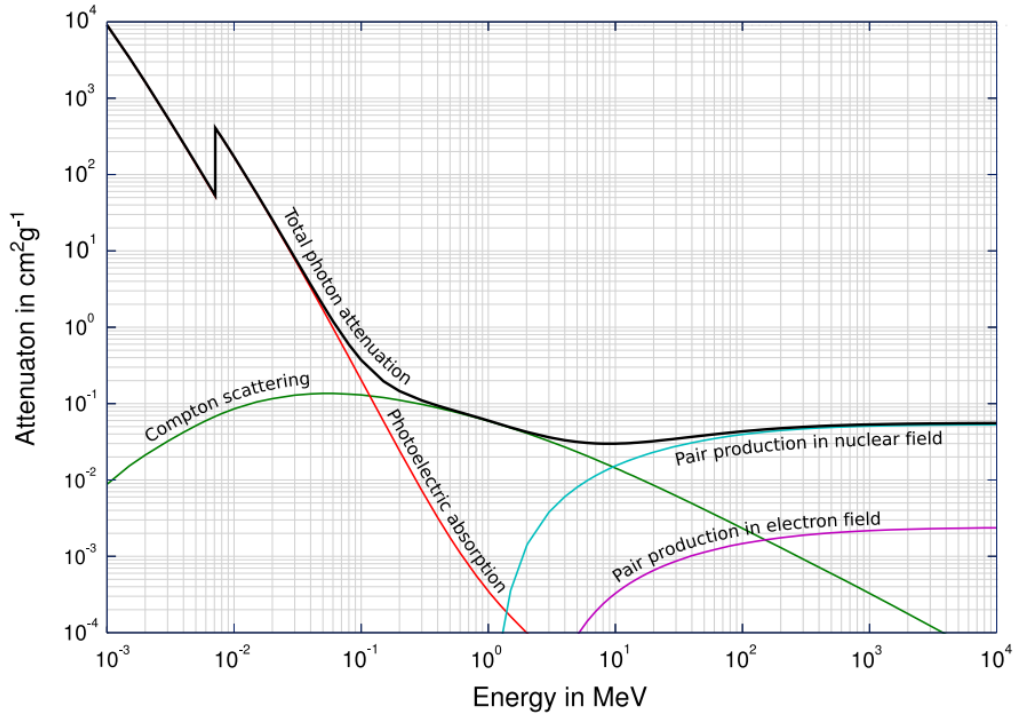


Figure 2.2: Interaction of photons with matter at different energies [10]

interacting at different energies are depicted in figure 2.2.

Photons can interact through:

- **Compton Scattering:** At low energies in the keV region, the Compton Effect is dominant. Here, a photon scatters on an other particle, usually on an electron in the atomic shell, whereby the wavelength of the photon is augmented. When scattering on an electron, the electron is removed from its shell and the atom is ionized. [11]
- **Photoelectric Absorption:** Also at low energies up to the MeV region the photoelectric absorption (also called photoelectric effect) takes place. Photons can knock electrons out of a material if their energy is high enough to make the absorbing electron overcome the electronic binding energy. [11]
- **Pair Production:** At high energies starting at the MeV region, pair production becomes dominant and the photon creates an electron-positron-pair when interacting with an atomic nucleus. On interaction with an electron in the atomic shell, this electron can be emitted. This is called triplet building because two electrons and a positron are created. [11]

Possible interactions for electrons are (see fig. 2.3):

2 Theoretical concepts

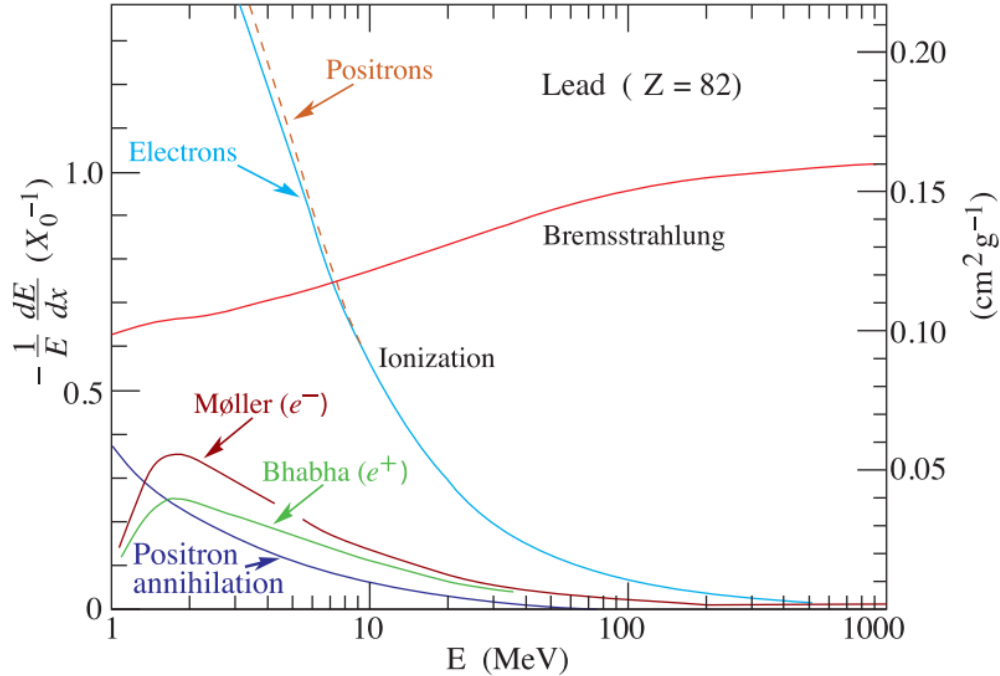


Figure 2.3: Interaction of electrons with matter at different energies [12]

- **Ionization:** When colliding with atoms, electrons can knock out one or several other electrons, which leaves the atom ionized. This process is dominant for energies below ~ 10 MeV. [6]
- **Bremsstrahlung:** When charged particles are decelerated they are emitting electromagnetic radiation, called bremsstrahlung, which has a continuous spectrum. Electrons are usually decelerated or deflected at an atomic nucleus. This process occurs mainly at energies above ~ 10 MeV. [11]
- **Cherenkov Radiation:** Cherenkov radiation is visible as a blue light that is created by fast electrons and other charged particles and can be observed in e.g. spent fuel pools of nuclear power plants. It arises when charged particles travel through matter with a higher velocity than the phase velocity of electromagnetic waves in this medium. [11]
- **Møller Scattering:** Møller scattering describes the process of electron-electron scattering. Two electrons interact with each other through a photon and consequently are deflected. [13]
- **Bhabha Scattering:** Similar to Møller scattering in Bhabha scattering an electron and a positron scatter on each other while exchanging a photon. [13]

2 Theoretical concepts

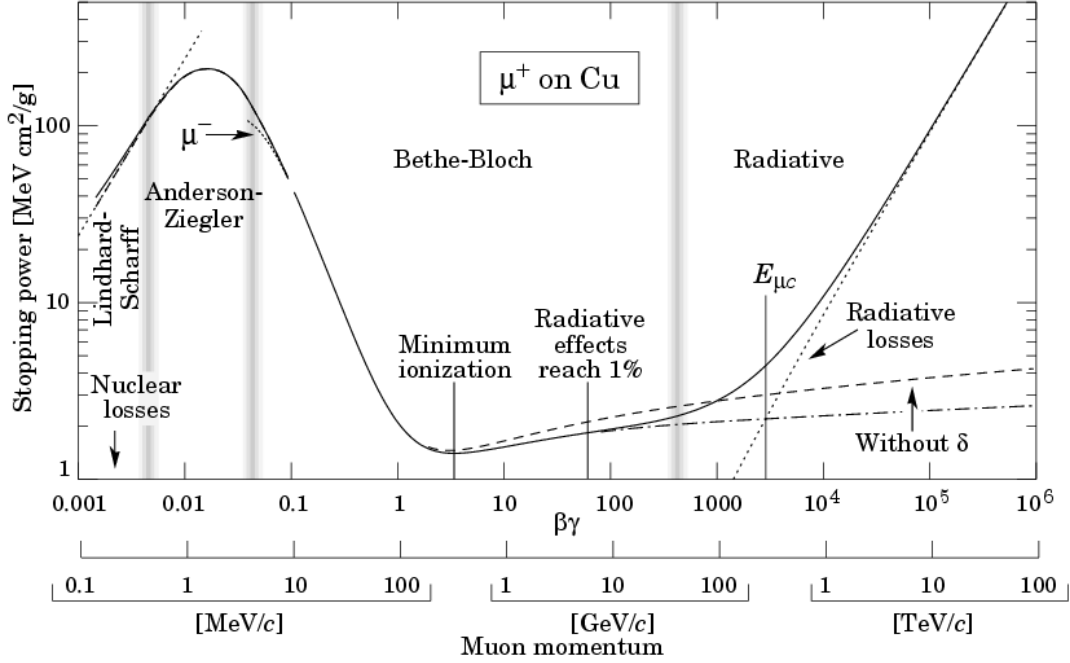


Figure 2.4: The Bethe-Bloch formula describes the mean energy loss of charged hadronic particles when crossing matter. Even though the picture shows the formula for muons, it is also valid for hadrons, because the x axis shows the momentum and can be calculated for other particles and their momentum. [14]

- **Positron Annihilation:** In positron annihilation (also called electron-positron annihilation) an electron and positron collide with each other. At low energies this will create two photons, at high energies also other particles (e.g. B mesons or W^\pm and Z^0 bosons) can be created. [13]

Since Møller and Bhabha scattering and positron annihilation only take place at low energies, they can be neglected in this thesis.

2.2.2 Hadronic interaction

Charged hadrons lose their energy mostly through strong interactions, but also by several other mechanisms:

- **Inelastic collisions with atomic electrons:** The penetrating particle collides with orbital electrons and excites or ionizes the atom. It experiences an average energy loss that can be described by the Bethe-Bloch formula (see fig. 2.4):

$$-\frac{dE}{dx} = \frac{4\pi n z^2}{m_e c^2 \beta^2} \cdot \left(\frac{e^2}{4\pi\epsilon_0}\right)^2 \cdot \left[\ln\left(\frac{2m_e c^2 \beta^2}{I(1-\beta^2)}\right) - \beta^2 \right] \quad (2.1)$$

2 Theoretical concepts

with:

$$\beta = \frac{v}{c}$$

v = Velocity of the particle

c = Speed of light

E = Energy of the particle

x = Travelling distance

z = Charge number

ϵ_0 = Vacuum permittivity

e = Elementary charge

n = Electron density

m_e = Mass of electron

I = Mean excitation potential [15]

The formula is valid for fast, charged and heavy particles.

- **Elastic Scattering with Nuclei:** Elastic scattering can excite the atom or knock out nuclear components which creates particles in the MeV range. [11]
- **Inelastic Nuclear Reactions:** Inelastic scattering leads to the production of further secondary hadrons with a similar energy to the incoming hadron. This process is also called spallation. [16]
- **Bremsstrahlung and Cherenkov Radiation:** Bremsstrahlung and Cherenkov radiation affect all kinds of charged particles. Their working principles are explained above. [11]

The Bethe-Bloch formula falls down to a minimum for $\beta\gamma$ in the range of 3 and 4. Particles in this region are called minimum ionising particles (MIP). [6] This region is almost the same for particles of the same charge. The energy loss of muons with a momentum in the GeV/c region is comparable to MIPs. [11]

An important note is, that the Bethe-Bloch formula only gives the mean energy loss. Thus, two particles do not necessarily need to have the same energy after travelling the same distance since interactions with the material are statistical processes. In the case of sufficiently large material, the energy of crossing particles follows a Gaussian distribution. The number of collisions is quite large and the central limit theorem, which states that every distribution converges to a Gaussian distribution with a high number of repetition, can be applied. In thin material, however, the central limit theorem cannot be applied and another distribution arises. Here, rare effects have a bigger impact, which adds a tail to the distribution. This type of energy loss was described by Landau, hence the distribution is called Landau distribution. Its maximum is called the Most Probable Value (MPV). [17]

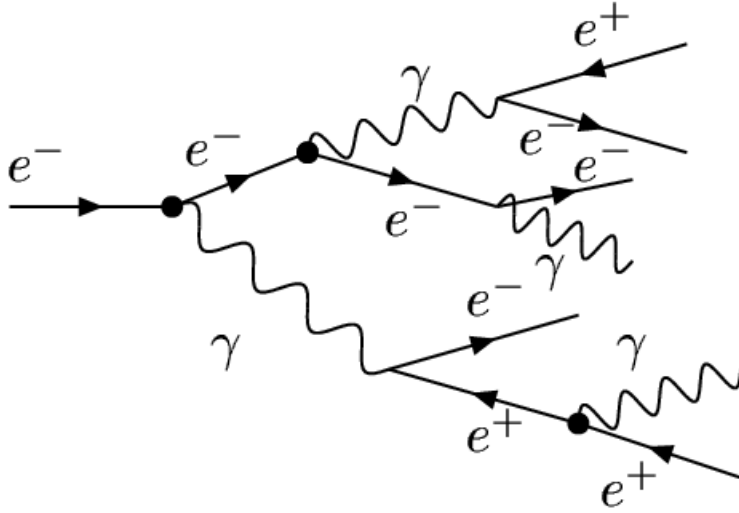


Figure 2.5: Electromagnetic shower development: High energy electrons produce photons by bremsstrahlung, which then creates more positrons and electrons by pair production until the energy of the particles gets too low and the shower dies out [18]

2.2.3 Electromagnetic showers

The energy where the influence of bremsstrahlung and ionization is the same is called critical energy. An electron with an energy higher than the critical energy will create photons through bremsstrahlung and lose energy because of this. Those photons can then create further electron-positron pairs. This generates an electromagnetic cascade, that will start to spread through the material until the energy of the electrons falls below the critical energy. Then, ionization prevails, no more photons are created and the shower dies out. The number of created particles increases logarithmically with the energy of the primary particle. An example for an electromagnetic shower is given in the left part of figure 2.5.

The longitudinal and lateral spread of electromagnetic showers depend on the material of the calorimeter and can be characterized by the radiation length X_0 and the Molière radius R_M . The radiation length is the mean free distance that an electron travels before it loses $\frac{1}{e}$ of its energy through bremsstrahlung as well as $\frac{7}{9}$ of the path of an high energy photon before pair production occurs. The radiation length for materials with the atomical number $Z > 2$ and the mass number A is given as:

$$X_0 \approx \frac{716.4 \cdot A}{Z(Z+1) \cdot \ln\left(\frac{287}{\sqrt{Z}}\right)} \left[\frac{\text{g}}{\text{cm}^2} \right] \quad (2.2)$$

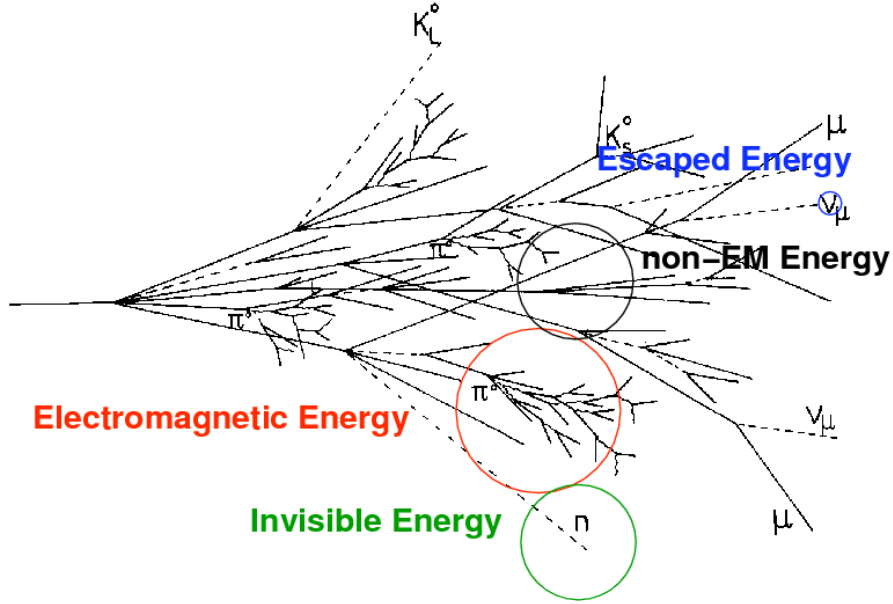


Figure 2.6: Hadronic shower development: Hadrons interact in more ways and create many different particles; the main interaction is inelastic hadronic interaction, that creates more hadrons. There are also electromagnetic sub-showers. Part of the energy, called invisible energy, is absorbed in binding energy and recoil and cannot be detected; particles spilling out of the detector before their energy can be measured carry the escaping energy [19]

The Molière radius describes the transversal spread of a shower. It corresponds to the radius of a cylinder around the shower centre in direction of the shower that contains 90% of the deposited energy. The Molière radius is important for calorimetry because a smaller radius corresponds with a better resolution and thus a better separation of showers from different particles. The Molière radius can be calculated with:

$$R_M = 0.0265 X_0 \cdot (Z + 1.2) \left[\frac{\text{g}}{\text{cm}^2} \right] \quad (2.3)$$

The Molière radius and the radiation length are important parameters to estimate the size of a planned calorimeter when the expected energy of the particles and the chosen material are already known. [16]

2.2.4 Hadronic showers

Similar to the electromagnetic showers, hadronic showers create more and more different particles until the energy of the single particles gets too low and the shower

2 Theoretical concepts

starts to die off. Compared to electromagnetic showers, many more processes occur in hadronic showers and thus, it is more complicated to describe them. An example for a hadronic shower is depicted on the right in figure 2.6. Hadronic showers have an electromagnetic component from decaying pions π^0 that propagates as described above. Additionally, they have the non-electromagnetic (respectively hadronic) component. In this shower part, inelastic hadronic interaction is dominant which is more unlikely than electromagnetic interactions, thus the hadronic shower is longer and has a wider lateral spread. In a detector, the energy of hadronic interactions cannot be detected completely because it will partly be absorbed by the binding energy or the recoil of the atoms upon impact. Therefore, the undetectable part is called invisible energy and makes up to 20% of the total energy. Also, if the dimensions of the detector are too small or if neutrinos are produced by the decay of short-lived hadrons in the shower, a part of the energy can escape the detector without being measured. This energy is called escaped energy. [17]

Depending on the material of the absorber the shower shape changes. This can be characterised with the nuclear interaction length λ_1 , that describes the mean free path before an inelastic interaction [17]:

$$\lambda_1 = \frac{A}{N_A \cdot \rho \cdot \sigma_{inel}(A)} \approx 35 \frac{A^{\frac{1}{3}}}{\rho} \text{ [cm]} \quad (2.4)$$

with:

A = Atomic mass number

N_A = Avogadro number

ρ = Density of the material

$\sigma_{inel}(A)$ = Inelastic cross section

In denser material, the probability for an interaction increases, thus λ_1 gets smaller and the shower depth shorter. Similar to the radiation length and the Molière radius for electromagnetic interactions, λ_1 can be used to plan the size of hadronic calorimeters. In comparison to electromagnetic showers, hadronic showers have a larger particle variety with different hadrons, muons, neutrinos, as well as photons, electrons, and photons from electronic sub-showers, while having a smaller density and a larger distribution. In an ordinary shower the energy loss from hadrons consist of 40 to 60% ionization, 10 to 15% creation of neutrons, 3% photons, and 30 to 45% from nuclear decay (ignoring neutral pions and mesons). [20]

To detect neutral particles, they have to undergo a reaction that sets off a charged particle that will then react as described above.

2.3 Calorimetry

In the previous section, the interaction of particles with matter was described. This section explains how these interactions can be measured.

2 Theoretical concepts

Calorimeters are a set-up to measure the energy of a particle. Calorimetry, in contrast to tracking, is destructive, that means particles are absorbed inside of the calorimeter and cannot be used afterwards. The energy can be deposited in many different ways, e.g. heat, ionization, or radiation. Part of these mechanisms are already explained above. Calorimeters can be divided in two groups: **Homogeneous** and **sampling calorimeters**.

In homogeneous calorimeters, the same material is used for the detector and the absorber. This can be material that scintillates, sends out Cherenkov light or is ionized. This detector type is only used for electromagnetic calorimeters. The advantage is that homogeneous calorimeters achieve the best energy resolution. On the other hand, they are quite expensive and give no longitudinal shower information.

The solution to this problem is to alternate layers made out of a dense and relatively cheap material e.g. lead, uranium, or iron, called absorber layers, and layers made out of active material (called active layers) like plastic scintillators, gas or silicon detectors, or noble liquid ionization chambers. This type of calorimeter is called sampling calorimeter. For those, the materials can be chosen more freely and adjusted to the purpose of the detector, the material is cheap, and by choosing a dense material the calorimeter can be built very compact. Furthermore, the longitudinal resolution is higher than for homogeneous calorimeters and a lateral separation can be build more easily. On the other hand, due to the sampling, not all of the energy is deposited in the detector layers, where it could be measured. Thus, the energy resolution of sampling calorimeters is worse.

The working principle for measuring electromagnetic and hadronic showers with a sampling calorimeter is basically the same, but since the nuclear interaction length is longer than the radiation length, the calorimeter for a hadronic shower needs to be longer or made out of a denser material to contain the same fraction of an electromagnetic shower. [16]

2.3.1 Energy resolution

The relative energy resolution σ_E/E of a calorimeter depends of three different terms. It can be written as:

$$\frac{\sigma_E}{E} = \frac{a}{\sqrt{E}} \oplus \frac{b}{E} \oplus c = \sqrt{\left(\frac{a}{\sqrt{E}}\right)^2 + \left(\frac{b}{E}\right)^2 + c^2} \quad (2.5)$$

Firstly, there is the sampling term a . It results from intrinsic statistical fluctuations since each shower develops differently (e.g. different sized electromagnetic showers in the hadronic showers) and sampling fluctuations originating from the loss of information in the absorber layers of a sampling calorimeter. When extrapolating the energy, fluctuations lead to imprecisions in the calculated total energy. The sampling term follows a Poisson distribution, scales with $\frac{1}{\sqrt{E}}$ and can be described with the term $\frac{a}{\sqrt{E}}$. Next, there is a noise term b that takes into account the electronics noise and background fluctuations. The noise level does not change with the particle energy,

2 Theoretical concepts

hence, its influence diminishes with increasing energies with $\frac{1}{E}$. Lastly, the constant term c that describes inaccurateness from calibrations, inhomogeneities in the sensitive areas, and leakage effects. The noise term limits the resolution at low energies, at high energies the constant term becomes the bigger influence. [16]

2.3.2 Typical structures of multi-purpose detectors

Different particles have varying kinds of interaction with material (as described in section 2.2). To be able to identify the particles, the detector needs to consist of different layers where the particles leave different signals. Figure 2.7 describes which particle leaves what kind of signal in the detector parts. The innermost part usually is the tracking chamber that measures the momentum of charged particles by bending their trajectory with a magnetic field. Only charged particles are able to ionize the gas in the tracking chamber and thus leave a track. After that, there is the Electromagnetic CALorimeter (ECAL) where electrons and photons produce showers, followed by the Hadron CALorimeter (HCAL) where the hadronic particles produce showers. Last, there is a muon chamber, where passing muons are detected. In the most optimal case, each particle can be identified and its path and energy can be measured. Additionally, to further improve the jet energy resolution, computer algorithms called Particle Flow Algorithms (PFA) can be used. [17] They are described in chapter 2.4.

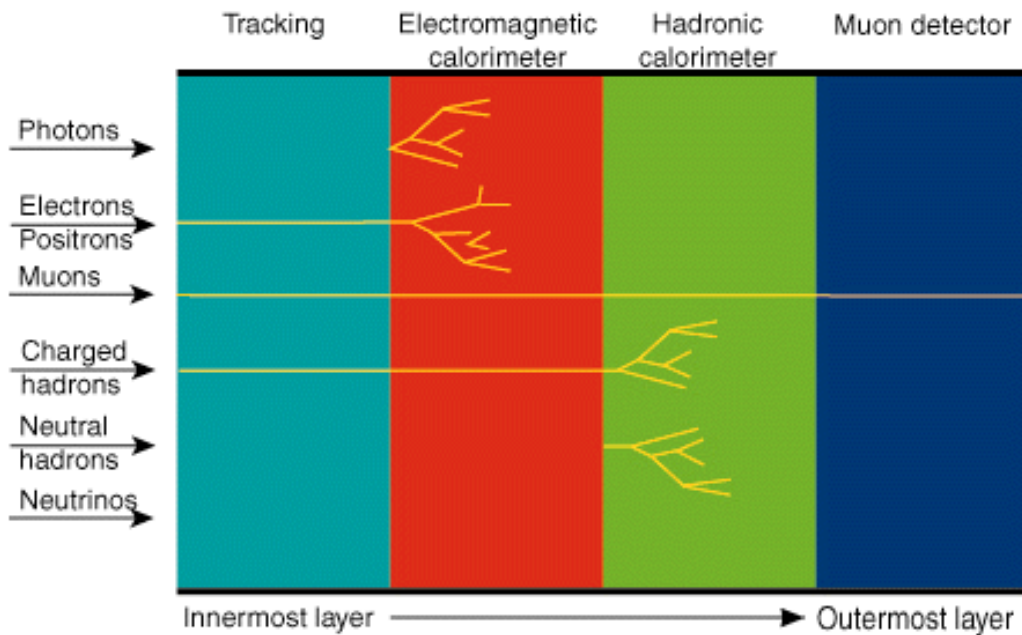


Figure 2.7: Schematic working principle of detectors [21]

2 Theoretical concepts

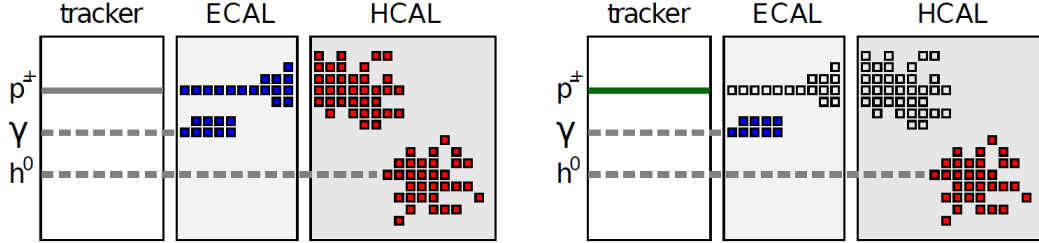


Figure 2.8: Left: Classical calorimetry: The energy deposition is used to measure the particle energy; Right: PFA measure charged particles with the curved path in the tracker and can assign hits in the calorimeter to certain particles [22]

2.4 Particle Flow Algorithm

The goal of a high hadronic jet resolution of the detector of $\sigma_E/E = 0.3/\sqrt{E[\text{GeV}]}$ requires algorithms that can differentiate between particle types and, to be able to use them, a highly granular detector. Those algorithms are called Particle Flow Algorithms (PFA). As described above, different particle types interact in separate detector layers. Charged particles are forced onto a curved trajectory by the magnetic field of the tracking chamber. From the curvature, the momentum of the particle can be calculated. With an assumption about the particle type (and thus its mass) the energy can be determined with a usually higher precision than from the calorimetric system. The exception are high momentum tracks where the momentum resolution lessens. Neutral particles are not detected by the tracking system and are only visible if they produce a particle shower. Thus, they have to be measured with the calorimetric system. The energy of the charged particles can also be measured with the calorimetric system which allows to make two measurements and thereby increases the resolution. In classical calorimetry, hadrons are measured with the energy they deposit in the different parts of the detector (as shown on the left of figure 2.8), for electrons and muons tracking is used. PFA allows the measurement of the energy of a single hadron by assigning the hits of the produced particles to the track of the initial particle (as shown on the right of figure 2.8) and by using the most precise particle for each created particle.

The resolution of the PFA is restricted if clusters overlap and cannot be separated. This problem is worse if charged and uncharged particle clusters are close, since the neutral particle cannot be detected in the tracker. In this case, the PFA might assign hits to the wrong particle. An example for this is given in figure 2.9. It shows the trajectories and overlapping clusters of a charged (blue) and an uncharged (red) particle. On the left, the clusters are shown with the correct assignment of hits. In the middle, too many hits are assigned to the charged particle and on the right, too many hits are assigned to the neutral particle. This is only an example, there a many

2 Theoretical concepts

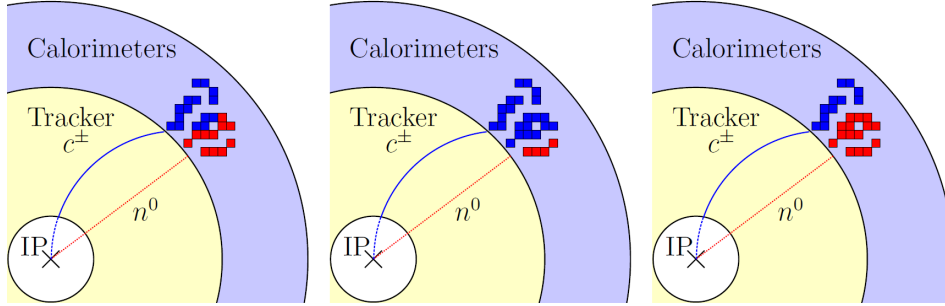


Figure 2.9: Overlapping clusters from charged (blue) and uncharged (red) particles can cause Particle Flow confusion; Left: Real cluster distribution; Middle: Too much energy contribution from cluster from charged particle; Right: Too much energy contribution from cluster from neutral particle [24]

more possibilities for confusions, e.g. if also muons are involved.

To reduce some of the confusion, reclustering with the expected energy derived from the tracking can be performed, but mainly the confusions can be reduced by using calorimeters with a high granularity. [23]

3 ILC and ILD

3.1 ILC

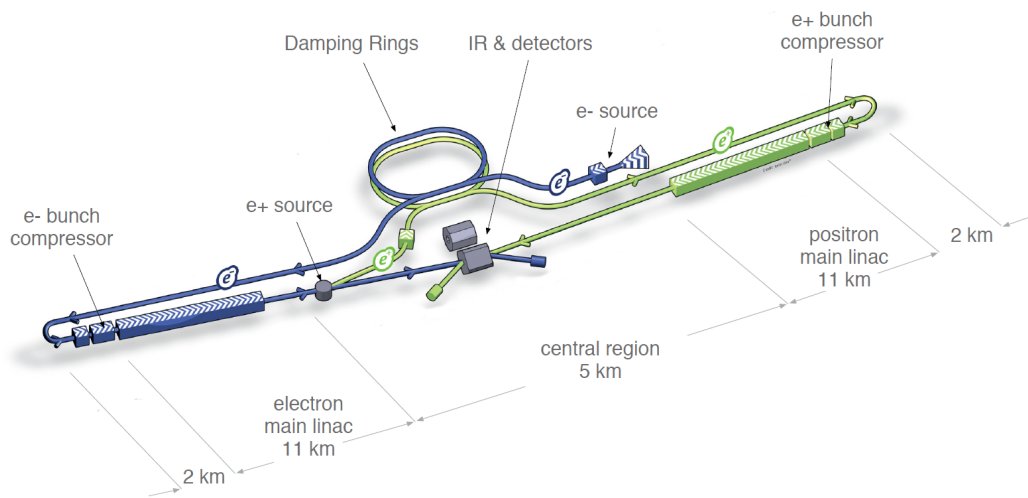


Figure 3.1: Concept for the ILC: Electrons and positrons are accelerated by different pre-accelerators until they reach the final linear accelerators. There, they are brought to their final energy of 250 GeV and collide with each other. [25]

As mentioned before, the ILC (International Linear Collider) is proposed to examine the Higgs boson, the top quark and to help with the search for new particles. The ILC will induce collisions of electrons and positrons at energies of 250 to 500 GeV with the option for an upgrade to 1 TeV. This would be much higher than the current highest collision energy of 209 GeV at the Large Electron-Positron collider (LEP). [25]

The electrons for the ILC are produced by pointing 2 ns laser pulses on a GaAs semiconductor cathode. The produced electrons are focused and accelerated to 5 GeV by a 370 m long linear accelerator system. The positrons are created by the 250 GeV electron beam in the main LINear ACcelerator (LINAC). The electrons cross an undulator where they emit gamma radiation. The radiation is directed on a thin titanium-alloy target where it produces an electron and positron shower. The positrons are collected and, like the 5 GeV electrons, injected into a damping ring where they emit synchrotron radiation through a process called radiation damping.

3 ILC and ILD

The same effect also is used in the undulator for the creation of the positrons. [26] Since electrons with a higher energy will lose more energy and electrons on different circuits are affected differently, the radiation damping is reducing synchrotron and betatron oscillations in the energy and the transversal direction. [27] In the ILC, there will be two damping rings, one for electrons and one for positrons.

After damping, the beams are travelling 15 km in opposite directions. They are accelerated to 15 GeV and the bunches are compressed from 6 mm to 0.3 mm on the way. This is accomplished by a LINAC system together with magnetic system of dipoles and quadrupoles. At the end, the beams are turned in by 180° via an arch and then sent in the main LINAC towards the collision point. There, the particles are accelerated up to 250 GeV (with a possible upgrade to 500 GeV). To reach energies of this dimension the LINAC is 11 km long and consists of superconducting microwave cavities with very high precision and is running at a temperature of -271°C . Afterwards, the electron beam is hitting the titanium-alloy target to produce the positrons and then travels towards the positron beam. As last step before collision both beams are heading through the final focus. The last two kilometres of the beam lines are equipped with a system of magnets instead of accelerating cavities. They function like a lens and focus the beams to a diameter of a few nanometres. The beams need to be monitored and controlled very precisely since small fluctuations could lead to the beams missing each other.

Finally, the beams collide with each other. In the best case, there could be up to 7000 mostly elastic interactions per second. The colliding electrons and positrons create particle showers that are measured in two detectors. The detectors are installed on a push-pull system and will be operated in turns. [26] The detectors are called International Linear Detector (ILD) (see section 3.2) and Silicon Detector (SiD) (see section 3.3). The idea behind building two detectors is, that they complement one another. Additionally, this allows to be able to cross-check results and reduce the impact of mishaps.

3.2 ILD

The design of the ILD contains the components described in section 2.3.2. It is depicted in figure 3.2 that shows one quarter of the ILD. It will have a total size of over 15×13 m and the inner parts of the detector will be inside a 3.5 T magnetic field. The interaction point lies in the center of the detector. In front of the tracking chamber, the ILD will have a pixel VerTeX detector (VTX) made of five layers that detects the position of the primary interaction and of the secondary decays. The tracking system consists of a combination of silicon trackers with a large-volume Time Projection Chamber (TPC). The silicon trackers are located between the VTX and TPC, and the TPC and ECAL. Additionally, they are installed in the forward region to track particles at low angles as well. They consist of several strip and pixel detectors. The TPC is responsible for the 3-dimensional point resolution, with up to 224 points

3 ILC and ILD

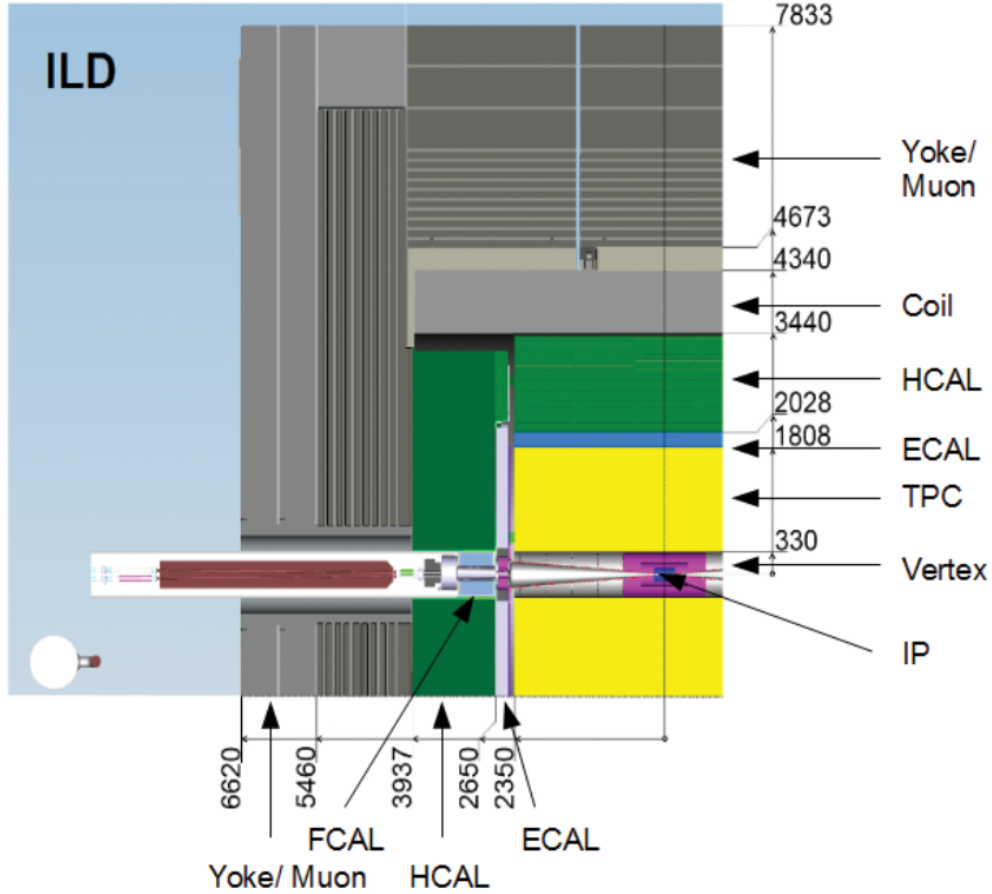


Figure 3.2: Schematic illustration of the ILD. Around the interaction point (IP) the different components of the ILD are built. First the tracking systems (Vertex detector and TPC), then the electromagnetic and the hadronic calorimeters, followed by the coil that produces a magnetic field inside the detector and finally the yoke that is also used as muon detector. [28]

per track, and can be used for the dE/dx -based particle identification.

Behind those trackers, the calorimeters are placed. First, there is an ECAL, as barrel form and as end-cap system. It is planned to have 30 layers with highly granular cells, separated by tungsten absorbers. The ECAL is followed by the Analogue HCAL (AHCAL), which will have a small transverse cell size, up to 48 layers and steel as absorbers. The AHCAL is made of two half barrels and also two endcaps. Each half barrel is divided in 16 sectors each containing 48 layers, as shown in figure 3.3. Each layer is built out of three slabs of five to six HCAL Uase units (HBU) each. [29]

To also measure the very forward angles radiation hard detectors are developed to increase the coverage to nearly 4π , measure the luminosity, and check the beam quality.

3 ILC and ILD

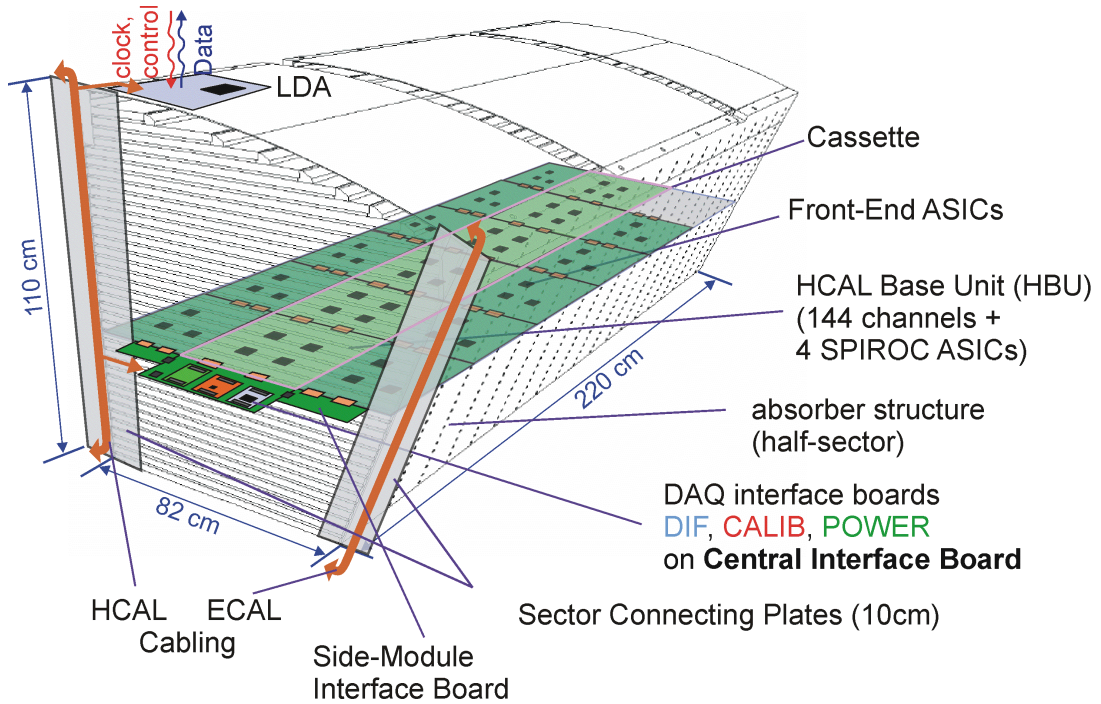


Figure 3.3: Scheme of a single AHCAL section with a layer and electronic components [28]

The whole setup is surrounded by a large superconducting coil that creates a 3.5 T magnetic field. Its iron yoke will be equipped with either scintillator strips or resistive plate chambers so that it can also be operated as muon filter, muon detector, and tail-catcher calorimeter.

For the ILD, power pulsing is used to minimize the energy usage and avoid heating, and hence the use of a cooling system. The front-end electronics are switched off while there are no particle collisions. On account of this, all parts of the detector need to be optimised to support power pulsing. [28]

3.3 SiD

The AHCAL was originally developed for the ILD but is now considered an option for the SiD hadron calorimeter.

The SiD incorporates a silicon pixel vertex detector, silicon trackers, silicon-tungsten ECAL, and a highly segmented HCAL, that offers the possibility to use of particle flow algorithms, inside of a high field solenoid, an iron flux return, and a muon identification system. Silicon is chosen to make the detector more robust to beam background, and to ensure a high resolution of the momenta of charged particles. The structure of the SiD is shown on the right of picture 3.4. The SiD has a approximate size of 12 x 12

3 ILC and ILD



Figure 3.4: Schematic illustration of the SiD. The most inner part is the tracking system made out of a vertex detector, followed by the ECAL and then the HCAL. Those parts are enclosed by a magnetic solenoid that produces a 5 T magnetic field and whose yoke is also used as muon detector and tail catcher. [30]

m^2 and is seated in a 5 T magnetic field. Like for the ILD, the interaction point is in the middle of the detector. The inner part of the detector is a dry air cooled vertex detector constructed of a barrel system and two disks for the forward regions with several layers of silicon pixels. The vertex detector time-stamps each hit to assign it to a bunch crossing. It is followed by the ECAL and then the HCAL. Both are required to have a very high resolution. The ECAL consists of 30 layers that comprise an active silicon and an absorbing tungsten layer. The active layer contains $5 \times 5 \text{ mm}^2$ pixels. The whole ECAL has a depth of $26 X_0$ and $1 \lambda_1$. The HCAL also is a sampling calorimeter with a depth of $4.5 \lambda_1$, but different options for the setup are still under discussion. The vertex detector, ECAL and HCAL are enclosed by a superconducting solenoid that creates a 5 T magnetic field. The flux return yoke of the magnet coil also serves as muon filter and tail catcher with a spatial resolution of a few centimetres. For that purpose, strip detectors arranged in about nine layers are being discussed. [28]

4 CALICE AHCAL

The CALICE collaboration is responsible for the development of the three main parts of the ILD: the ECAL, the HCAL and the tail catcher/muon tracker (TCMT). Since 2006, CALICE is engaged in a testbeam programme where different prototypes of the detectors are tested in various testbeams. For all detector parts, different proposals are tested:

- **ECAL:** The ECAL should have a depth of $24 X_0$, which is achieved with 30 tungsten layers. The active layers, made out of either silicon diodes or scintillators, are planned to be segmented in cells in the size of 5 to 10 mm.
- **HCAL:** The HCAL is supposed to consist of 48 layers. As absorber material stainless steel will be used, this results in a depth of $5.5 \lambda_1$. There are two different approaches for the active layers. The digital HCAL (DHCAL) consists of $1 \times 1 \text{ cm}^2$ cells filled with gas. In the analogue HCAL (AHCAL), the readout is realized by $3 \times 3 \text{ mm}^2$ scintillator tiles read out by SiPMs. The DHCAL allows a higher spatial resolution but gives, in contrast to the AHCAL, no information about the deposited energy.
- **TCMT:** The TCMT is going to be integrated into the iron yoke. Possible setups are the use of gas detectors, silicon scintillators or plastic scintillators. [1]

The analysis in this thesis is about a prototype of the AHCAL, thus, in the following, only the working principle of the AHCAL and its components are described.

4.1 HCAL Basic Unit

The HCAL Base Unit (HBU) is a segment of the active layers of the AHCAL. Three slabs of five to six HBUs together form one layer. Each HBU contains 144 channels with a size of $3 \times 3 \text{ cm}^2$ each which results in a total HBU size of $36 \times 36 \text{ cm}^2$. The height of one HBU has to be smaller than 2 mm since it needs to fit in the gap between two absorber layers. [28]

The backside of the board is mounted with 144 individually wrapped scintillator tiles (one for each channel) that are glued to the HBU. Their signals are collected by 144 SiPMs and then read out by the SPIROC2b ASICs (Application Specific Integrated Circuit). For calibration, each channel has its own individually controlled LED. [29] Each AHCAL layer is controlled by a Central Interface Board (CIB) that controls the SPIROC2b, the voltage supply, and the calibration system. The gain calibration of the SiPMs (further explanation in section 4.1.3) is controlled by the CALIB2 board. It

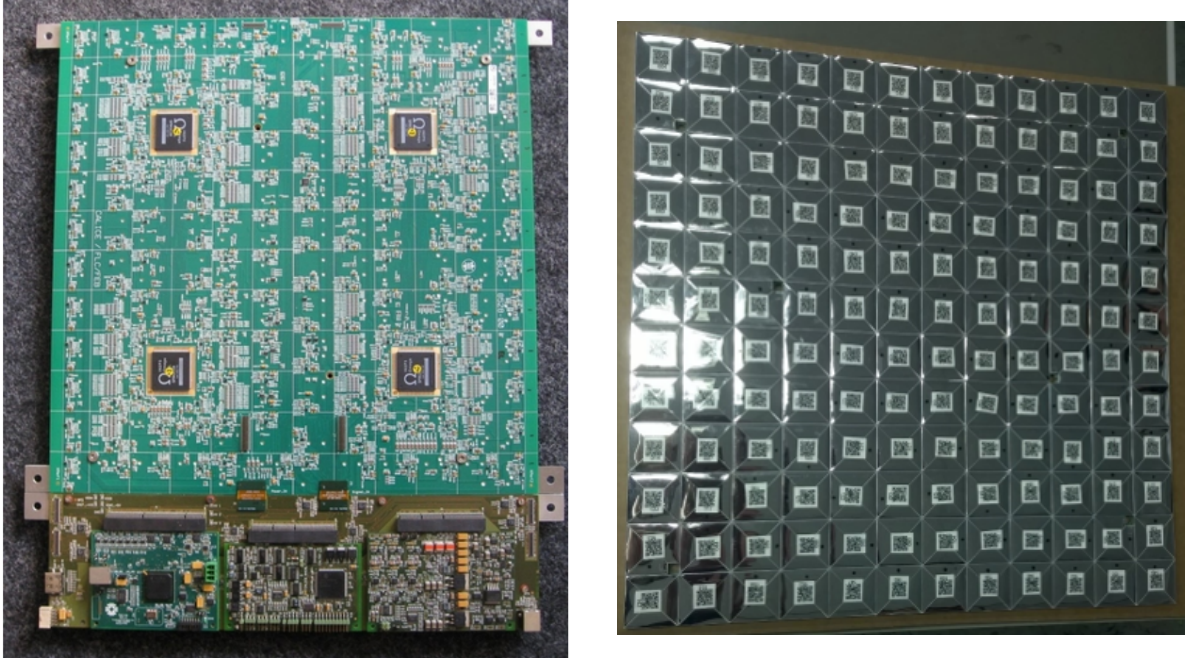


Figure 4.1: Left: Picture of HBU constructed of four SPIROC2b ASICs; DAQ interface modules are below the board [29]; right: Picture of wrapped scintillator tiles that are mounted on the bottom side of the HBU [31]

sends a calibration voltage and trigger pulses to the LED system on the HBU. When synchronising the trigger pulses with the trigger pulses of the SPIROC2b, the data can be used for gain calibration. The voltage to operate the HBUs is generated by the POWER2 board. It has three input supply voltages of 6 V, 12 V, and a variable high voltage of around 50 V. The 6 V input feeds the SPIROC, the 12 V input is responsible for the CALIB2 board, and the high voltage line sets the SiPM bias voltage. This board is also responsible for the power pulsing of the HBU electronics. To enable the communication between the different components, a Detector InterFace (DIF) board is used. It generates a clock signal and all SPIROC2b steering signals and is responsible for data transfer to the Data Acquisition (DAQ) system. [22]

There have been several different designs of the HBU. The most current ones are the HBU3 and HBU4, that have been designed for their use with power pulsing. Also, the designs for the scintillator tiles and some implementations, e.g. the position and type of the LEDs, were changed.

4.1.1 SPIROC2b ASIC

The SPIROC2b (Silicon Photomultiplier Integrated ReadOut Chip) is an ASIC that is used to run the silicon photomultiplier. The chip can control up to 36 SiPMs by distributing their individual bias voltages. At the same time, it reads out the signals

4 CALICE AHCAL

from the SiPMs in memory cells that can hold up to 16 events per channel before they are read out. The reading is done by a 12 bit Wilkinson ADC (analogue to digital converter). In the setup used in this analysis, the zeroth memory cell is broken, thus only 15 events can be saved. The chip is designed for the use with power pulsing and has a very low power consumption of $25 \mu\text{W}$. [22]

4.1.2 Scintillator tiles

The scintillator tiles used for the HBUs are organic scintillators. Organic scintillators usually consist of a solvent, a scintillating material, and a second fluorescent that acts as a wavelength shifter. Traversing ionizing particles lose energy in the solvent. This energy is transferred to the particles of the scintillating material. The energy transfer excites the particles into a higher state and, when falling back to their ground state, emit light. The light is absorbed by the fluorescent, which re-emits the light at a longer wavelength.

Here, polystyrene is used as solvent, mixed with $\sim 1\%$ of p-terphylene as main scintillating material. Approximately 0.003% of POPOP are used as wavelength shifter. [32] In contrast to HBU1, HBU2 and HBU3, where the tiles had a wavelength shifting fibre in the middle, the tiles are now used with the center dimple design. In this design, a small dimple is drilled into the middle of the tile to leave space for the SiPM. The tiles are individually wrapped in a reflective foil to reduce the crosstalk between them. The foil has two small holes: one, to allow the SiPM to be placed in the dimple, and the other to let the light from the LEDs reach the tile for calibration.

4.1.3 Silicon photomultipliers

When a photon moves through silicon it can create an electron-hole pair by transferring its energy to an electron, which will then move from the valence to the conducting band. The absorption of the photon depends on its wavelength, thus the detection efficiency is also wavelength dependant. To produce a photo diode from silicon, a p-n junction with a charge carrier free depletion area is created. Then, a reverse bias is applied. This creates an electric field that will accelerate the electrons towards the cathode and the holes towards the anode, where a current can be measured.

Silicon photo diodes often are operated in Geiger mode to achieve a high amplification of the signal. In this mode, a high reverse bias ($> 5 \cdot 10^5 \text{ V/cm}$) is applied in the depletion area. Now, if a charge carrier is created, it will be accelerated until it gets enough energy to ionize further atoms and create more electron-hole pairs that will also contribute in the ionization cascade. The cascade will spread through the whole volume and by that the silicon becomes conductive. This creates a macroscopic current. The voltage at which the silicon becomes conductive is called breakdown voltage V_b . In Geiger mode, the applied reverse bias voltage V_{bias} needs to be higher than the breakdown voltage, otherwise no cascade will emerge. The difference between the bias voltage and the breakdown voltage is called overvoltage ΔV . The cascade is stopped with a process called quenching: resistors lower the current drawn by the

4 CALICE AHCAL

diode after breakdown which lowers the reverse bias in the diode below the breakdown voltage and the cascade dies out. After that, the diode recharges and can then detect further photons. The time that the diode needs to recharge is called recovery time. During this time, no photons can be detected.

In silicon photo diodes the signal is independent of the energy or number of incoming photons, since the particle avalanche allows no conclusions on the primary number of electron-hole pairs. To still achieve the possibility of measuring the magnitude of the photon flux, hundreds to thousands of silicon diodes per square millimetre are integrated in parallel into a dense array. The measured signal is the sum over the signals from each pixel. Each pixel still works independently from the others with its own quenching resistors. Thus, if one pixel is triggered, the others will remain active and are able to detect further photons, but photons usually trigger several pixels at once. Since all diodes have the same output charge when firing, the sum over all pixels forms a quasi-analogue signal that allows to draw conclusions about the light pulse amplitudes. [33] When the intensity of the light pulse is too high, the SiPM can saturate. This means that all diodes are triggered at once and a maximum signal is reached. At this range, the output is not linear anymore [34].

4.1.3.1 Properties

- **Photon Detection Efficiency:** The photon detection efficiency is the probability that a photon interacts with a photo diode and produces an avalanche. It is a function of the wavelength of the incident particle, the bias voltage and the material composition of the diode. If the bias voltage is higher, the probability increases that an electron-hole pair will not recombine immediately and thus the photo detection efficiency is increased. [33]
- **Dark Count Rate:** The dark count rate is the most dominant noise source in SiPMs. Dark counts occur, when a diode is fired due to a thermal excitation or quantum tunnelling electrons. The dark count rate depends on the active area, the temperature, and the applied electric field and thus on the bias voltage. The signals from spontaneous effects are indistinguishable from signals that are generated from photons. To minimise the influence of the dark count rate, a threshold can be defined that requires several pixels being triggered at the same time. [33]
- **Optical Cross Talk:** A contribution to the noise is also made by the optical crosstalk. Crosstalk occurs, when an avalanche in one pixel initiates a cascade in one of its neighbouring cells. It depends on the bias voltage and the material of the diodes. The second pixel can be triggered by a secondary photon in three different ways: it can travel directly to the neighbouring cell, it can be reflected at the bottom of the silicon substrate, or it can be reflected on the window on top of the diode. [33]
- **Afterpulsing:** Another source of noise is the afterpulsing. It can occur when

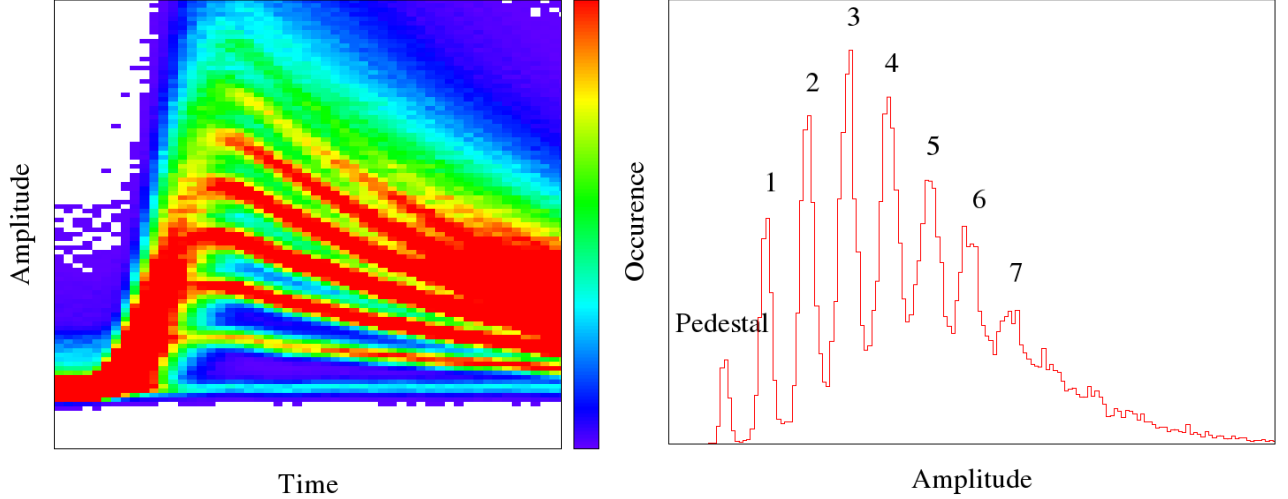


Figure 4.2: Example for a single photon spectrum; left: Time resolved distribution; right: Single photon peak structure derived from picture on the left [22]

a charge carrier gets trapped in defects of the silicon. When the charge carriers escapes, usually after a few nanoseconds, it can trigger another cascade called afterpulse. If the afterpulse develops within the recovery time it will have no influence on the result. But if the afterpulse is generated after the diode is active again, it will be counted as signal and thus affect the measurement. The probability for afterpulses rises with increasing bias voltage, and number of defects in the silicon and thus also with higher numbers of radiation damage. [33]

- **Gain:**

The gain G is the amount of charge that is created by each detected photon. It is defined as:

$$G(T) = \frac{C \cdot (V_{bias} - V_b(T))}{q} = \frac{C \cdot \Delta V(T)}{q} \quad (4.1)$$

with:

$$\begin{aligned} C &= \text{Diode capacity} \\ V_{bias} &= \text{Bias voltage} \\ V_b &= \text{Breakdown voltage} \\ \Delta V &= \text{Overvoltage} \\ q &= \text{Electron charge} \\ T &= \text{Temperature} \end{aligned}$$

Since the bias voltages for each SiPM in the AHCAL are slightly different, the gain factors have to be determined for each one separately. Therefore, a Single

4 CALICE AHCAL

Photon Spectrum (SPS) is used. An example for a SPS is given in figure 4.2. On the left, the time resolved distribution is shown, this can be measured for example with an oscilloscope. The right image is an histogram of the measured values from the figure on the left. In this example, the single peak structure is clearly visible. The first peak is generated when no signal is measured, it is called pedestal peak and is created by the electronics. The other peaks are called pixel peaks. The first one is created when one pixel is fired, the second one when two pixels are active and so on. Since there is background noise coming from the electronics, the pixel peaks are not sharp but slightly smeared.

The distance between two pixel peaks is always the same. It can be calculated for example by fitting with a multi Gaussian fit.

The gain also depends on the temperature: with increasing temperature the gain is decreasing. This behaviour results from the temperature dependence of the breakdown voltage. With increasing temperature, the probability for charge carriers scattering with the crystal lattice becomes higher which augments the energy loss of the charge carriers and thus the breakdown voltage rises and therefore the gain decreases. [33]

- **MIP calibration:** The MIP calibration has to be performed to build a connection between the number of fired pixels and the energy of the incident particle. For this calibration a spectrum of the measured charge generated from Minimum Ionizing Particles (MIP) is used. Since MIPs are the minimal energy deposition that can be measured, the most probable value of their spectra can be used as unit energy. The ratio of the most probable value and the gain value is called light yield and is defined as the number of pixels of the SiPM that fire upon being hit by an MIP [35].

4.2 Test beam setup

In this thesis, data from a testbeam in July and August 2016 at DESY (Deutsches Elektronen SYnchrotron) in Hamburg is analysed. In the following, the testbeam facility and the detector setup are described.

4.2.1 Test beam facility

DESY II is an electron/positron synchrotron located at the research facility DESY. A synchrotron is a special kind of ring accelerator to reach high energies. It usually consist of linear acceleration lines with high frequent electrical fields in resonators and deflecting magnets. With increasing energy of the particles, also the magnetic field has to be raised. [17]

The accelerator ring at DESY II has a circumference of 292.8 m and is usually used as injector for DORIS and PETRA, two other accelerators in Hamburg [36]. But DESY II also has three test beam lines (TB 24 was used during the testbeam for CALICE) where bremsstrahlung emitted by DESY II can be used. To create the bremsstrahlung,

4 CALICE AHCAL

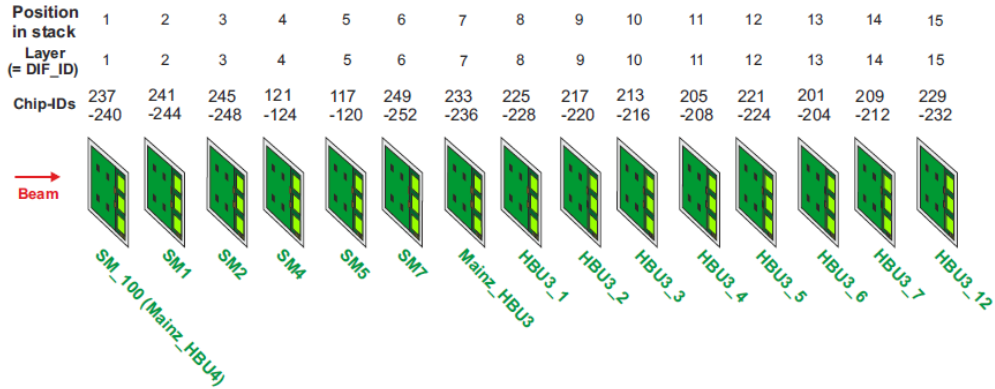


Figure 4.3: Setup of the AHCAL prototype in July and August 2016 at DESY

a carbon fibre target is placed in the beam line. The emitted photons hit a metal plate called converter that creates electron-positron pairs. Finally, a dipole magnet spreads the beam on a collimator where the final beam with a selected energy range is cut of. The final beam can contain electrons or positrons with an energy up to 6 GeV. [37]

4.2.2 Detector setup

The goal of the testbeam was on the one hand to see the impact of power pulsing, since it was tested here for the first time, and on the other hand to use a further developed version of the HBUs in a larger number. In total, three different HBU versions have been used.

The used detector was an engineering prototype of the AHCAL. It consisted of 15 layers with one HBU each of which contains 4 ASICs. Since each HBU consists of 144 channels, the whole setup contains 2160 channels (see fig. 4.3). Each ASIC has its own unique number with which it can be allocated. This number is shown in the figure as Chip-ID.

The boards are equipped with different SiPMs, thus their performance differs. The first 6 layers are equipped with the HBU4 that have new Hamamatsu silicon PMs with a low crosstalk of 2-3%, layer 7 with an older version of the HBU4 has an older Hamamatsu SiPM type with a high crosstalk of about 25%. Layers 8 to 15 with HBU3 are equipped with Sensl SiPM. Also, the position of the SiPMs differs. For the layers with HBU4 the SiPMs are surface mounted. That means that they are seated between the board and the scintillator tile which has a small dimple drilled into it to make space for the SiPM. The tiles for the HBU3 have light shifting fibres embedded into them that transport the light to the small side of the tile, where the SiPM is placed. This setup is called side mounted. A summary of these details can be found in table 4.1. Apart from the different SiPMs there are some more differences between HBU3

4 CALICE AHCAL

Layer	SiPM	HBU type	
1-6	Hamamatsu MPPC S13360-1325pe [38]	HBU4	surface mounted
7	Hamamatsu MPPC S12571-25P [39]	HBU3	surface mounted
8-15	SensL B [40]	HBU3	side mounted

Table 4.1: Information about the layers used for the AHCAL prototype in July and August 2016

and HBU4. The positions of the LEDs are changed and also another type of LEDs is used, which changes the voltage for the LED calibration.

For measuring showers, absorbing layers made out of steel are placed between the detector layers, the setup without absorbers is called airstack.

4.2.3 Data taking

For taking the data, different ways were used that can be divided in three groups: Gain calibration, MIP calibration and electron shower data. The gain and MIP calibration are both performed in the air stack where the absorbing layers are removed. At first, to estimate the noise of the electronics, a so called pedestal run while the 144 LEDs every HBU is equipped with, are switched off is taken. Then, the LED voltage is increased from usually 3500 mV in steps of 50 mV until around 8000 mV is reached. The LEDs will fire short light pulses (~ 10 ns) at a low amplitude. When a photon hits the SiPM, a signal is generated and a single photon spectrum can be measured. The light pulse has to be short to avoid a saturation of the SiPMs. The gain runs are repeated frequently to constantly monitor the gain.

MIP measurements usually are performed with muons but since DESY has no muon beam available, an electron beam is used instead to simulate MIPs. Electrons can be used for this task as long as they do not shower, to achieve that, the absorber layers have to be removed for this measurement. The default setup consists of the previously shown 15 layers (see figure 4.3) but since the MIP signal becomes diminished for the later layers, the measurement is repeated three times while removing five boards from the front each time. Due to the relatively narrow diameter of the beam, it has to be moved systematically over the surface of the board in order to reach every channel. Since the beam can cover four channels at a time, there have to be at least nine measurements per ASIC.

The measurement of the shower data is performed with an electron beam at five different energies from 1 to 5 GeV in steps of 1 GeV. For power pulsing, the data for 3 and 4 GeV are missing, since in the runs at 3 GeV, the last 9 layers had to be turned off and for 4 GeV, there was a software problem. The beam is centred to the middle of the boards. At first, several runs were taken in continuous mode, then the mode was switched to power pulsing and runs with different power pulsing frequencies were taken. In this thesis, only power pulsing runs with ILC timing structure of 500 clock cycles are used.

5 Software

5.1 Gain calibration

To compute the gain, an adaptation of the existing software developed at DESY is used. It consists of several steps that will be described in the following. For this first part of the calibration procedure, data obtained from the LED runs is used.

The raw data from the test beam is first converted into root files [41] without using event building. These root files are more manageable than the raw data and contain trees for the bunch and chip ID, cycle, ASIC and event number, channel, TDC and ADC data, x- and y-position and hit and gain bit.

Then, the pedestal offset (as described in the paragraph about gain in section 4.1.3.1) is calculated. The input for the pedestal calculation is data from a LED run with the LED voltage set to 0 V. Since the pedestal results from electronic noise and dark count, it needs to be calculated memory cell-wise. In this setup, memory cell 0 is defective and thus has no entries and will not be used for calibration or the analysis. For the pedestal determination, each memory cell with a Gaussian-like distribution (usually around 200 to 300 ADC ticks) is fitted with a Gaussian curve. An example for this is given in figure 5.1. If the distribution does not fulfill the criteria, the pedestal value

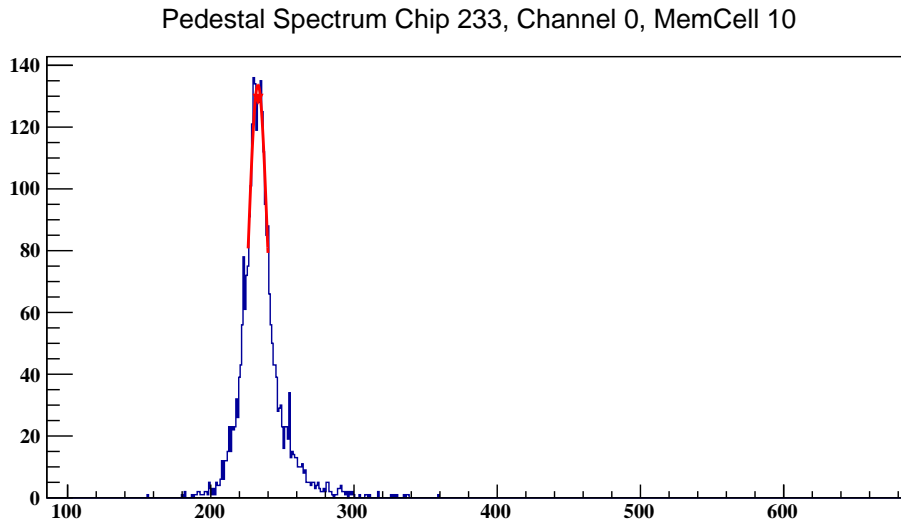


Figure 5.1: Example for a Gaussian fit for the pedestal correction (Run 43510) for chip 233, channel 0, memory cell 10

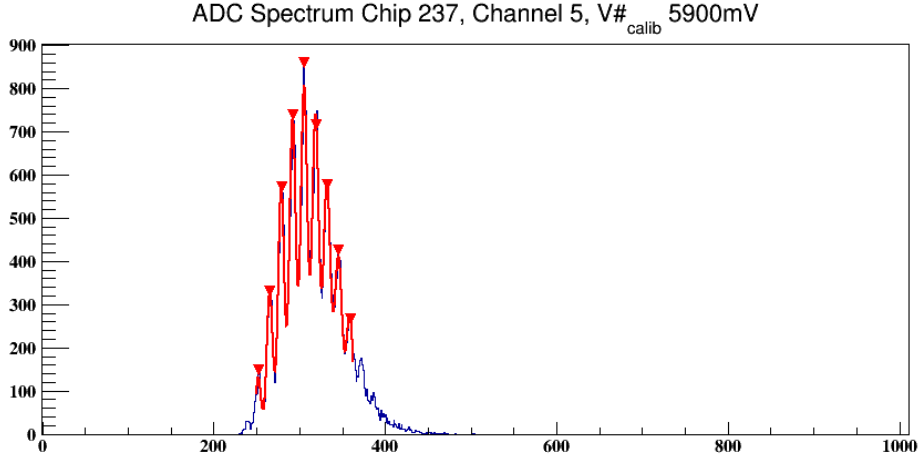


Figure 5.2: Example for a multi gaussian fit for chip 237, channel 5, LED voltage: 5900 mV; The recognised pseudo peaks are marked as red arrows

for this memory cell is set to zero. From the mean value, a pedestal correction value is derived that describes the shift of the pedestal with respect to the first memory cell. The reason behind this is to shift all the memory cells to the same base level to be able to merge the information of all memory cells for the gain calibration, which is conducted in the next step.

After applying the pedestal correction cell by memory cell to the gain calibration data obtained with the LEDs, an ADC spectrum for each channel is created. In order to rule out bad spectra, maxima, which are called pseudo peaks, are searched for using the GetNPeaks root function. If there are enough pseudo peaks and they are in similar distances to each other, the gain is calculated. As another check the mean of the spectrum is calculated. The spectrum is only taken into account if the mean is below 3000 ADCs to make sure that it is not saturated yet.

Then, two different methods to calculate the gain are used: a multi Gaussian fit and a Fast Fourier Transformation (FFT) are performed.

The multi Gaussian fit consists of the sum over several Gaussian fits. It has the following form:

$$f(x) = \sum_i \frac{c_i}{\sqrt{2\pi\sigma_i^2}} \cdot e^{-\frac{(x-\mu_i)^2}{2\sigma_i^2}} \quad (5.1)$$

with:

i = Index of the fitted peak

c_i = Amplitude

σ_i = Standard deviation

μ_i = Mean

5 Software

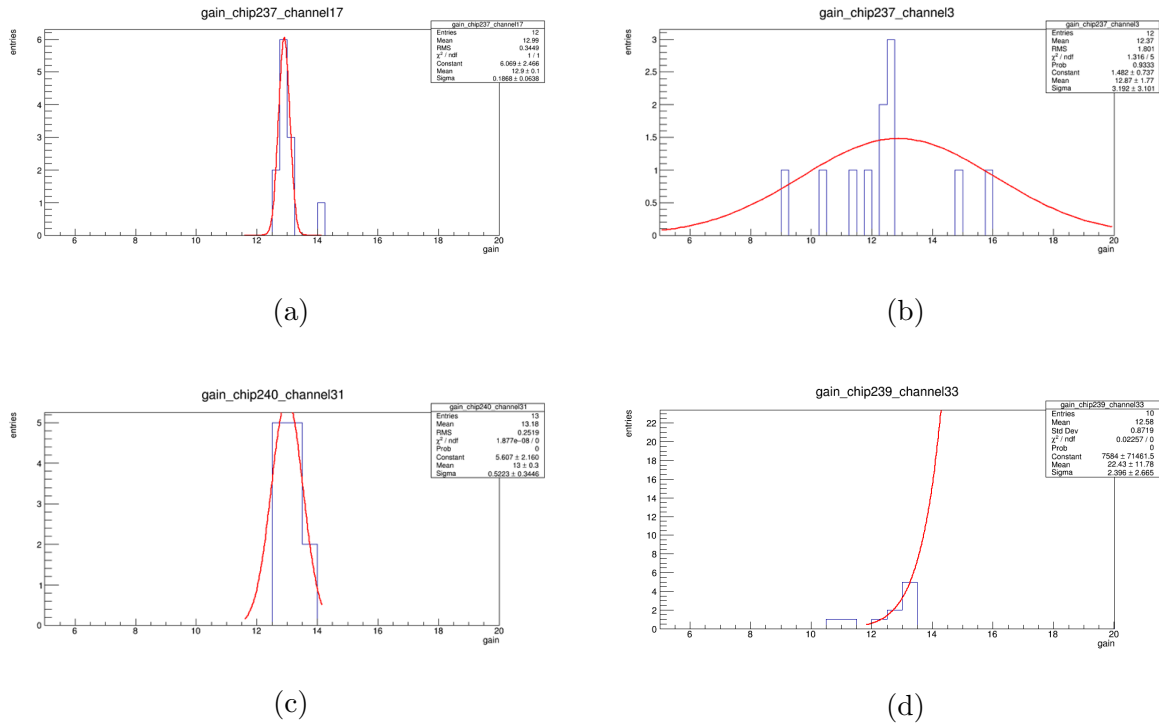


Figure 5.3: Second step of gain calibration: distributions of gain values per channel; (a): Fit with 10% fitting range around the maximum peak; (b): Fit with wider fitting range over whole histogram; (c): Fit with small fitting range after rebinning; (d): Non-converging channel, mean of histogram is used

The fit uses the information of the pseudo peaks as starting values. The gain is determined by calculating the distances between the mean of the second and the penultimate peak and averaging over them. An example for the fit is given in figure 5.2. The red arrows mark the positions of the recognized pseudo peaks.

The FFT is proceeded with the FFT tool from root. It is an algorithm to quickly calculate the discrete Fourier transformation that shifts a signal into the frequency domain where it can be analysed. To derive a gain value, a peak in the first 10% of the histogram is searched for that is then fitted with a Gaussian. This is then converted back to the original domain to get the gain value. Since 88 runs at different LED voltages were used and each one possibly delivers a value for each channel, a single value per channel needs to be extracted. To do so, all the gains for one channel are filled in a histogram which is then fitted with a Gaussian curve where 10% around the highest bin are taken as fit boundaries. When the mean lies within a range of 20% around the maximum bin, it is assumed that the fit converges. If the fit does not converge properly, these channels are fitted again but with a wider fitting range over the whole histogram. If this fit does not converge either, the histogram is rebinned

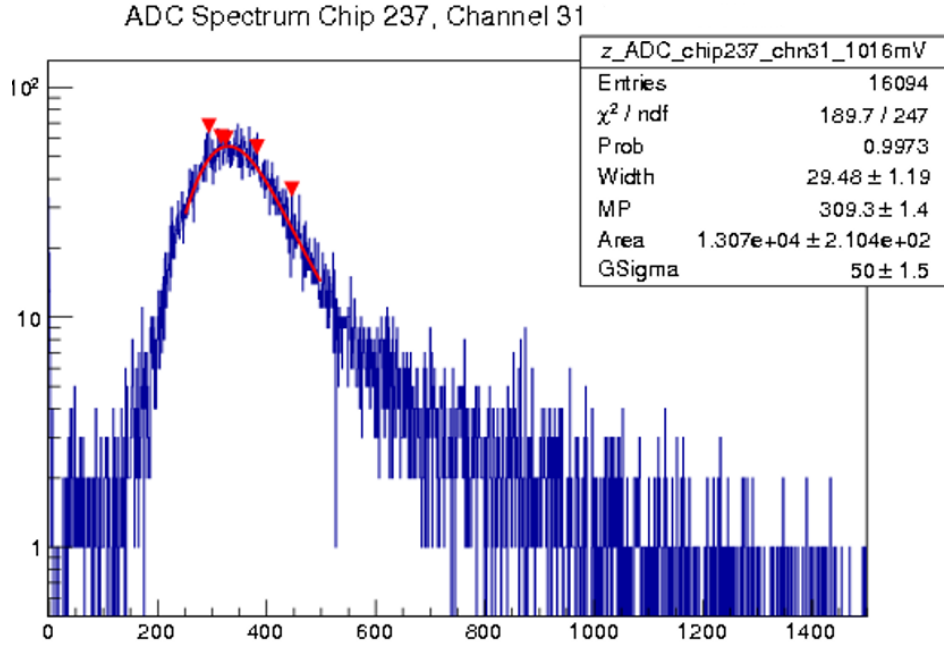


Figure 5.4: Example of a Landau-Gaussian fit to calculate the MIP value; distribution after TDC cut. The red arrows are remaining markers for the pseudo peaks from the adaptation of the gain software, they are still drawn but not used

(two neighbouring bins are merged together) and fitted again with a smaller fitting range. For the remaining channels, the mean of the histogram is used. Examples for these cases are depicted in figure 5.3.

5.2 MIP calibration

The data for the MIP calibration is taken in the airstack in MIPs runs with a narrow electron beam that simulates MIPs. To determine the value of the MIP energy the software already used for the gain is slightly adapted. The conversion to root files and the pedestal fits are performed analogously to the process described in section 5.1. Then, the step for the gain calibration is changed so that it still produces the channelwise ADC spectra but without performing the multi Gaussian fit. Additionally, the data below 1500 TDC are cut off to remove the noise peak. This noise peak occurs because the timing window in which the TDC is open is a bit longer than the actual signal. During that short time period, the TDC collect noise that should not be taken into account for the MIP calibration.

To finally calculate the MIP value the ADC spectrum is fitted channelwise with a

Landau distribution convoluted with a Gaussian distribution. The convolution is done numerically by root. The most probable value (MP) from the fit is taken as MIP value. An example for the fit is given in figure 5.4.

5.3 Reconstruction

The measured data are stored as raw data. They contain the measured signals in each channel, called hits, that are built up to events. Events are selected by trigger conditions to make sure that one event only contains one incoming particle and thus also only one electromagnetic shower. For each hit, information like the chip and channel number, the measured signal, and the beam and hit bit is stored.

The numbers from the raw data have to be converted into a more readable format. To do so, the data is reconstructed with Marlin [42]. Its advantage is that it is highly modular and can be easily adapted to different detector setups. For this thesis, the Marlin version 01-09 is used. In the end, the reconstructed data is saved in root trees for easy visualisation and further analysis.

For reconstruction, the data is read in and the events are splitted to separate different types of entries, e.g. one collection for the temperature information and one collection for the hit data. Since the detector geometry is implemented in a database, the hits can be assigned to their actual position in the detector (e.g. the chip number is assigned to the layer number). After that, calibration factors like the gain, MIP energy, and pedestal values are read from the database and applied to the hits to convert them from ADC counts to MIP energy units. After processing, the data is written in one root file for the temperature information and one file for the physics data.

5.4 Simulation

In order to test if the detector behaves as expected, it is important to compare the data with simulations. For this thesis, the Monte Carlo simulations are produced with DD4hep [43]. DD4hep is short for Detector Description Toolkit for High Energy Physics Experiments. It is developed to provide a framework for the description of detectors for simulation, reconstruction as well as analysis.

The simulation process can be divided into two steps. First, particles with a given energy are produced. The distance of the particle source from the detector, the position of the beam, and the beam profile can be varied. In this thesis, a Gaussian beam profile is used and the distance between the particle source and the detector is set to 10 m. The beam position is shifted by -1 mm in x- and -0.5 mm in y direction. Then, the behaviour of those particles in a given detector volume is simulated. The detector volume can be changed according to the used detector setup via a geometry file. The path of each particle is being followed for each of its steps on the way through the detector material. At each step, an interaction is chosen based on the implemented model, that takes into account the probabilities for all allowed types of interactions. The models that decide over the interactions are called physics lists. A selection of

5 Software

physics lists is available, from which a suitable one has to be chosen according to the used energy range and particle types. In this thesis, the physics list `QGSP_BERT` is used. Created daughter particles are also tracked until their energy falls under a given threshold. Each interaction of a particle in a cell generates a hit. All of those simulated hits are written into a raw data file.

After the hits are simulated they are digitised. This step simulates the electronics of the detector and transforms the energy of the hits into measured signals.

Finally, the simulated data is reconstructed with the same reconstruction process described above for data.

5.5 Temperature correction

Layer	Gain slope [%/deg. C]	MIP slope [%/deg. C]
1-6	-0.7	-1.3
7	-1.5	-3
8-15	-0.5	-1

Table 5.1: Temperature dependence of the gain and MIP energy values [44]

As described in section 4.1.3, the gain and the MIP correction factors depend on temperature. A possible temperature change in the detector needs to be corrected for, since the data used to determine the gain, the MIP energy and for physics analysis was taken at different times. Furthermore, a decrease in temperature might occur. This is caused by the electronics switch off when not needed in power pulsing mode. To apply the temperature correction, the mean temperature of the six sensors per layer is computed per run.

The temperature of the LED and MIP runs are taken as reference and the other temperatures are corrected with respect to them. Since the values used in the simulation are the ones that are computed at the reference temperature, there is no correction needed for it. The temperature difference is computed layer-wise and the correction factor is calculated according to the values from table 5.1. Then, the temperature correction factors are applied to the data after the reconstruction.

6 Analysis of test beam data

6.1 Calibration of SiPM gain

In this section, the results from the gain measurement are shown. As described in section 5.1, a multi Gaussian fit is used to calculate the gain values from the ADC spectra. The results for chip 237, channel 11 at nine different voltages are displayed in figure 6.1. It can be observed that the number of pixels increases with higher LED voltages and the distribution shifts to higher ADC values. This is expected because each peak corresponds to a certain number of photons and with higher LED voltage, more photons are emitted and thus, more pixels are fired and more pixel peaks are

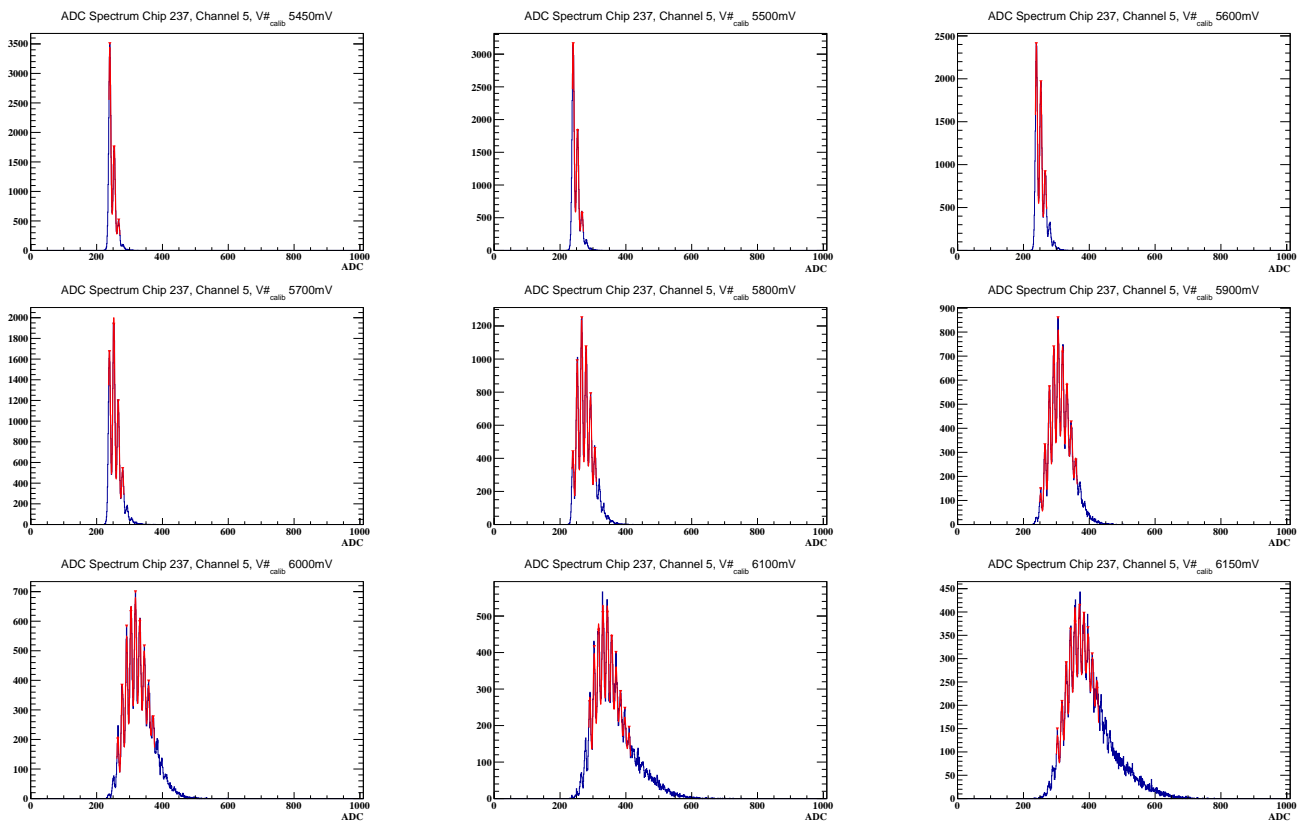


Figure 6.1: Display of single photon spectra for chip 23, channel 11 at different voltages. It can be observed that the number of pixels increases with higher voltages and the distribution is shifting to higher ADC values

6 Analysis of test beam data

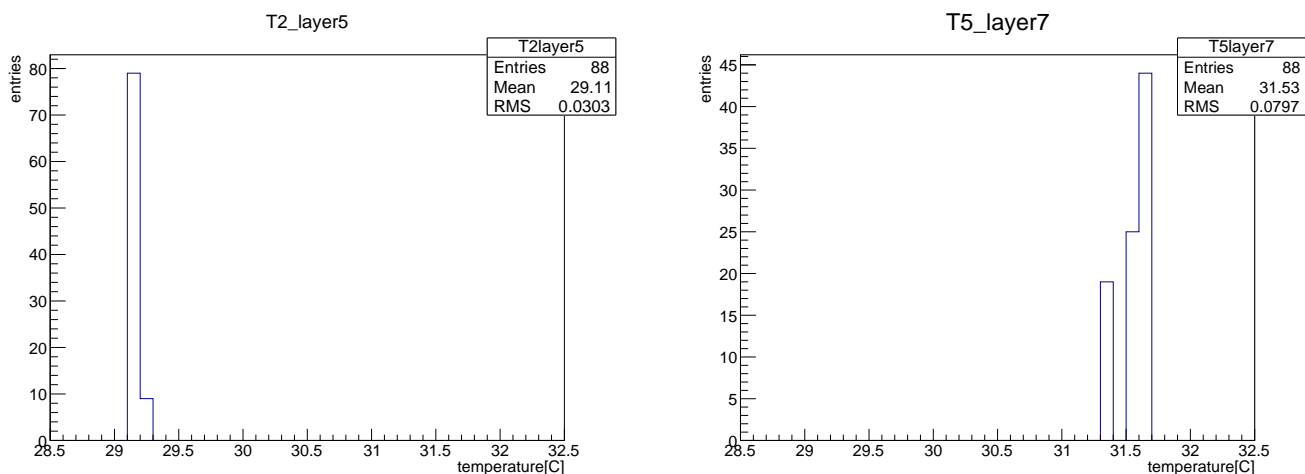


Figure 6.2: Temperature distribution over 88 LED runs. Left: lowest RMS; right: highest RMS

visible in the ADC spectrum. This also explains the shift of distribution to the right. Since the gain is temperature dependent, it has to be ensured that there are no significant fluctuations during the runs for the gain measurements. Therefore, data from the six measuring points of each HBU were taken during 88 LED runs and plotted. Figure 6.2 shows the distribution of the temperature with the highest and the lowest RMS. All distributions only vary by not more than 0.3°C . This difference is small enough to neglect temperature corrections among the LED runs. The resolution of the temperature sensors is 0.1°C .

The distributions lie in different temperature regions because some parts of the HBU, e.g. near the SPIROC2b, are much warmer than other parts, for example next to the cooler.

Next, the gain calculated by the multi Gaussian fit is compared with the one from the FFT. Therefore, both obtained gains are plotted against each other channelwise as shown in figure 6.3. A clear correlation can be observed. Notably, the gain calculated with FFT is in some cases much higher than the corresponding value from the multi Gaussian fit. It can be concluded that the multi Gaussian fit is more reliable than the FFT and thus, it will be used for further analysis.

Finally, the gain for each channel is calculated. Since 88 runs were used and each one possibly delivers a value for each channel, a way has to be found to extract one single value per channel. To do so, two different methods were compared in order to choose the optimal one.

First, an approach with different cuts is tested. The Gaussian fit to get the gain delivers a value for χ^2 , a distribution of those are shown in figure 6.4. The first cut is undertaken at 5. Since the fits for some channels are not converging but still have a good χ^2 (for example, see figure 6.5) an additional cut on the gain is performed. Here, the threshold is put to 20. After the cuts, the gain for the channel is calculated by

6 Analysis of test beam data

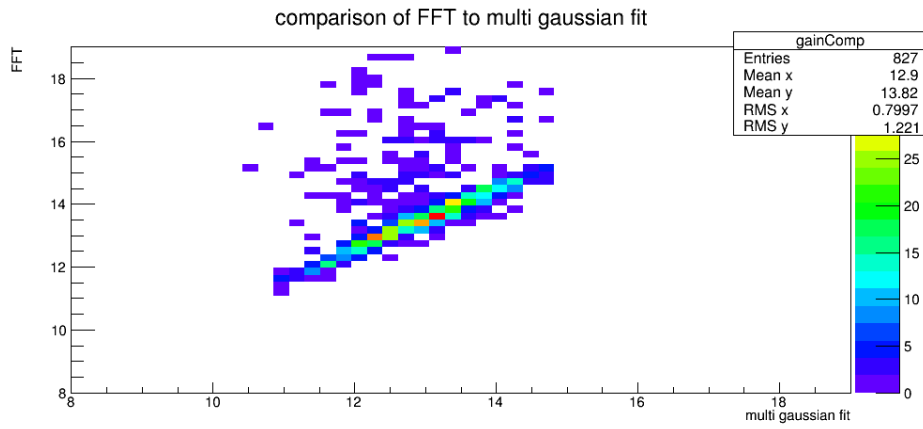


Figure 6.3: Comparison of the gain calculated with a multi Gaussian fit and FFT

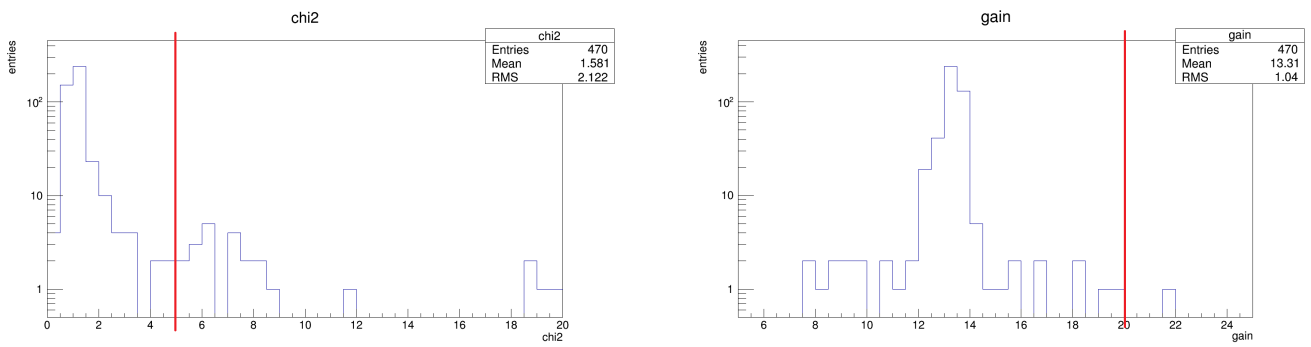


Figure 6.4: Distribution of χ^2 (left) and gain (right) from multi Gaussian fits and used cuts (red lines)

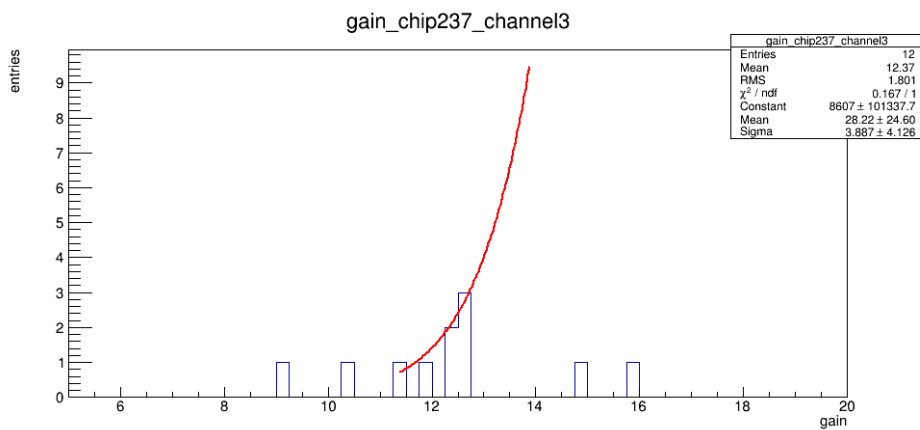


Figure 6.5: Example for a non-converging fit with good χ^2

6 Analysis of test beam data

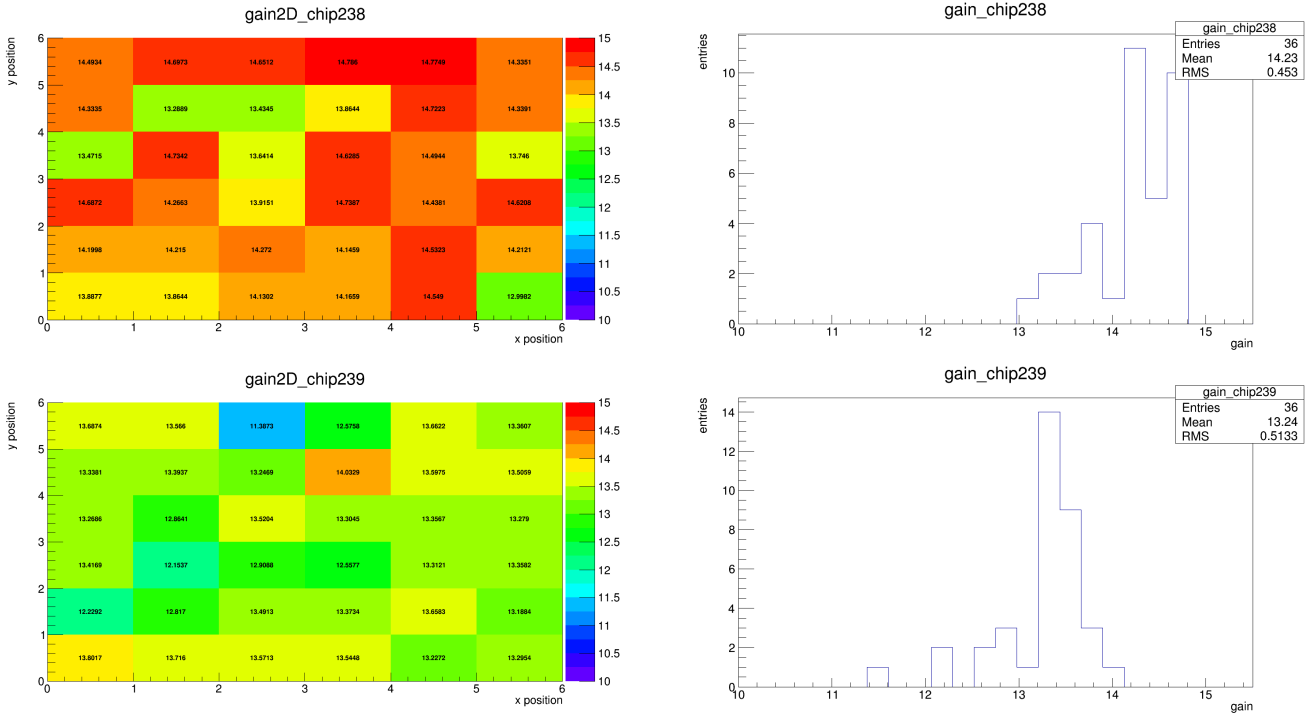


Figure 6.6: Chipwise gains and corresponding distributions

averaging over the remaining gains. Examples for the chipwise results are displayed in figure 6.6. Since the gains in another testbeam could vary from these, the cuts cannot be applied universally, thus the more general method described in 5.1 is preferred. The results are shown in figure 6.7, the marked channel is one of those where the fit is not converging.

The first step with the Gaussian fit with a fitting range of 10% around the highest bin is successful for 95.0% of the channels. The channels fitted with a wider fitting range result in another 1.2% successfully fitted channels. Rebinning works for additional 3.0%. The remaining channels, where the mean of the histogram is used, are 0.8% of the total.

The relative spread of the with the new method obtained gain values is calculated by dividing the RMS with the mean (see fig. 6.8). This allows a conclusion on the quality of the used SiPMs, since a small spread is preferable. For these SiPMs, the relative spread is smaller than 5%, which fulfils the requirements of a spread smaller than 10%.

In the end, the values are compared with the values obtained at DESY with a similar method. The difference for each channel is shown in figure 6.9. Both methods seem to deliver similar values.

6 Analysis of test beam data

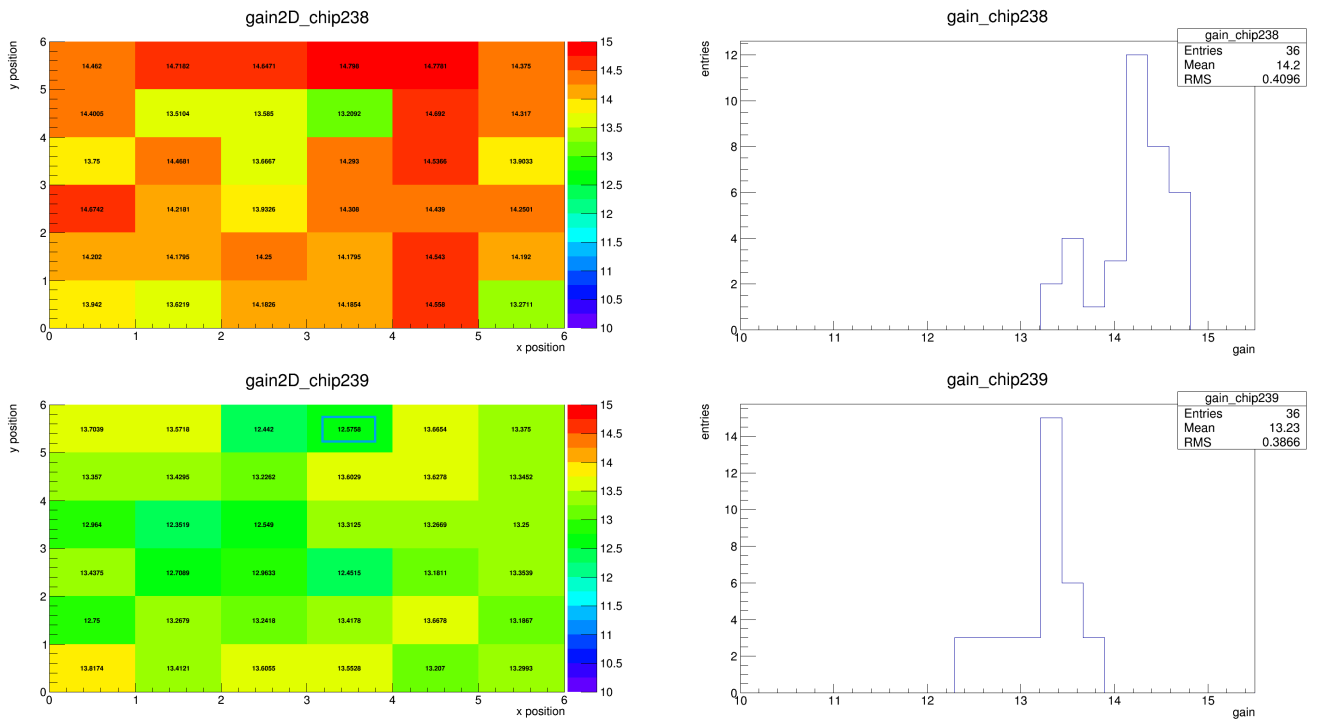


Figure 6.7: Chipwise gains and corresponding distributions with new method. For the marked channel, the fits are not converging and the mean is used

6 Analysis of test beam data

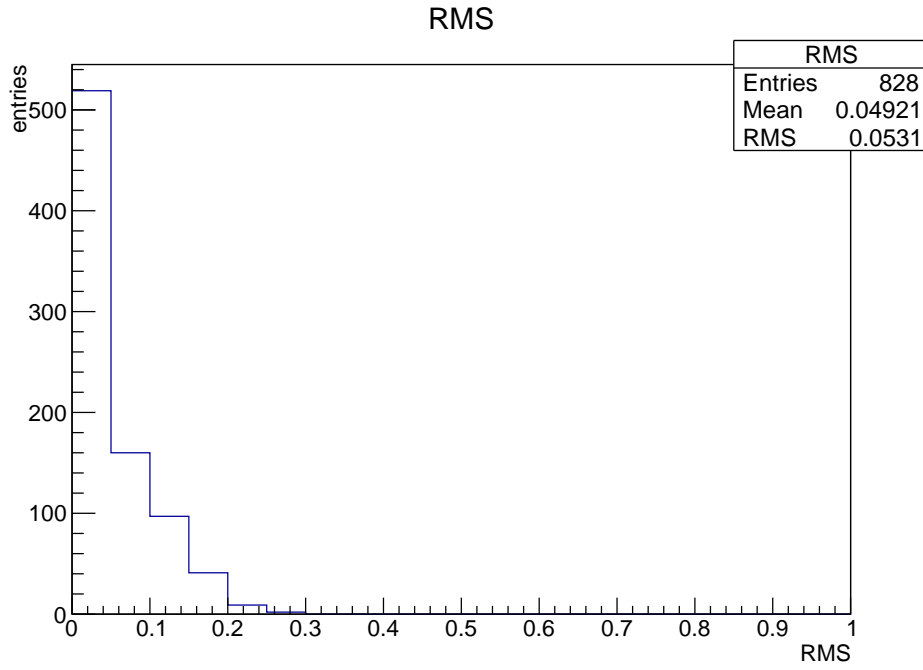


Figure 6.8: Relative spread of gain for gain values obtained with the second method

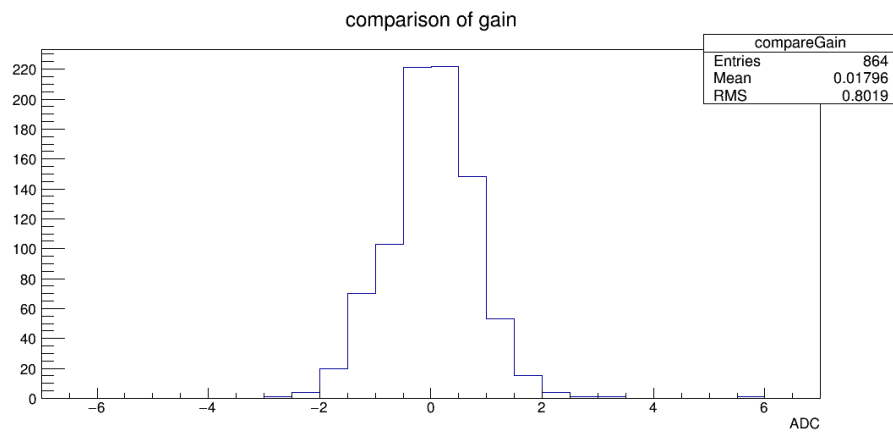


Figure 6.9: Comparison of gain values from DESY with own values

6 Analysis of test beam data

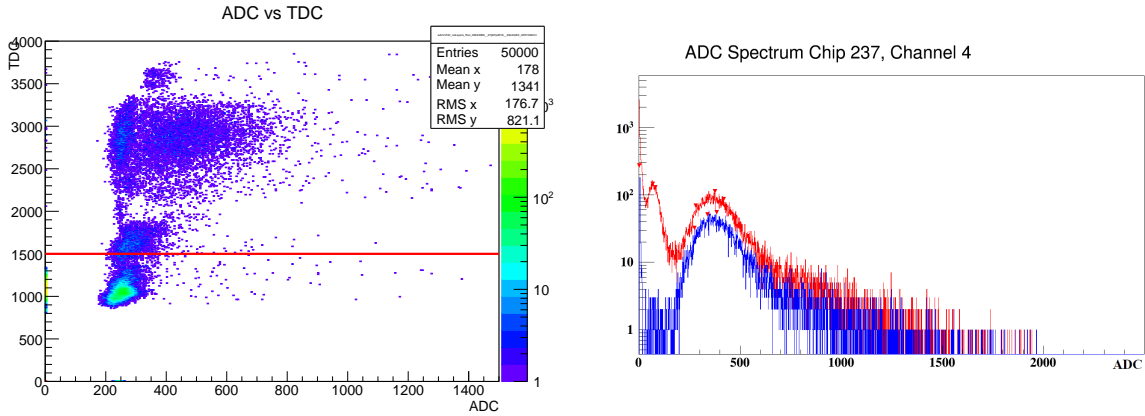


Figure 6.10: Left: Plot of TDC vs ADC distribution to determine the position of the cut; Right: Comparison of MIP plot without (red) and with (blue) TDC cut

6.2 Determination of MIP energy

6.2.1 TDC cut

As described in section 5.2, a cut on the TDC value needs to be performed to remove the noise peak. The left side of figure 6.10 shows how the position of the TDC cut is chosen. The ADC and TDC values are plotted against each other and the cut is placed at the gap in the distribution at 1500 TDC. The right side of figure 6.10 depicts how the cut affects the shape of the MIP peak. The structure at the left side of the MIP peak is cut off from the distribution of the ADC values before the cut (in red), but the position of the MIP peak remains the same.

6.2.2 MIP values

The MIP distribution is fitted with a Landau-Gaussian fit as described in section 5.2. The sigma for the Gaussian fit was checked. It is always nearly 50 for the first 1 to 6 layers, between 70 and 90 for the last 8 layers with the older boards and near 100 for layer 7. Figure 6.11 shows some examples for the resulting MIP values and, after division by the gain values, the light yields and the corresponding distributions.

In some few cases, the data for certain channels is missing (most likely due to wrong channel values in the eLog). Here, the values obtained at DESY are used. This was necessary for 15 out of 1008 channels.

The gain and MIP values obtained above are then loaded into the database and can be used for further analysis.

6 Analysis of test beam data

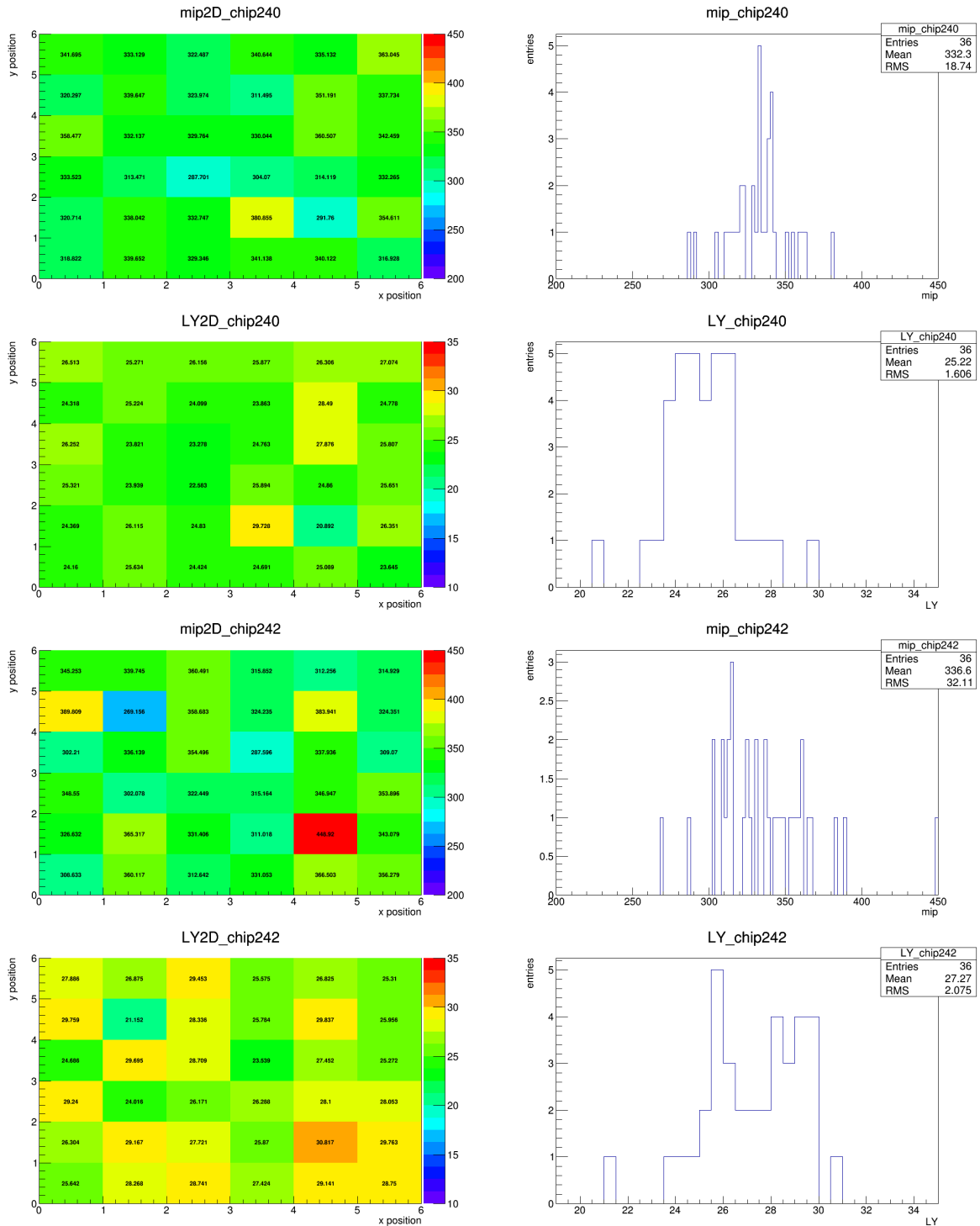


Figure 6.11: Chipwise MIPs and light yields and corresponding distributions for chip 240 and 242

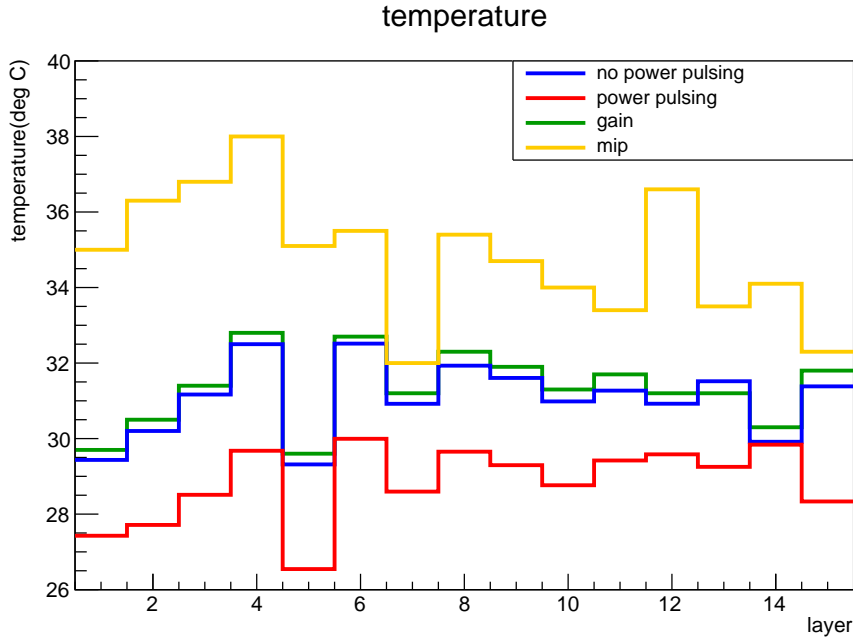


Figure 6.12: Comparison of the average temperature per layer for a beam energy of 5 GeV; the temperatures of the LED runs and the runs without power pulsing are similar, the temperatures for the runs with power pulsing are approximately 3°C colder, the MIP runs are warmer by several degrees most of the time

6.3 Temperature difference

Figure 6.12 shows a comparison of the temperatures of electron data with and without power pulsing, LED runs and MIP runs. The simulation and the LED runs have approximately the same temperature, while the power pulsing runs are colder by approximately 3°C. This is expected, since the electronics are switched off in power pulsing mode when not needed, thus it should not produce as much heat. This shift in temperature is visible in all layers but layer 12 and 14 where the temperature difference is much smaller. The MIP runs are distinctly warmer than the other runs except for layers 7 and 15, where the temperature is close to the gain runs and the runs without power pulsing, and their temperatures fluctuate more.

6.4 Analysis of electron data

6.4.1 Beam profiles

To start with, different beam profiles are examined. At first, the centre of gravity is compared for runs with and without power pulsing. The distributions for the x-

6 Analysis of test beam data

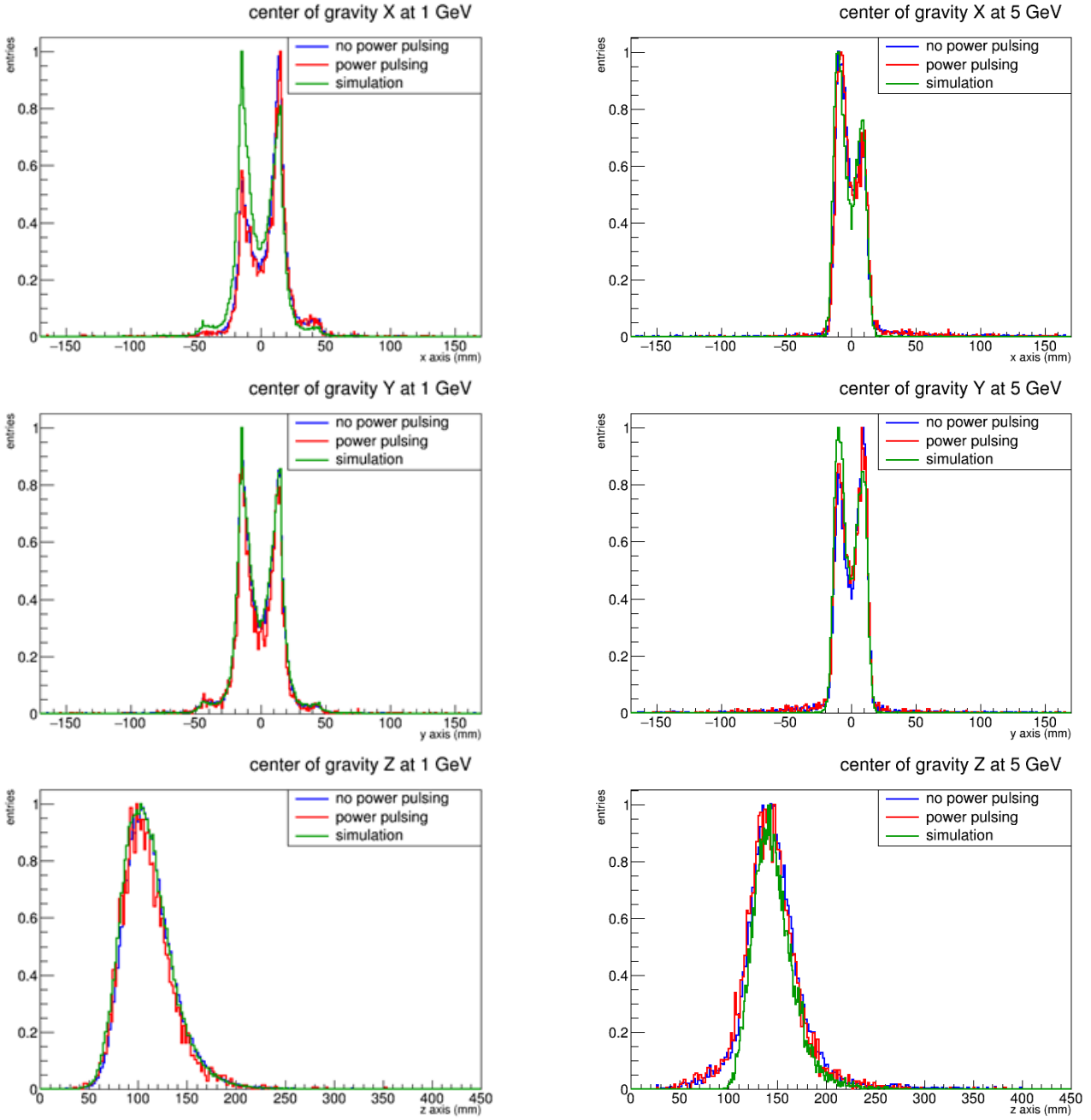


Figure 6.13: Comparison of centre of gravity for 1 and 5 GeV: distributions for x- and y-direction are used to optimise the simulation; from the well-aligned z-distributions, it can be concluded that the description of the detector material is correct

6 Analysis of test beam data

and y-directions are used to optimise the position of the beam centre and the width of the beam in the simulation. The centre of gravity is the weighted average of all hit positions with their energy with the assumption that the position of the hit is in the centre of the tile. Examples for the centres of gravity at 1 and 5 GeV are given in figure 6.13. The plots are scaled so that the maximum value is at 1. The distributions for the x- and y-direction show a double peak structure. The positions of the peaks are in the centres of the four (two in x- and two in y-direction) innermost cells of the HBU. The two peaks occur because the beam mainly hits those cells. The shapes of the centre of gravity distributions in x and y are very similar for no power pulsing and power pulsing and are used to adjust the beam width and the distance between the particle source and the detector in the simulation so that it also looks similar. This calibration aligns the positions and number of peaks of all three distributions, but the beam path of the simulation is slightly tilted in regard to the z-direction of the detector in regard to the runs with and without power pulsing, that is why one side of the distribution is higher than the other. Due to that, the simulation is not completely alike to the real data for the x-direction at 1 GeV and the y-direction at 5 GeV. The z-direction is not affected by the alignment of the simulation. Thus, it can be used to check if the description of the detector material is correct. Those distributions are nearly identical, which leads to the conclusion, that there are no problems in the description of the detector. It can also be observed that the maximum is shifted towards the end of the detector for 5 GeV in the distributions for the z-direction. This is expected because the electron shower grows longer at higher energies.

6.4.2 Longitudinal shower profile

Now, the longitudinal shower profile is examined. It is calculated in three different ways: with the energy per hit, the number of hits per event, and the total energy per event. Distributions for those values are produced layerwise and the mean of the histogram, respectively the mean of a Gaussian fit for the number of hits per event, is calculated (see fig. 6.14). With these values, a longitudinal shower profile can be created (see fig. 6.15), the errors are negligible. All the distributions have a similar shape and their maxima are in similar layers. As expected, the maxima of the distributions move towards later layers for higher beam energies. It can be observed that the distribution for power pulsing looks different from the others starting at layer 8, especially for runs at 5 GeV. In these layers, there is more energy with less entries at the same time. The distributions over all layers for the energy per hit, the number of hits per event, and the total energy per event are depicted in figure 6.16. For the distributions, the statistical errors are negligible. The energy per hit distribution shows an approximately exponential shape with a lot of entries at low energies and fewer entries at higher energies and is very similar for data with and without power pulsing and simulation. The first bin is empty because in the reconstruction a cut is applied on the hit energy at 0.5 MIP energies. The distributions for power pulsing and

6 Analysis of test beam data

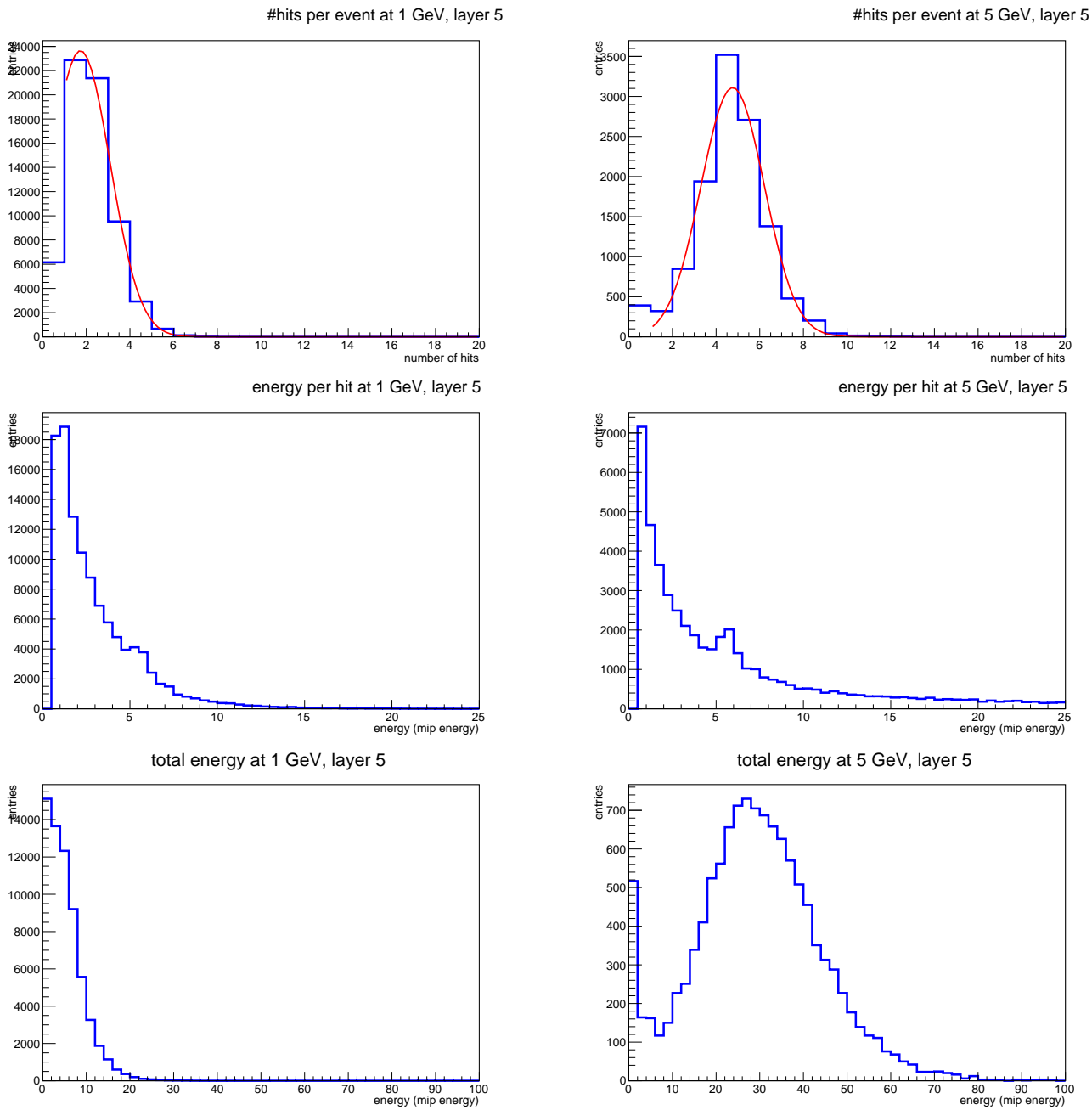


Figure 6.14: Distribution for the number of hits in layer 5 per event with Gaussian fit to calculate the mean (top), the energy per hit in layer 5 (middle) and the total energy per event in layer 5 (bottom) at energies of 1 and 5 GeV For a run without power pulsing. Their means are used to calculate a longitudinal shower profile.

6 Analysis of test beam data

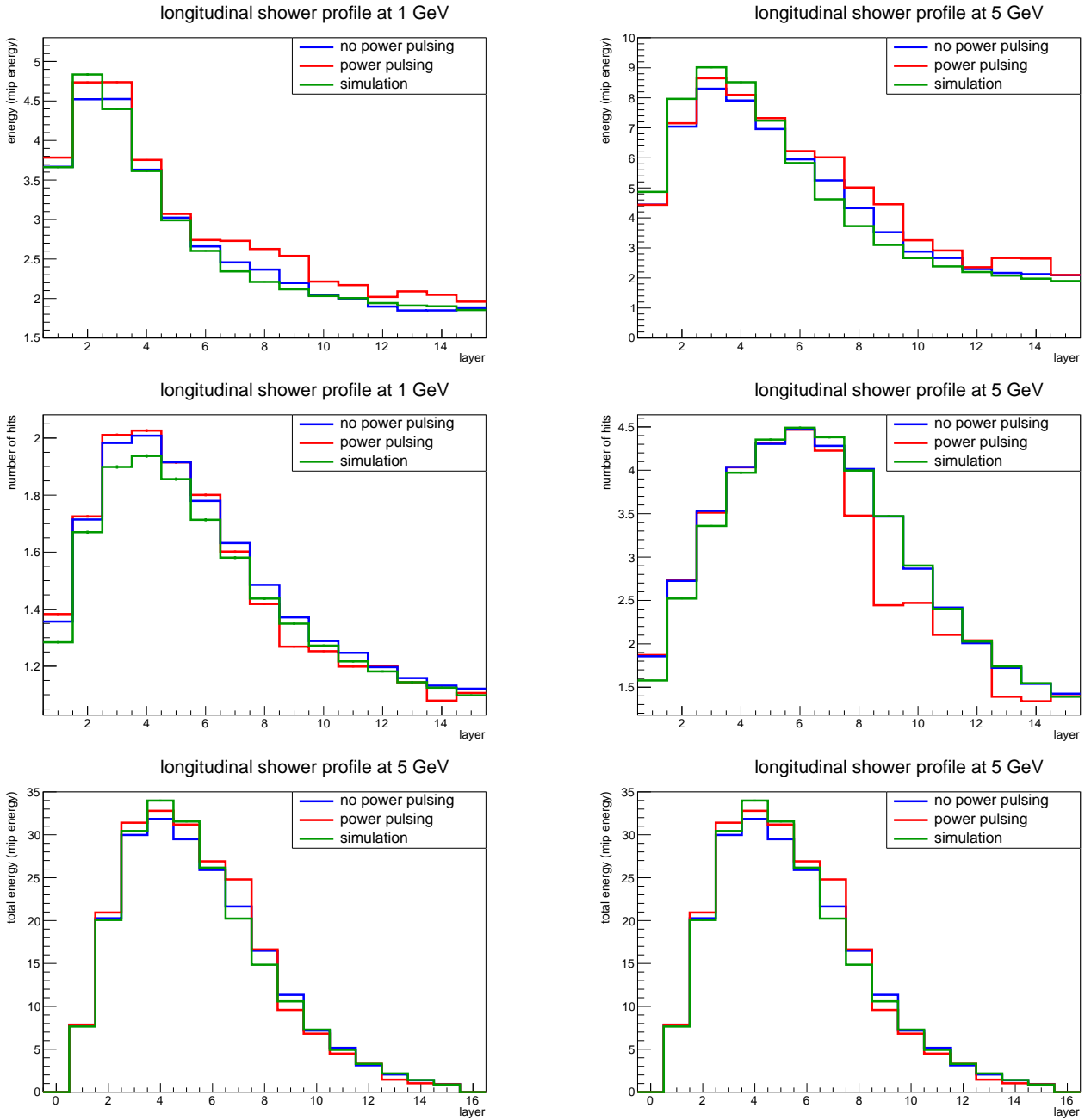


Figure 6.15: Longitudinal shower profile for the energy (top), the number of hits per event (middle) and the total energy per event (bottom) for 1 and 5 GeV derived from the layerwise distributions for the energy per hit, the number of hits per event or the energy per event

6 Analysis of test beam data

no power pulsing have a small dent around 6 MIP energies compared to the simulation. This is most probably due to incorrect high gain - low gain intercalibration correction values. This correction needs to be executed, because the data are taken in autogain mode. The ASIC has two different lines for amplifying the signal: the high gain has a bigger amplification factor and the low gain a smaller one. In autogain mode, the ASIC decides by the height of the signal if a strong or a small amplification, and thus high gain or low gain, is needed. But high gain and low gain both shift the signal by a different amount and this needs to be corrected for with the high gain - low gain intercalibration factors. Updated values were provided, but the time was not sufficient to utilise them in this thesis. For the number of hits per event, the distribution at 1 GeV is similar for all three types of data, but for 5 GeV, the distributions for power pulsing and no power pulsing are shifted with respect to each other with the simulation in between them. The total energy per event is similar for 1 GeV, and also for power pulsing and no power pulsing at 5 GeV, but the distribution for simulation has its maximum in lower energies and also is much higher. From these plots, it can be concluded that the simulation fits the data sufficiently well, except for the total energy at 5 GeV. Since the main aim of this analysis is to test the behaviour of the detector, the agreement with the simulation is considered satisfactory, and in the following, data with and without power pulsing will be compared in more detail.

6 Analysis of test beam data

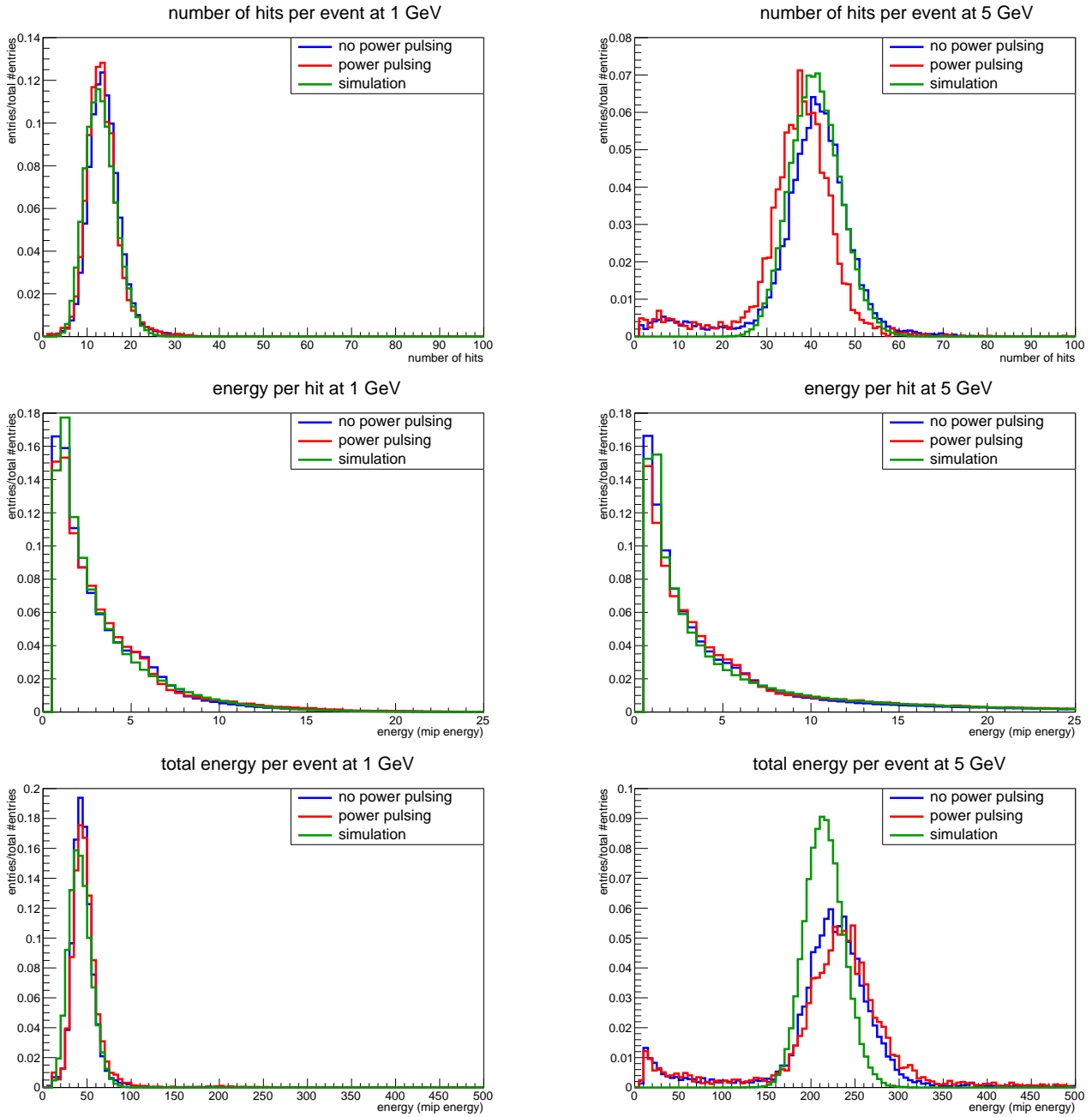


Figure 6.16: Distribution for the number of hits per event (top), the energy per hit (middle), and the total energy per hit (bottom) at 1 and 5 GeV. Except for the simulation for the total energy per hit at 5 GeV, which is higher than the two other distributions, all distributions are very similar to each other.

6.5 Detailed comparison of the data with and without power pulsing

Taking a closer look at the distributions for the energy per hit and the number of hits per event, now the means are taken into account. Therefore, for the energy per hit distribution, the mean of the histogram is taken and for the number of hits distribution, a Gaussian fit is performed, the calculated values are listed in table 6.1). Comparing those values, the number of hits per event and the energy per hit increase with higher beam energy as expected, but it seems like the runs with power pulsing have less hits but at the same time a higher energy per hit.

To check if the behaviour in layer 8 and following is responsible for the shifts

		mean #hits	mean energy
1 GeV	no PP	13.7	3.18
1 GeV	PP	13.2	3.34
5 GeV	no PP	41.6	5.15
5 GeV	PP	38.2	5.64

Table 6.1: Mean of the distributions for the energy per hit and the number of hits per event

in the distributions between the runs with and without power pulsing, the layerwise distributions for the number of hits (see fig. 6.17), the energy per hit (see fig. 6.18), and the total energy (see fig. 6.19) are summed up incrementally to see at which point the distributions start to diverge. All distributions look similar for the first few layers but starting from layer 8 to 9, they begin to diverge. Therefore, the single layers are examined now in more detail. First, the 2D distribution of the hits and total energy per channel are calculated. An example for layer 8 at 5 GeV is depicted in figure 6.20. More layers can be found in the appendix (8.2). It can be observed that the shower mostly hits the four central tiles, the other channels mainly show noise. The central tiles are numbered from one (top left) to four (lower right). The distribution from the run without power pulsing looks uniform over the four central tiles as expected, but looking at cell 3 from the power pulsing distribution, it is the one with the highest energy but also with the lowest number of hits. Also, the whole ASIC seems to have a lower statistics since approximately one third of the cells is empty which are significantly more than in the other ASICs. The same behaviour can also be observed for cell 3 in layer 9, 10, and 11 and cell 1 in layer 9.

To understand why these cells behave differently, the energy distribution is plotted for each of the central cells. Examples for layer 8 are given in figure 6.21, more examples are in the appendix (8.1). Here, it is visible that cell 1, 2, and 4 look similar. They have their maximum at low energies and fewer entries at higher energies. Also, they have a second peak at around 6 MIP energies. This is due to the faulty high gain - low gain intercalibration values as explained above. In cell 3, however, the distribution looks different. Here, the first four to six bins contain nearly no entries. With that, it

6 Analysis of test beam data

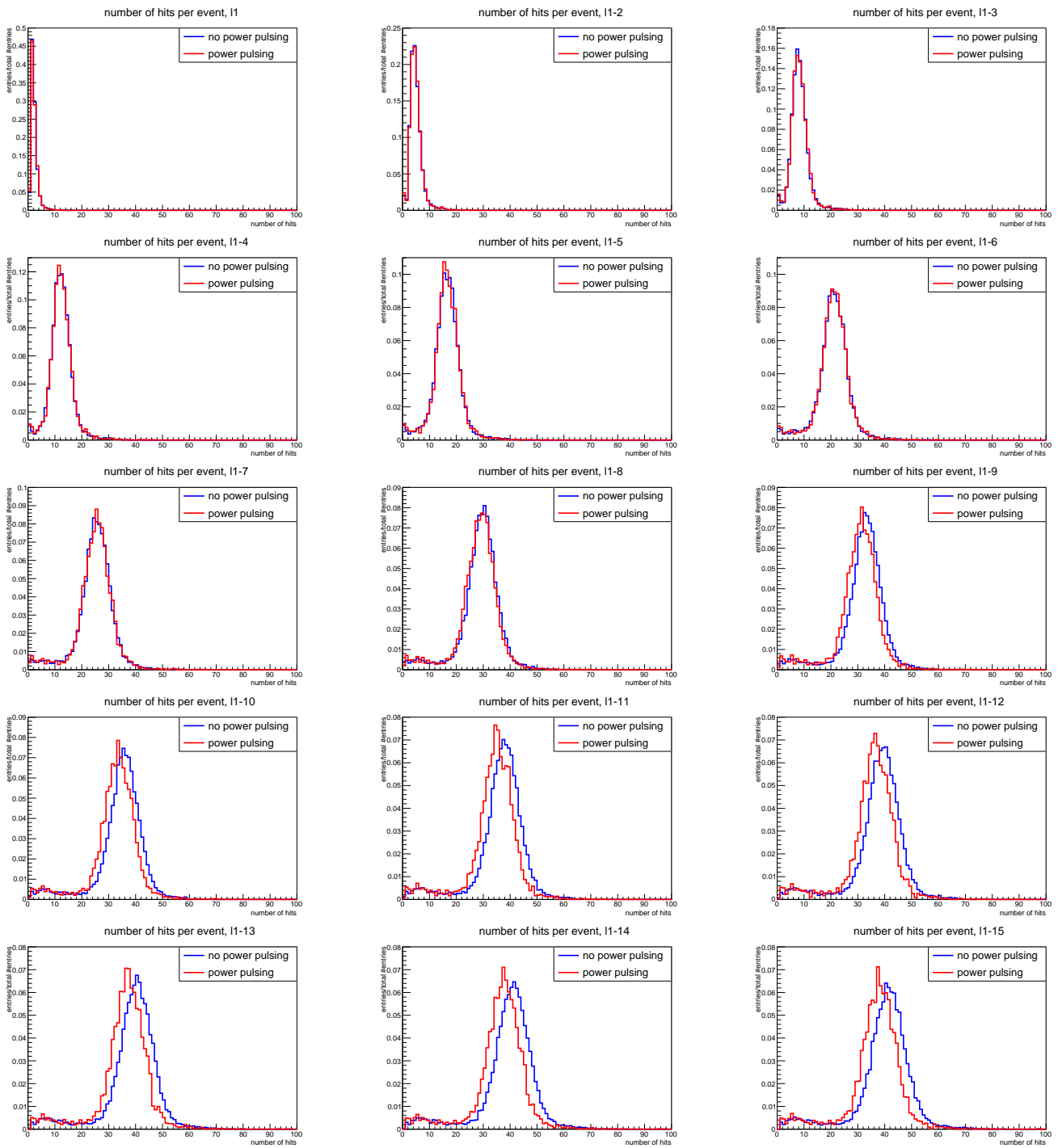


Figure 6.17: Distribution for incremental layerwise sum over the number of hits per event

6 Analysis of test beam data

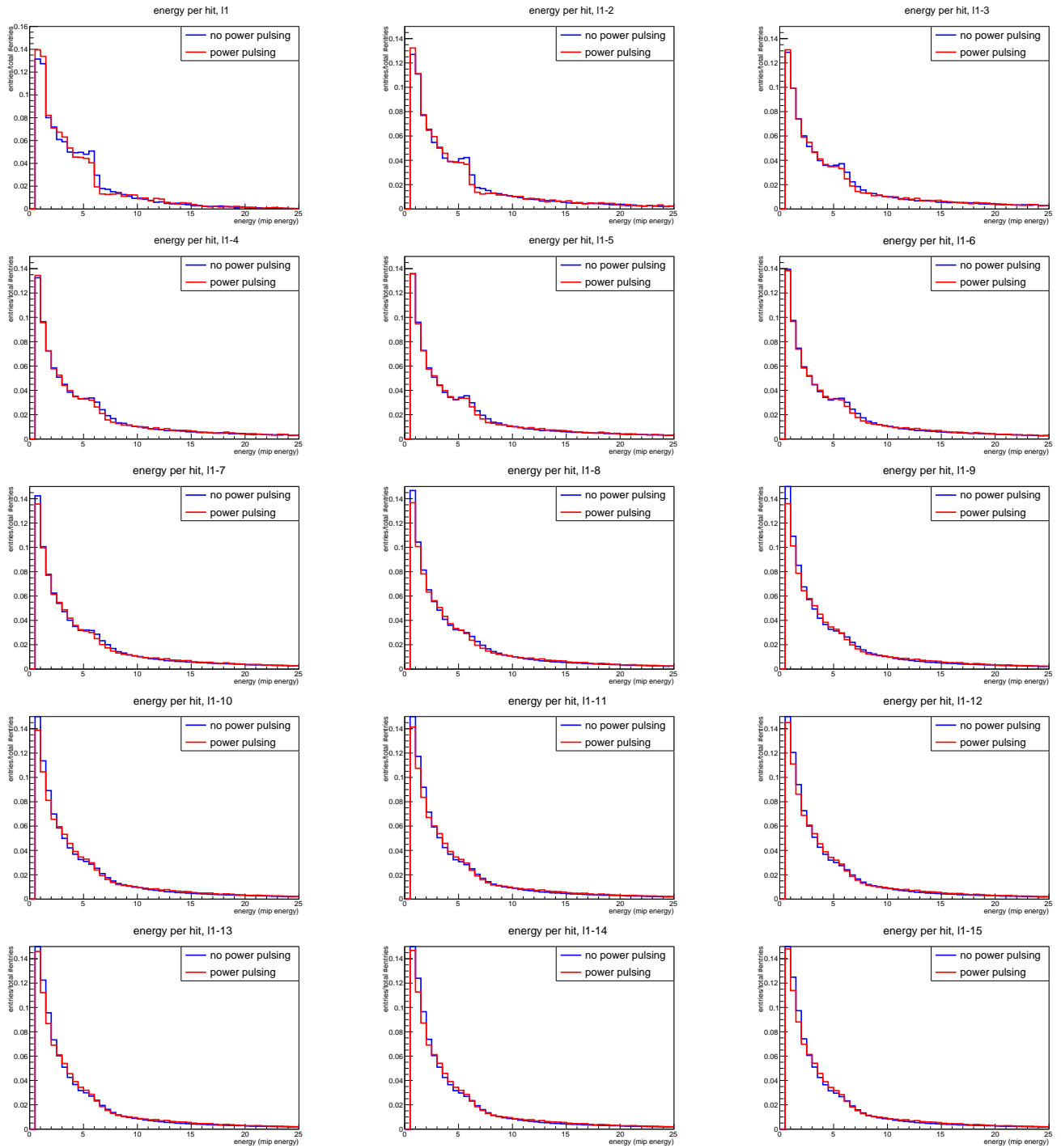


Figure 6.18: Distribution for incremental layerwise sum over the energy per hit

6 Analysis of test beam data

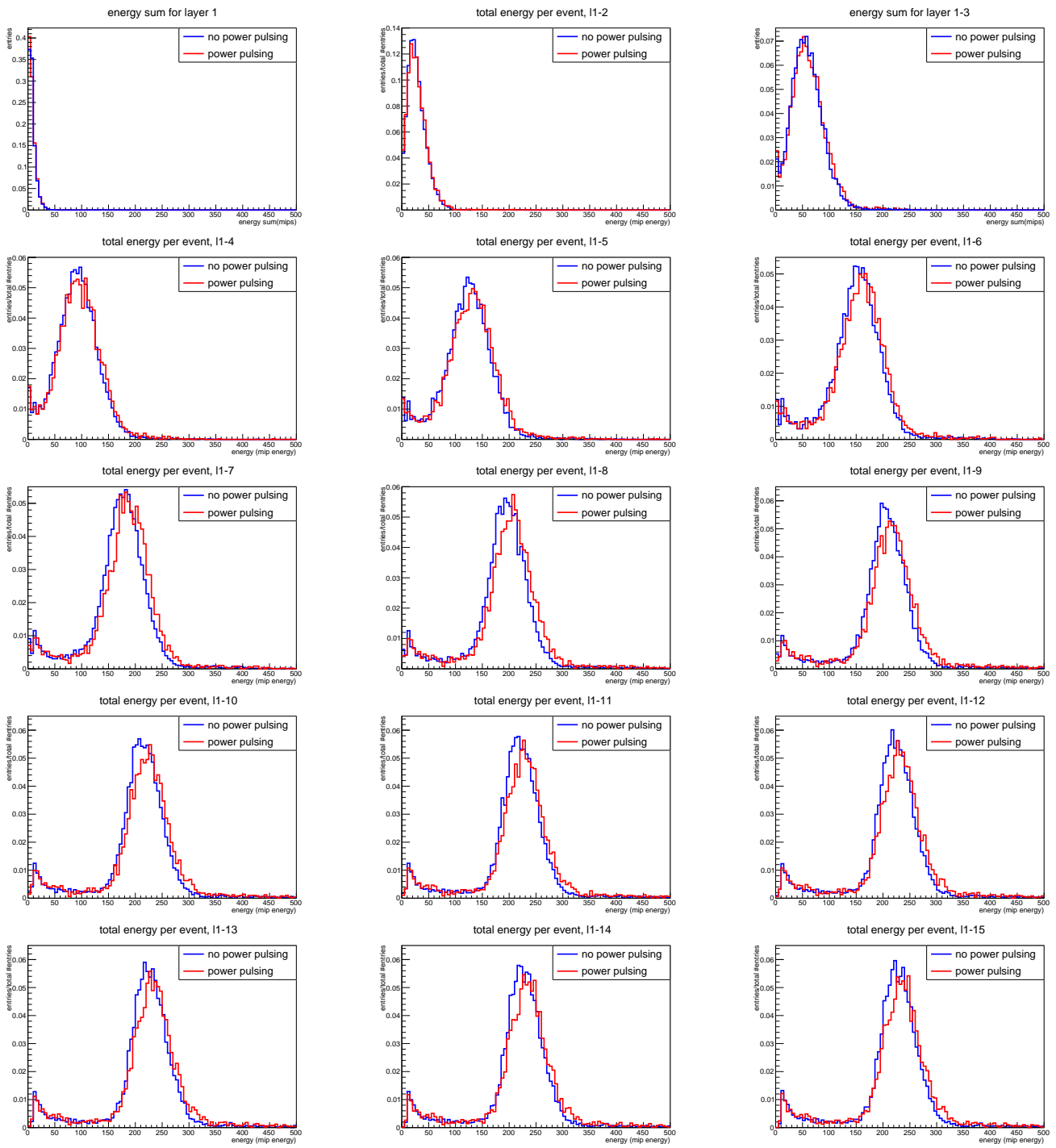


Figure 6.19: Distributions for incremental layerwise sum over the total energy

6 Analysis of test beam data

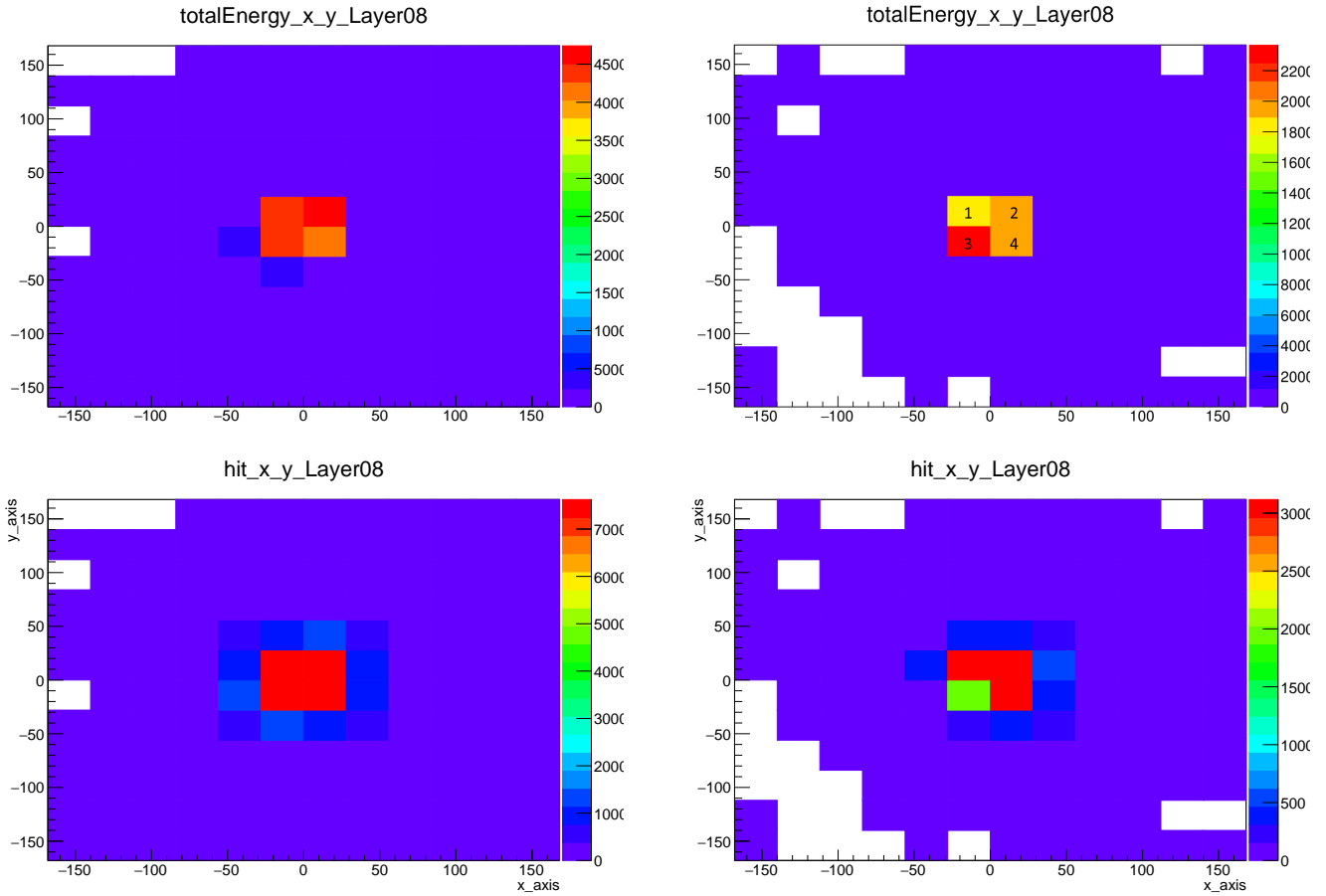


Figure 6.20: 2D distribution for layer 8 at 5 GeV for no power pulsing (right) and power pulsing (left) with the total energy (top) and the number of hits per channel

can be explained, why the other distributions showed less entries at a higher energies in the affected layers. There are less entries, because the first bins that are usually the highest are cut off. The energy in the other distributions seems to be higher because the mean of the energy distribution is used. If, like here, the entries at low energies are missing, the mean will move to higher energies. There is no final explanation for this error yet, one reason could be that the TDC got stuck, further hardware tests will be performed at DESY. Hopefully, the problem is specific to the older HBU versions since it does not seem to affect the first layers where newer HBU versions have been used.

6 Analysis of test beam data

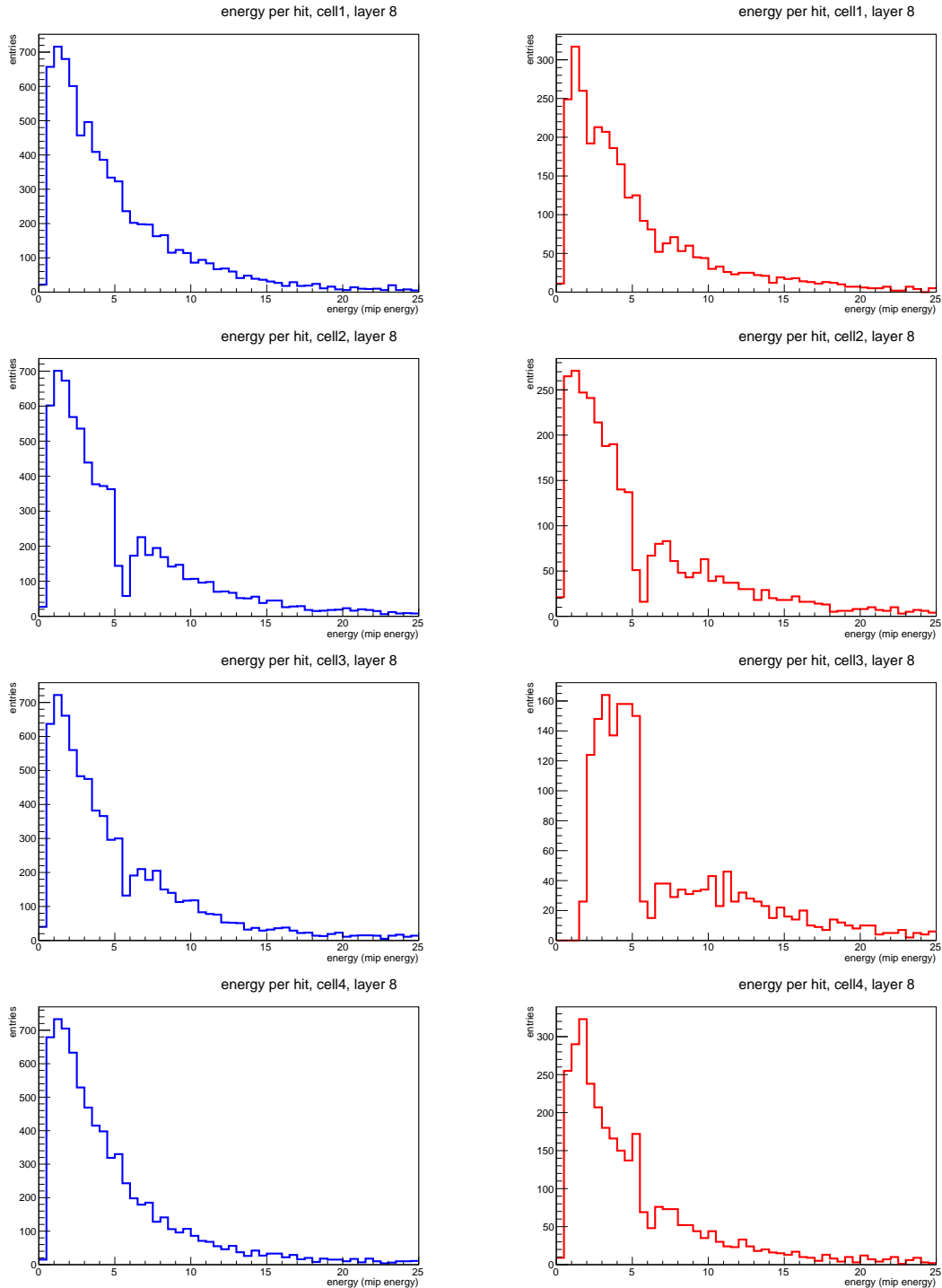


Figure 6.21: Comparison of cellwise energy distribution for layer 8 at 5 GeV for runs without (left) and with (right) power pulsing

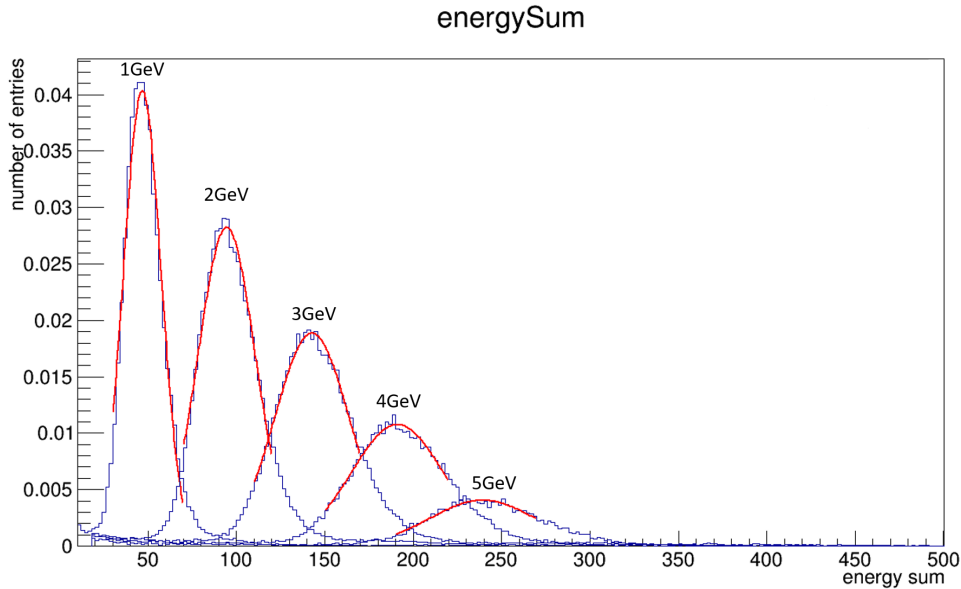


Figure 6.22: Energy sum at different energies with Gaussian fits

6.5.1 Linearity of energy measurement

An important variable is the total energy, also called energy sum. If the showers are fully contained, the mean of the energy sum should be linear with respect to the beam energy. The energy sum is the sum over the hit energies per event. Those values are plotted in a histogram and then fitted with a Gaussian fit to calculate the mean. The energy sums with fits for beam energies from 1 GeV to 5 GeV are depicted in figure 6.22. The distributions are scaled with the number of entries. For runs with power pulsing, two energies are missing, because for the runs at 3 GeV, layers 7 to 15 were turned off and the runs at 4 GeV are defective and cannot be reconstructed. As expected, the position of the maximum shifts towards higher MIP energies with rising beam energies. Then, the means are plotted against the beam energies and fitted with a linear function. The fits for the runs with and without power pulsing after the temperature correction are shown in figure 6.23. The statistical error is negligible, but it can be assumed that the highest systematic uncertainties result from the temperature differences in the layers and the averaging process for determining the gain. In order to estimate the error, the largest temperature difference in one layer is calculated, which is 2.7°C. This equals an error of 1.8%. For the error of the gain averaging, the RMS for each histogram that calculates the gain (see fig. 5.3) divided by the gain of this channel is filled into a histogram and its mean is used as error. This leads to an error of 4.9%. Through quadratic addition, the total systematic error can be calculated as 5.2%. The different run types themselves show a linear response, and are compatible within the error range.

6 Analysis of test beam data

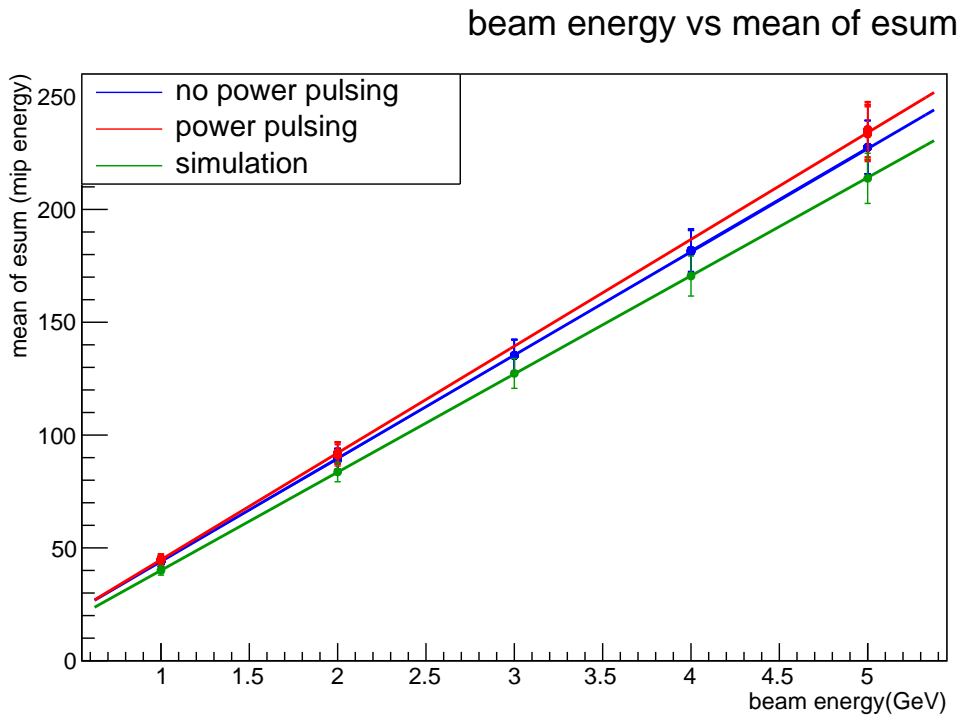


Figure 6.23: Beam energies plotted against the mean of the energy sums

7 Conclusion and Outlook

In this thesis, data taken with an engineering prototype of the AHCAL in an electron beam at energies of 1 to 5 GeV were analysed. To summarise the results, first, the gain and MIP calibrations were performed successfully and the calculated values were used for the reconstruction. Then, the temperature correction factors are determined and applied to the energy values. For the electron data analysis, the data for runs with and without power pulsing were compared with simulation. The beam profiles for the centre of gravity are very similar. The longitudinal shower profile was created with three different variables (number of hits, energy per hit, total energy per hit) of which all the distributions looked similar, apart from the last layers for the power pulsing data. This was examined in more detail and a problem was found that concerns four channels, and presumably also the corresponding ASICs, in the layers 8 to 11. In those channels, the hits at low energies are missing which leads to a higher mean energy in those channels which also affects the longitudinal shower profiles. Finally, the linearity of the energy sums were compared. The runs with and without power pulsing and the simulation all showed a linear behaviour and agreed within the range of the errors, even though there were faulty channels in the power pulsing runs. As conclusion, it can be said that the behaviour of the detector with and without power pulsing and the simulation agree very well, especially for the newer first seven layers. Starting in the older boards in layer 8, some channels behave differently than expected, but the goal to show that, the newer boards in particular, give reasonable results when run in power pulsing mode could be reached.

To complete the analysis, the proper high gain - low gain intercalibration values need to be used to erase the double peak structure in the energy, but the effect of this correction should be minor.

And the strangely behaving channels in the layers 8 to 11 need to be checked. Therefore, the TDC value will be examined to see if it got stuck. If this is not the case, the problems most probably result from a hardware problem for which further data need to be collected.

Bibliography

- [1] The ILD Concept Group.
International large detector: Letter of intent.
<https://arxiv.org/abs/1006.3396v1>, 2010.
- [2] <http://www.linearcollider.org/from-design-to-reality>.
(24.09.2017).
- [3] https://en.wikipedia.org/wiki/File:Standard_Model_of_Elementary_Particles.svg.
(22.10.2017).
- [4] <https://www.uni-muenster.de/Physik.AP/Demokritov/Forschen/Forschungsschwerpunkte/mBECwabaf.html>.
(25.09.2017).
- [5] David Griffith.
Introduction to Elementary Particles.
Wiley-VHC, 2008.
p. 37-40.
- [6] B.R. Martin and G. Shaw.
Particle Physics.
Wiley-VHC, 2008.
p. 1-2, 24, 27-28, 85f, 179-180, 239f, 265, 285.
- [7] <https://home.cern/topics/higgs-boson>.
(25.09.2017).
- [8] Christoph Scholz Bogdan Povh, Klaus Rith and Frank Zetsche.
Teilchen und Kerne.
Springer, 2006.
p. 293ff.
- [9] Bruce A. Schumm.
Deep down things : the breathtaking beauty of particle physics.
The Johns Hopkins University Press, 2004.
p. 7ff.
- [10] <http://www.nuclear-power.net/nuclear-power/reactor-physics/interaction-radiation-matter/interaction-gamma-radiation-matter/#prettyPhoto/2/>.
(24.09.2017).

Bibliography

- [11] William R. Leo.
Techniques for Nuclear and Particle Physics Experiments: A How-to Approach.
Springer, 1994.
p. 21f, 27, 33, 35f, 54ff.
- [12] <http://www.nuclear-power.net/wp-content/uploads/2015/03/Bremsstrahlung-vs.-Ionization.png?a34b7f>.
(24.09.2017).
- [13] Francis Halzen and Alan D. Martin.
Quarks and Leptons: An Introductory Course in Modern Particle Physics.
John Wiley and Sons, 1984.
p. 19f, 129f.
- [14] http://meroli.web.cern.ch/meroli/lecture_stragglingsfunction.html.
(24.09.2017).
- [15] Wolfgang Demtröder.
Experimentalphysik 4: Kern-, Teilchen- und Astrophysik.
Springer, 2005.
p. 83.
- [16] Christian W. Fabjan and Fabiola Gianotti.
Calorimetry for particle physics.
<http://adsabs.harvard.edu/abs/2003RvMP...75.1243F>, October 2003.
- [17] Claus Grupen and Boris A. Shwartz.
Particle Detectors.
Cambridge University Press, 2008.
p. 9, 41, 83, 186ff, 230ff, 249f.
- [18] Nicholas P. Guillemaud.
Radiation fluence to dose conversion factors for sensors studied in slac experiment t-506.
<https://www.slideshare.net/NikolasGuillemaud/guillemaud-thesis>,
2015.
- [19] Karl-Johan Grahn for the ATLAS Liquid Argon Calorimeter Group.
A layer correlation technique for pion energy calibration at the 2004 atlas combined beam test.
<https://arxiv.org/abs/0911.2639>, 2009.
- [20] Claude Leroy and Pier-Giorgio Rancoia.
Physics of cascading shower generation and propagation in matter: principles of high-energy, ultrahigh-energy and compensating calorimetry.
<http://iopscience.iop.org/article/10.1088/0034-4885/63/4/202/meta>,
2000.
- [21] <http://www.physicsmasterclasses.org/exercises/keyhole/sp/detectors/DELPHI.html>.
(24.09.2017).

Bibliography

- [22] Oskar Hartbrich.
Commissioning and LED system tests of the engineering prototype of the analog hadronic calorimeter of the CALICE collaboration.
<http://www-library.desy.de/cgi-bin/showprep.pl?thesis12-040>, 2012.
- [23] The CALICE Collaboration.
Tests of a Particle Flow Algorithm with CALICE Test Beam Data.
<https://arxiv.org/abs/1105.3417v3>, 2011.
- [24] Lars Weuste.
Mass measurement of right-handed scalar quarks and time measurement of hadronic showers for the compact linear collider.
<http://nbn-resolving.de/urn:nbn:de:bvb:19-157943>, 2013.
- [25] Ties Behnke, James E. Brau, Brian Foster, Juan Fuster, Mike Harrison, James McEwan Paterson, Michael Peskin, Marcel Stanitzki, Nicholas Walker, and Hitoshi Yamamoto.
International large detector: Technical design report: Volume 1: Executive summary.
<https://arxiv.org/abs/1306.6327>, 2013.
- [26] Philip Burrows, Brian Foster, Nicholas Walker, John Carwardine, Keisuke Fujii, Kirk Yamamoto, Marcel Demarteau, Michael Harrison, Pan Qian, Perrine Royole-Degieux, Rika Takahashi, and Barbara Warmbein.
The International Linear Collider - From Design to Reality.
<http://www.linearcollider.org/from-design-to-reality/>.
- [27] R.P. Walker.
Radiation Damping.
<https://cds.cern.ch/record/398430/files/p461.pdf>.
- [28] Ties Behnke, James E. Brau, Philip N. Burrows, Juan Fuster, Michael Peskin, Marcel Stanitzki, Yasuhiro Sugimoto, Sakue Yamada, and Hitoshi Yamamoto.
International large detector: Technical design report: Volume 4: Detectors.
<https://arxiv.org/abs/1306.6329>, 2013.
- [29] Mark Terwort for the CALICE Collaboration.
Status of the CALICE analog calorimeter technological prototypes.
<https://arxiv.org/abs/1209.2594>, 2012.
- [30] Andy White.
The Detailed Baseline Design for the SiD Detector Concept.
http://www.fnal.gov/directorate/ILCPAC/2012Dec/SiD_DBD_ILC_PAC_Dec_2012-Stanitzki.pdf, 2012.
- [31] Phi Chau.
Automatische Bestückung und Test von CALICE-Ausleseboards, 2017.
- [32] C. D'Ambrosio.
A short Overview on Scintillators, 2005.

Bibliography

- [33] Sensl.
Introduction to SiPM - Technical Note, 2005.
- [34] http://www.hamamatsu.com/eu/en/support/glossary/o/index.html?_ga=2.54601387.186950117.1510786980-1802652550.1510316782&_gac=1.250792370.1510316782.EAIaIQobChMIq6W0s4C01wIV0hXTCh1mWwmnEAAYASAAEgKvnPD_BwE.
(16.11.2017).
- [35] Nils Feege.
Silicon Photomultipliers: Properties and Application in a Highly Granular Calorimeter .
http://www.iaea.org/inis/collection/NCLCollectionStore/_Public/40/018/40018286.pdf, 2008.
- [36] <http://particle-physics.desy.de/e252106/e252106/e252334>.
(12.11.2017).
- [37] <http://particle-physics.desy.de/e252106/e252106/e252211>.
(12.11.2017).
- [38] <http://www.hamamatsu.com/jp/en/S13360-1325PE.html>.
(23.11.2017).
- [39] <http://www.hamamatsu.com/jp/en/S12571-015P.html>.
(23.11.2017).
- [40] <http://www.sensl.com/downloads/ds/DS-MicroBseries.pdf>.
(23.11.2017).
- [41] <https://root.cern.ch/>.
(11.11.2017).
- [42] http://ilcsoft.desy.de/MarlinReco/v00-02/manual_html/manual.html.
(12.11.2017).
- [43] <http://ilcsoft.desy.de/v01-17-09/DD4hep/v00-15/doc/html/index.html>.
(12.11.2017).
- [44] Email conervation with Yuji Sudo, 25.08.2017.

8 Appendix

8.1 Cellwise energy distribution

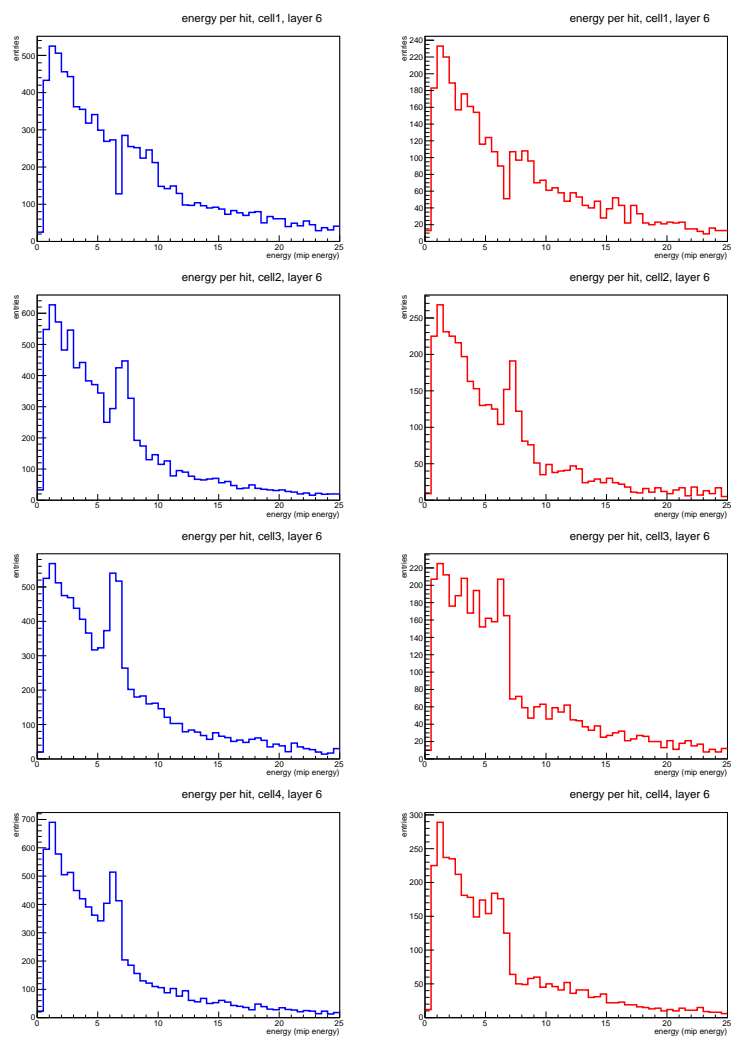


Figure 8.1: Comparison of cellwise energy distribution for layer 6 at 5 GeV for runs without (left) and with (right) power pulsing

8 Appendix

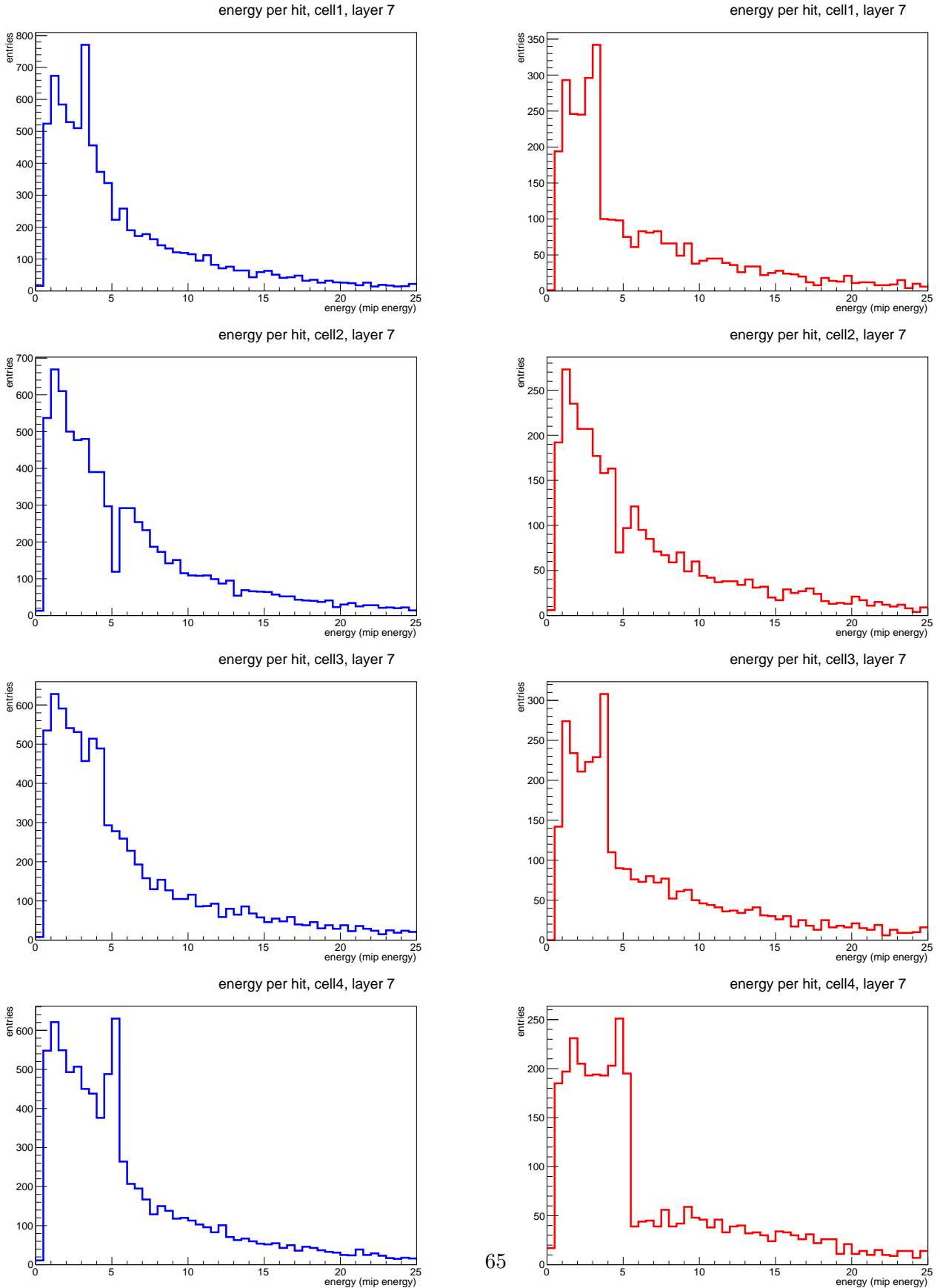


Figure 8.2: Comparison of cellwise energy distribution for layer 7 at 5 GeV for runs without (left) and with (right) power pulsing

8 Appendix

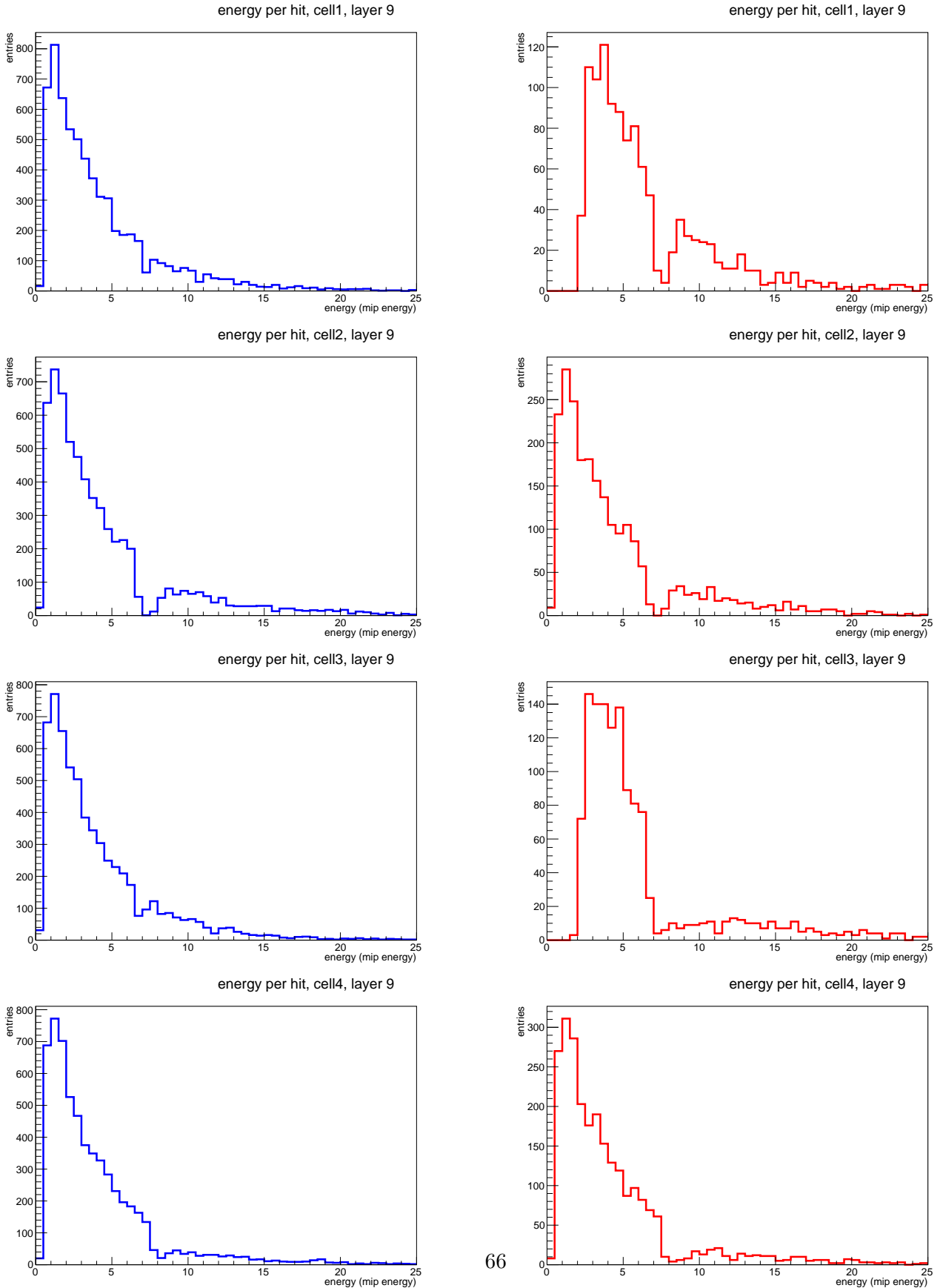


Figure 8.3: Comparison of cellwise energy distribution for layer 9 at 5 GeV for runs without (left) and with (right) power pulsing

8 Appendix

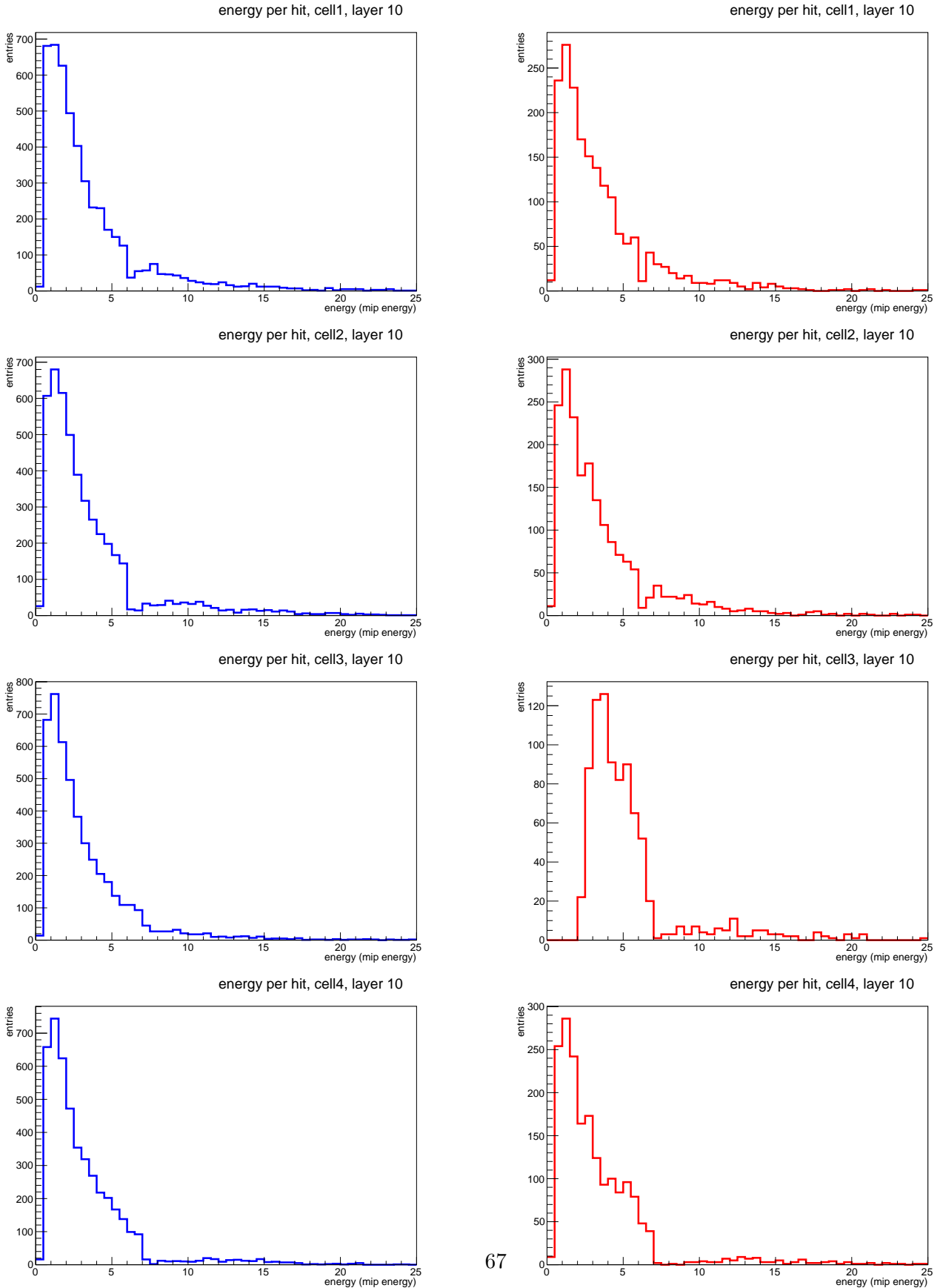


Figure 8.4: Comparison of cellwise energy distribution for layer 10 at 5 GeV for runs without (left) and with (right) power pulsing

8 Appendix

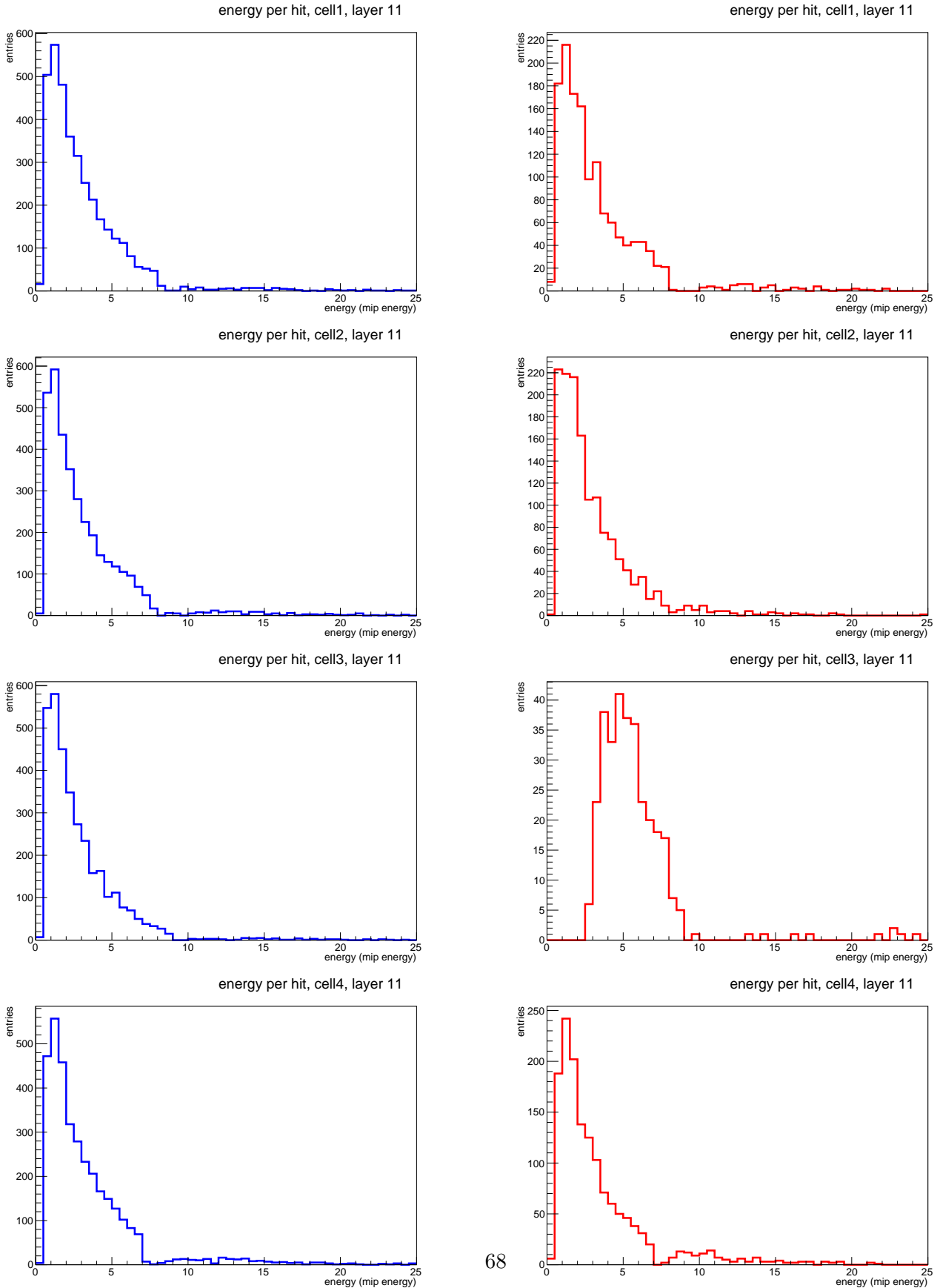


Figure 8.5: Comparison of cellwise energy distribution for layer 11 at 5 GeV for runs without (left) and with (right) power pulsing

8 Appendix

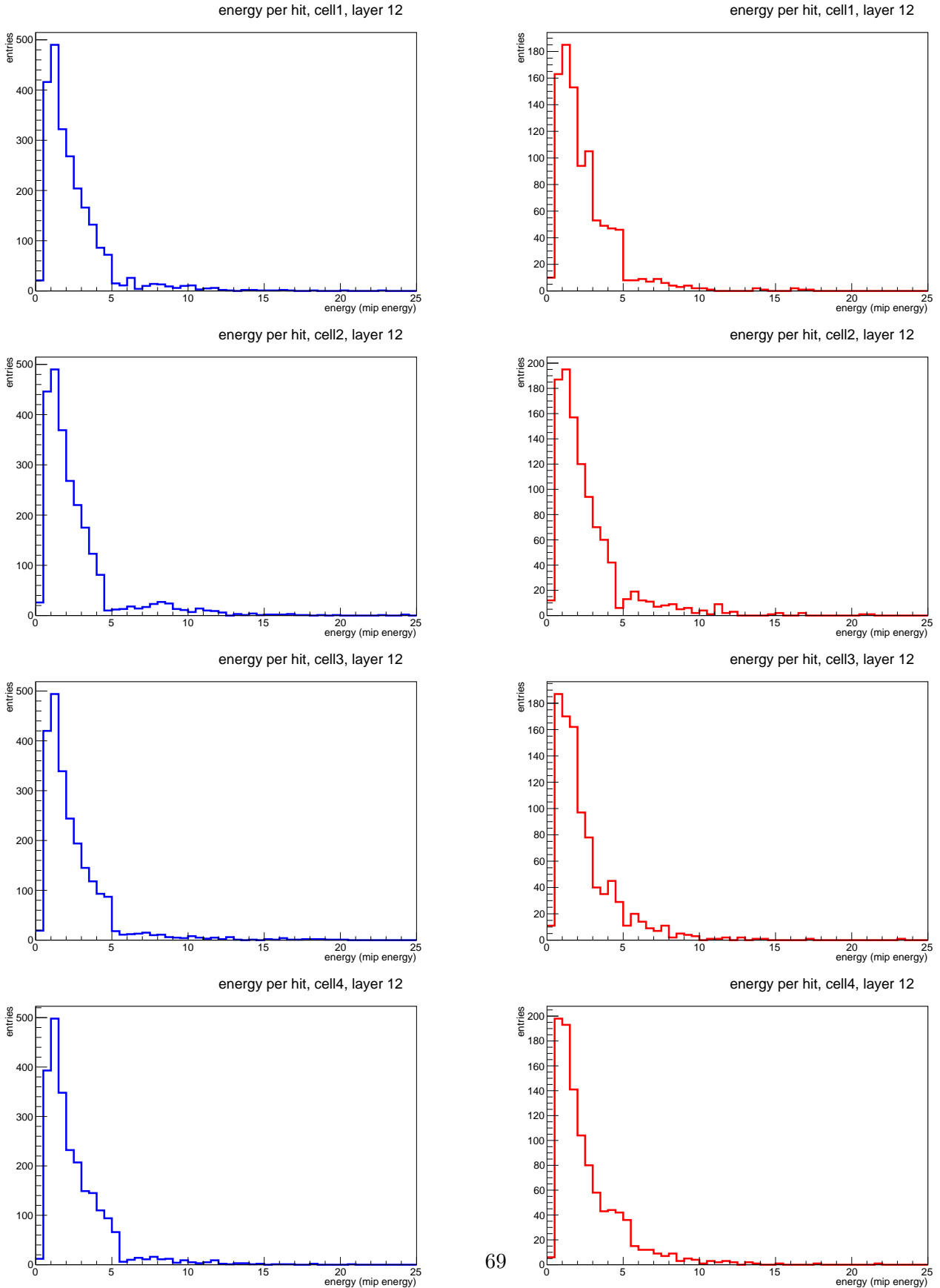


Figure 8.6: Comparison of cellwise energy distribution for layer 12 at 5 GeV for runs without (left) and with (right) power pulsing

8 Appendix

8.2 2D distributions for each layer

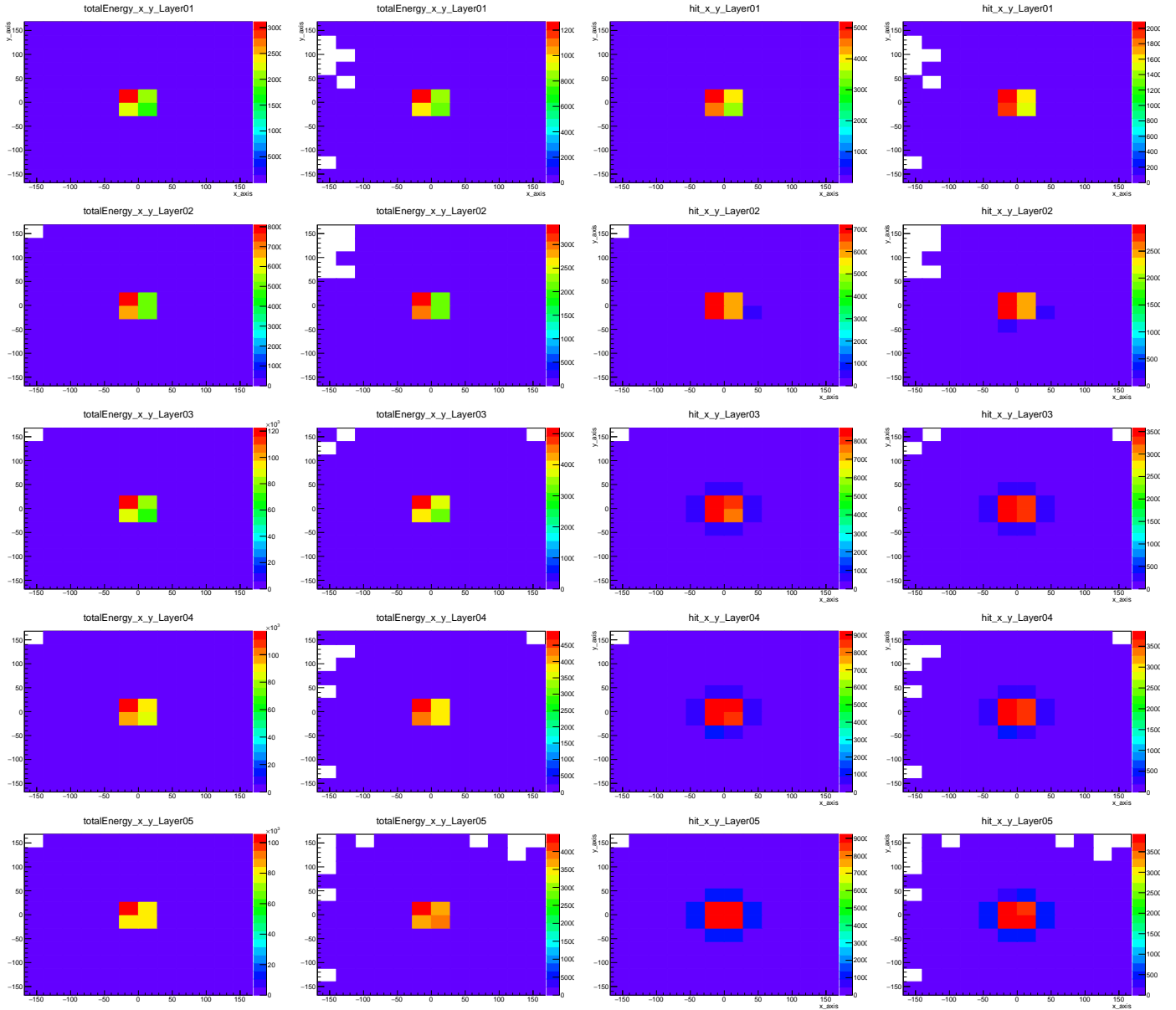


Figure 8.7: 2D distributions for no power pulsing (left) and power pulsing (right), layer 1 to 5

8 Appendix

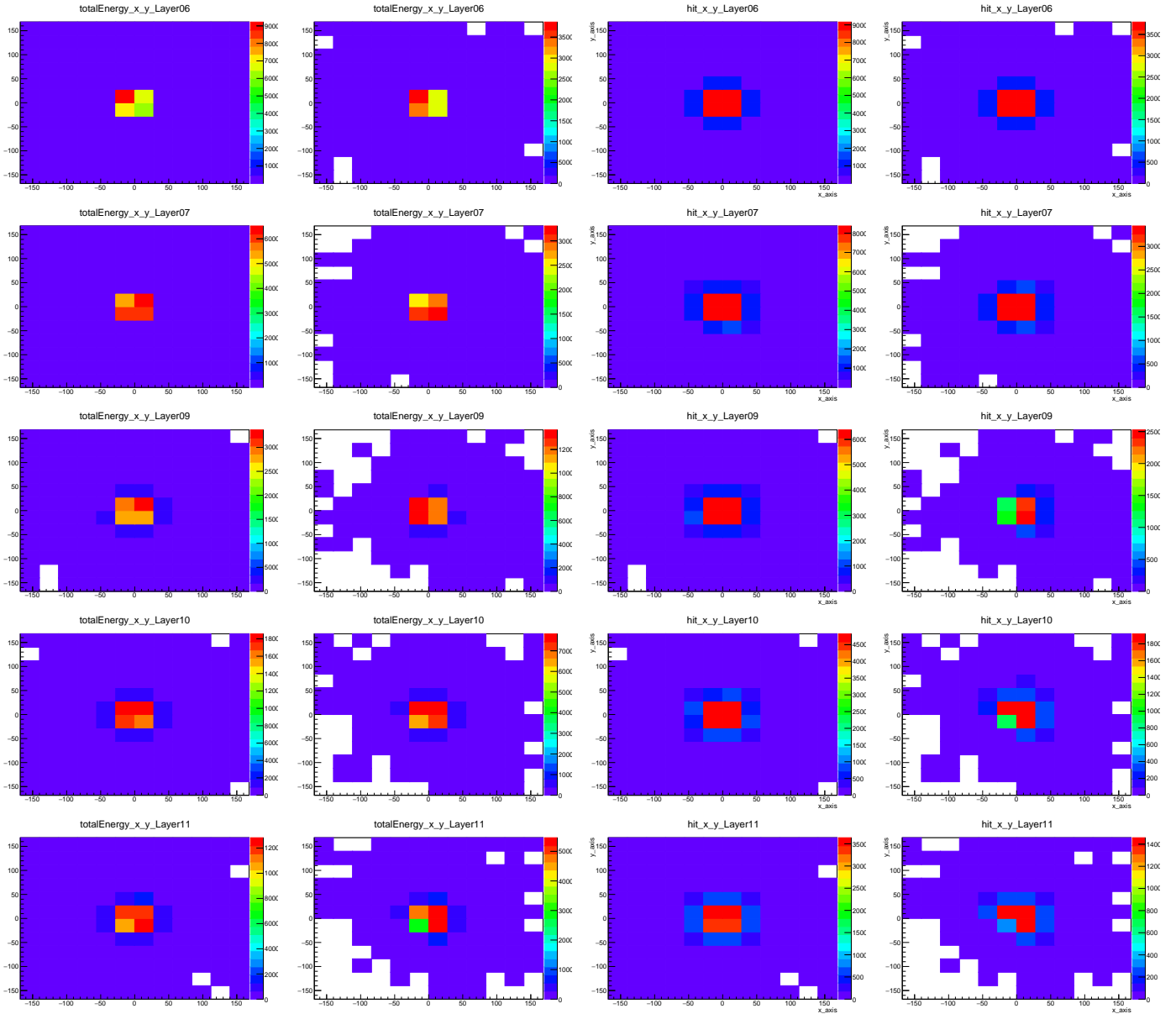


Figure 8.8: 2D distributions for no power pulsing (left) and power pulsing (right), layer 6, 7, and 9 to 11

8 Appendix

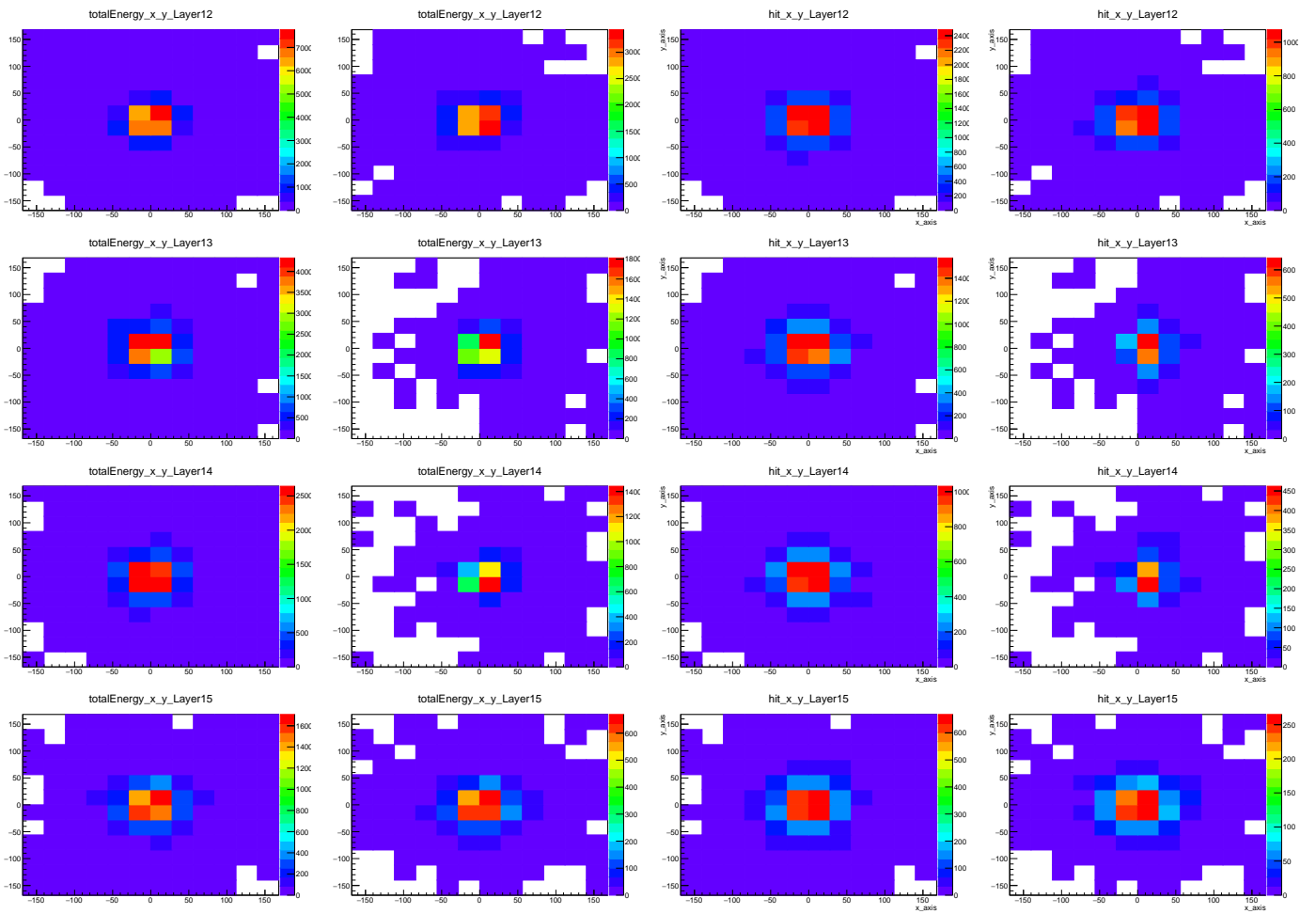


Figure 8.9: 2D distributions for no power pulsing (left) and power pulsing (right), layer 12 to 15

9 Acknowledgements

This thesis would not have been possible without the support of many people over the last years.

First, I would like to express my gratitude to my supervisor Prof. Dr. Lucia Masetti for giving me the opportunity to work on this topic and for all the helpful advices and ideas. In addition, I thank Prof. Dr. Volker Büscher for examining my thesis.

Furthermore, I would like to thank my colleagues in Mainz for always dealing with my questions, their encouragement, and a lot of fun. It is a pleasure working with you.

I am also very grateful for the help the colleagues at DESY provided.

A huge thanks goes to my flatmates for all the nice chats, relaxing evenings on the couch and feeding me chocolate when times get stressful, and in particular to Chrisi, for proofreading the whole thesis, the late night walks and talks, and for not letting me starve when I don't have the time to cook.

Flora, thank you for your cheerful attitude and for always believing in me (and, of course for proofreading).

Furthermore, I would like to thank my friends for all the fun we have and my family and especially my boyfriend Konstantin for always being there for me.